Performance monitoring and adaptative compensation of system impaiments for high-speed coherent optical multicarrier communication

Alexandru Ionut Frunza

DOCTORAT BRETAGNE LOIRE / MATHSTIC

THÈSE DE DOCTORAT DE

L'ÉCOLE NATIONALE
D'INGÉNIEURS DE BREST
DÉLIVRÉE CONJOINTEMENT AVEC
ACADEMIA TEHNICĂ MILITARĂ "FERDINAND I"

ÉCOLE DOCTORALE N° 601
Mathématiques et Sciences et Technologies de l'Information et de la Communication
Spécialité : *Télécommunications*

Par

Alexandru Ionuț FRUNZĂ

Global compensation of system linear impairments for high-speed coherent optical communications

Thèse présentée et soutenue à Brest, le 07/12/2022
Unité de recherche : Lab-STICC, CNRS UMR 6285

Rapporteurs avant soutenance :

Laurent ROS	Professeur, Grenoble INP
Ion MARGHESCU	Professeur, Universitatea Politehnica din București

Composition du Jury :

Président :	Christelle AUPETIT-BERTHELEMOT	Professeur, ENSIL-ENSCI
Rapporteurs :	Laurent ROS	Professeur, Grenoble INP
	Ion MARGHESCU	Professeur, Universitatea Politehnica din București
Examinateurs :	Christelle AUPETIT-BERTHELEMOT	Professeur, ENSIL-ENSCI
	Iulian Cristian RÎNCU	Maître de Conférences, Academia Tehnică Militară "Ferdinand I"
	Angela DIGULESCU-POPESCU	Maître de Conférences, Academia Tehnică Militară "Ferdinand I"
Co-dir. de thèse :	Alexandru ȘERBĂNECU	Professeur, Academia Tehnică Militară "Ferdinand I"
Dir. de thèse :	Stéphane AZOU	Professeur, École Nationale d'Ingénieurs de Brest
Co-encadrant :	Vincent CHOQUEUSE	Maître de Conférences, École Nationale d'Ingénieurs de Brest

Invité(s) :

	Philippe CIBLAT	Professeur, Telecom Paris, Institut Polytechnique de Paris
Co-encadrant :	Pascal MOREL	Maître de Conférences, École Nationale d'Ingénieurs de Brest

ACKNOWLEDGEMENT

Another chapter of my life concluded with the completion of my Ph. D. studies. It was a fantastic experience during which I received a lot of professional and personal support. Therefore, I would like to thank the people who helped me.

First, I would like to thank the *Institut français de Roumanie* for financing this thesis, the *Romanian Ministry of National Defence* for supporting it, and to the institutions which managed it *École Nationale d'Ingénieurs de Brest* (ENIB), and *Academia Tehnică Militară "Ferdinand I"* (ATM).

I'm extremely grateful to my awesome team who supervised me during this work: my co-directors Prof. Stéphane AZOU and Prof. Alexandru ȘERBĂNESCU, and my co-supervisors, Dr. Vincent CHOQUEUSE and Dr. Pascal MOREL. This thesis wouldn't have been possible without your valuable guidance. I learned so many things and improved myself a lot in these three years. Thank you for your continuous help in scientific matters and for your general life advice. I couldn't imagine a better experience, and I hope this is only the beginning of our collaboration.

I also extend my deepest gratitude to the professors who agreed to evaluate my thesis work. Thank you to Prof. Laurent ROS and Prof. Ion MARGHESCU, who reviewed my work and provided me with valuable feedback that allowed us to consider exciting perspectives. Thank you to Prof. Christelle AUPETIT-BERTHELEMOT, jury president, Dr. Iulian RÎNCU, and Dr. Angela DIGULESCU-POPESCU for assessing my work. Your questions were interesting and helpful. I would also like to thank Prof. Philippe CIBLAT for participating in my defense and his interesting questions during the presentation. I would also like to thank dr. Erwin PINCEMIN, Prof. Emanuel RĂDOI, and Prof. Ali MANSOUR for their commentaries and useful advice as members of *Comité de suivi de thèse*.

Many thanks to Prof. Constantin VIZITIU, Prof. Cristian MOLDOVEANU, Dr. Florin ENACHE, Dr. Florin POPESCU, and Dr. Petrică CIOTÎRNAE for ensuring good conditions for this thesis development. Special thanks to Dr. Alexandru GRIVEI, who perfectly managed stressful situations allowing me to focus on my research. Thanks should also go to Dr. Laura TELESCU and Dr. Mihai TELESCU for helping me in Brest

and for the very nice discussions we had. I gratefully acknowledge the assistance of Adina PLUȚU, Amelia MALACU, and Daniela DIN, who helped me in general in ATM.

I would like to thank all the people from ATM and ENIB for the help, advice and nice talks during these years: Prof. Ammar SHARAIHA, Prof. Ioan NICOLAESCU, Prof. André PERENNOU, Dr. Georgiana ROȘU, Dr. Véronique QUINTARD, Leontin TUȚĂ, Dr. Abdesslam BENZINOU, Dr. Kamal NASREDDINE, Dr. Thierry RAMPONE, and Céline ANSQUER. I also extend my sincere thanks to all the teachers and instructors that prepared me during my studies. Without your dedication, I wouldn't have come such a long way.

For the duration of the thesis, I had the opportunity to discover places and bond new friendships. I would like to thank for their support, pleasant discussion, and nice moments spent together: Dr. Jacqueline SIME, who also helped a lot in my scientific work, Dr. Abdelouahid BEN TAMOU, Dr. Noor HAMDASH, Dr. Marwa BRAIKI, Dr. Dimitrios KASTRITSIS, Cristina DESPINA-STOIAN, Dr. Mohamad YOUNES, Dr. Yuliya DADOENKOVA, Denis STĂNESCU, Romildo DE SOUZA, Dr. Bárbara Pilar DUMAS FERIS, Paolo KIOHARA, Dragoș NASTASIU, Raed AL HASSANIEH, Dr. Ramez HAMIE, Dr. Igor GLUKHOV, Abraham SOTOMAYOR FERNANDEZ, Cristina POPOVICI, Dr. Adan Omar ARELLANES BERNABE, Dr. Mahdi KASMI, Anthonin MARTINEL, Filipe LOPES, Dr. Morann MATTINA, Maeva FRANCO, Răzvan SCRIPCARU.

I am very grateful to my fiancee Bianca for all the support I received during this journey. You constantly encouraged me and you were there for me in the difficult times, thank you. I'd also like to extend my gratitude to my parents, Ion and Mariana. You have done a great job as parents. This wouldn't have been possible without you. I would like to also thank my sister Georgiana, uncle Cristi, and all my family and my fiancee's family who supported me in my work.

An important piece of support during the thesis I receveived from my friends and I would especially like to thank to: Adina, Cosmin, Bogdan & Adelina, Adrian & Crina, Mihai & Codruța.

Finally, I would like to thank everyone who helped me, which I did not mention here. I really appreciate it.

Table of Contents

List of Figures **v**

List of Tables **ix**

Acronyms **xi**

List of Symbols **xv**

Introduction **1**

1 Fundamentals of coherent optical communications **3**

1.1 Optical communication networks 4

1.2 Coherent optical systems 6

1.2.1 Transmitter 7

1.2.2 Optical channel 12

1.2.3 Receiver 17

1.3 Objective of the thesis 23

2 Linear imperfections impact and state-of-the-art compensation techniques **27**

2.1 Preliminaries 27

2.1.1 Signal Model 28

2.1.2 Compensation 28

2.2 In-phase and Quadrature (IQ) imbalance 29

2.2.1 Signal model 30

2.2.2 Compensation 32

2.3 Laser phase noise 34

2.3.1 Signal model 35

2.3.2 Compensation 36

2.4 Chromatic dispersion 39

2.4.1 Signal model 39

2.4.2 Compensation . . . 39
2.5 Polarization mode dispersion . . . 42
2.5.1 Signal model . . . 43
2.5.2 Compensation . . . 44
2.6 Carrier frequency offset . . . 47
2.6.1 Signal model . . . 48
2.6.2 Compensation . . . 48
2.7 Coherent optical transmission under the impact of multiple imperfections . 50
2.7.1 Objective . . . 51
2.7.2 Simulation results . . . 53
2.8 Conclusion and discussion . . . 60

3 Global Digital Signal Processing (DSP)-based compensation of linear imperfections 63
3.1 Global estimation and compensation . . . 64
3.2 Global estimation and compensation in coherent optical systems . . . 65
3.2.1 Signal model . . . 65
3.2.2 Parametric estimation and compensation . . . 68
3.3 Results . . . 77
3.3.1 Simulation results . . . 78
3.3.2 Comparison to the conventional DSP compensation algorithms . . . 84
3.3.3 Experimental demonstration . . . 86
3.4 Conclusion and discussion . . . 89

4 Global compensation of the linear imperfections using a parametric network 91
4.1 A Parametric Multi-Layer Compensation Network . . . 92
4.1.1 Multi-Layer Linear Single-Input Single-Output (SISO) Signal Model 92
4.1.2 Compensation Network Architecture . . . 94
4.1.3 Network training . . . 96
4.1.4 Comparison with conventional Neural Networks . . . 99
4.2 A Parametric Network for Dual Polarization (DP) Coherent Optical System with Multiple Impairments . . . 101
4.2.1 System Architecture . . . 101
4.2.2 Compensation Network . . . 102

4.2.3 Network Layers 102
4.2.4 Network architecture and training 105
4.3 Results 107
4.3.1 Simulation results 107
4.3.2 Comparison to the conventional Deep Learning (DL) and DSP compensation techniques 114
4.3.3 Experimental demonstration 117
4.4 Conclusion and discussion 120

Conclusion and perspectives **121**

A The compensation strategy in conventional coherent optical communications **125**

B Cramér Rao Lower Bound (CRLB) computation for the nonlinear parameters **127**

List of publications **131**

Bibliography **133**

List of Figures

1.1 Global traffic demand forecast [Cis21] . . . 3
1.2 Optical networks architectures, CO: Central Office . . . 5
1.3 Generic architecture of a coherent optical chain. . . . 6
1.4 Block diagram of a coherent optical transceiver, IQM: IQ Modulator, PBS: Polarization Beam Splitter, PBC: Polarization Beam Combiner. . . . 7
1.5 The frequency response of Root Raised Cosine (RRC) filters with different roll-off factors α_{rf} . . . 9
1.6 The Lorentzian spectral shape of a laser corrupted by the phase noise, δf: Laser Linewidth . . . 10
1.7 Mach-Zehnder Modulator architecture. $E_{in}(t)$ and $E_{out}(t)$ are the electric fields associated with the optical wave at the input and output of the modulator, and $V_i(t)$ is the driving signal corresponding to $i-th$ arm . . . 11
1.8 IQ Modulator architecture and the generation of a 16-QAM signal using two 4-PAM signals . . . 13
1.9 The optical chain composed of multiple spans of fibers and amplifiers . . . 13
1.10 Single-Mode Fiber (SMF) attenuation with wavelength and transmission bands [Opt17] . . . 14
1.11 Energy level diagram of Erbium ions . . . 16
1.12 The configuration of a generic DP coherent optical receiver, LO: Local Oscillator . . . 18
1.13 The detailed diagram of a setup consisting of a 90° hybrid and a balanced photodetector used in Single Polarization (SP) coherent optical systems . . . 19
1.14 Error Vector Magnitude (EVM) representation . . . 22

2.1 IQ imbalance impact on an ideal 4-Quadrature Amplitude Modulation (QAM) constellation . . . 31
2.2 Receiver IQ imbalance compensation using Gram-Schmidt Orthogonalization Procedure (GSOP) . . . 33
2.3 Transmitter IQ imbalance compensation using GSOP . . . 33

2.4 Laser Phase Noise (PN) impact on an ideal 4-QAM constellation 35
2.5 Laser phase estimation using pilot symbols and an averaging filter of length L 37
2.6 Laser phase estimation 37
2.7 Laser PN impact and compensation using pilot symbols 38
2.8 Impact of Chromatic Dispersion (CD) on a transmitted pulse 40
2.9 CD impact and compensation using an ideal compensating filter in the frequency domain 40
2.10 Impact of Polarization Mode Dispersion (PMD) on a transmitted signal . . 43
2.11 Multiple-Input Multiple-Output (MIMO) equalizer composed of Finite Impulse Response (FIR) filters 44
2.12 PMD impact and compensation using a MIMO equalizer with Constant-Modulus Algorithm (CMA) 46
2.13 The blocks used for update in the case of CMA and Decision-Directed Least-Mean-Square (DD-LMS) 47
2.14 Carrier Frequency Offset (CFO) impact on a 4-QAM constellation 48
2.15 CFO impact and compensation using a preamble data block 49
2.16 DSP sequence of compensation operations in a coherent optical receiver . . 52
2.17 The frame structure consisting of a preamble and multiple data blocks containing pilots inserted periodically 53
2.18 Communication system impaired by CFO, receiver IQ imbalance, and laser PN 54
2.19 Performance of the first compensation scheme in the presence of IQ imbalance on the receiver side 55
2.20 Communication system impaired by transmitter IQ imbalance, CFO, receiver IQ imbalance, and laser PN 56
2.21 Performance of the first compensation technique in the presence of IQ imbalance on the transmitter and receiver sides 57
2.22 Performance of the second compensation scheme in the presence of IQ imbalance on the transmitter and receiver sides 58
2.23 Performance of the third compensation scheme in the presence of IQ imbalance on the transmitter and receiver sides 59

3.1 SP coherent optical system impaired by laser PN, IQ imbalance, CD, and CFO; LPF: Low-pass filter 66

3.2 Block diagram of the SP coherent optical system under the impact of multiple linear imperfections 66
3.3 The data frame structure, which consists of a preamble and multiple pilot symbols inserted periodically into the data blocks 68
3.4 Laser phase tracking using common phase and polynomial models 71
3.5 A graphical representation of the cost function corresponding to the nonlinear parameters $Dz \in [0, 35000]$ ps/nm and $\Delta F \in [1.5, 2.5]$ GHz 73
3.6 Laser phase estimation for an ideal 16-QAM transmission 77
3.7 Mean Squared Error (MSE) evolution of the Nonlinear Least-Squares (NLS) estimator and CRLB for an Optical Signal-to-Noise Ratio (OSNR) of 20 dB for multiple values of N_0 79
3.8 MSE evolution of the NLS estimator for multiple values of OSNR 80
3.9 Bit Error Rate (BER) evolution for multiple values of OSNR with $\delta f_{tx} = \delta f_{rx} = 100$ kHz, and different values for the number of pilots P 81
3.10 BER evolution for multiple values of OSNR for $N_0 = 100$ with different values of $\delta f_{tx} = \delta f_{rx}$, and $P = 12$ pilot symbols 82
3.11 BER evolution for different $\mathcal{M}$-QAM for multiple values of OSNR 82
3.12 Diagram of the system used for comparison 84
3.13 BER evolution of the competing approaches with respect to OSNR for $\mathcal{M}$-QAM communications ($\mathcal{M} = 4$ and $\mathcal{M} = 16$) 85
3.14 Laser phase estimation using different polynomial orders 87
3.15 QAM coherent optical experimental setup. AWG: Arbitrary Waveform Generator, OMA: Optical Modulation Analyzer 88
3.16 Signal constellations after synchronization and compensation, and the estimated laser phase for the case where $\vartheta = 10°$ 88
3.17 EVM penalty for $g = 1$ dB against phase imbalance (ϑ) with respect to the case where no IQ imbalance occurs 89

4.1 Communication chain with multiple impairments 93
4.2 Proposed multi-layer parametric network depending on the parameter $\boldsymbol{\beta} = \{\boldsymbol{\beta}_1, \cdots, \boldsymbol{\beta}_L\}$) 95
4.3 Data frame structure consisting of a preamble and multiple pilot symbols inserted periodically 97
4.4 Evolution of MSE with the number of iterations during the pilot-based and self-labeling training and testing 99

4.5 Comparison between an Multi-layer Perceptron (MLP) network and the proposed multi-layer parametric network 100
4.6 DP coherent optical system under the impact of laser PN, IQ imbalance, CD, PMD, and CFO 101
4.7 Block diagram of the multi-layer system of interest 102
4.8 The architecture of the parametric compensation network 105
4.9 MSE evolution with respect to the number of iterations during the supervised pilot-based tracking for different values of K 110
4.10 EVM performance of the proposed parametric network 111
4.11 BER performance of the proposed parametric network 111
4.12 Network performance for different values of IQ imbalance (TX & RX) for 16-QAM at an OSNR of 20 dB 112
4.13 Block diagram of the system of interest 114
4.14 BER evolution with respect to OSNR for a static channel 115
4.15 BER evolution with respect to OSNR for a time-variant channel 116
4.16 Block diagram of the system of interest 116
4.17 BER evolution with respect to OSNR 117
4.18 Block diagram of the experimental system of interest 118
4.19 Block diagram of the compensation network 118
4.20 EVM for different values of K during the self-labeling training 119
4.21 Received signal constellations after different processing steps 119

List of Tables

2.1 Parameters classification with respect to the time evolution and polarization impact . . . 28
2.2 The impact of the receiver IQ imbalance for different QAM orders as a function of 1 dB OSNR penalty at a BER of 10^{-2} without any compensation [Far+17] . . . 31
2.3 Summary of the IQ imbalance compensation techniques . . . 34
2.4 Summary of the laser PN compensation techniques . . . 38
2.5 Summary of CD compensation techniques . . . 42
2.6 Summary of PMD compensation techniques . . . 47
2.7 Summary of the CFO compensation techniques . . . 50
2.8 System and imperfections parameters . . . 54

3.1 Different allocation strategies and their corresponding extraction matrices . 69
3.2 System parameters . . . 78
3.3 Imperfections parameters . . . 79
3.4 Approximative number of operations needed for the preamble-based estimation algorithm . . . 83
3.5 Approximative number of operations needed for the phase tracking and compensation algorithm . . . 84
3.6 System and imperfections parameters . . . 85
3.7 The approximate number of operations for the global approach for the preamble-based estimation, phase tracking, and compensation . . . 86
3.8 The approximate number of operations for the local approach in the case "DSP v3" scenario . . . 86

4.1 The compensation transfer matrix of $l-th$ layer depending on the impairments effect in MIMO systems . . . 97
4.2 System parameters . . . 107
4.3 Network and optimizer parameters . . . 108

4.4 Number of FLOPs required by the parametric network 113
4.5 Complexity versus performance regarding the BER and the number of training iterations 113

Acronyms

3GPP	Third Generation Partnership Project
5G	Fifth-generation technology standard for broadband cellular networks
ADC	Analog-to-Digital Converter
ASE	Amplified Spontaneous Emission
ASIC	Application-Specific Integrated Circuit
AWG	Arbitrary Waveform Generator
AWGN	Additive White Gaussian Noise
BASS	Blind Adaptive Source Separation
BER	Bit Error Rate
BPSK	Binary Phase Shift Keying
CD	Chromatic Dispersion
CFO	Carrier Frequency Offset
CMA	Constant-Modulus Algorithm
CRLB	Cramér Rao Lower Bound
CW	Continuous Wave
DAC	Digital-to-Analog Converter
DC	Direct Current
DCF	Dispersion Compensating Fibers
DCM	Dispersion Compensating Module
DD-LMS	Decision-Directed Least-Mean-Square
DFT	Discrete Fourier Transform
DGD	Differential Group Delay
DL	Deep Learning
DP	Dual Polarization
DSP	Digital Signal Processing
EASI	Equivariant Adaptive Separation via Independence

EDFA	Erbium-Doped Fiber Amplifier
EVM	Error Vector Magnitude
FEC	Forward Error Correction
FIR	Finite Impulse Response
FLOP	Floating-point Operation
FSE	Fractionally Spaced Equalizer
GSOP	Gram-Schmidt Orthogonalization Procedure
IIR	Infinite Impulse Response
IM/DD	Intensity Modulation/Direct Detection
IoT	Internet of Things
IQ	In-phase and Quadrature
IQM	IQ Modulator
ISI	Intersymbol Interference
ITU-T	International Telecommunication Union - Telecommunication Standardization Sector
LAN	Local Area Network
LDBP	Learned Digital Back-propagation
LED	Light-Emitting Diode
LM	Levenberg-Marquardt
LMS	Least Mean Square
LO	Local Oscillator
LS	Least-Squares
MAN	Metropolitan Area Network
MCM	Multicarrier Modulation
MIMO	Multiple-Input Multiple-Output
ML	Machine Learning
MLD	Maximum-Likelihood Detector
MLE	Maximum Likelihood Estimator
MLP	Multi-layer Perceptron
MMSE	Minimum Mean Squared Error
MSE	Mean Squared Error
MZM	Mach-Zehnder Modulator

NF	Noise Figure
NLS	Nonlinear Least-Squares
NLSE	Nonlinear Schrödinger Equation
OEO	Optical-Electrical-Optical
OFDM	Orthogonal Frequency Division Multiplexing
OMA	Optical Modulation Analyzer
OOK	On-Off Keying
OSNR	Optical Signal-to-Noise Ratio
PAM	Pulse Amplitude Modulation
PBC	Polarization Beam Combiner
PBS	Polarization Beam Splitter
PDM	Polarization Division Multiplexing
PMD	Polarization Mode Dispersion
PN	Phase Noise
PSD	Power Spectral Density
PSK	Phase Shift Keying
PSP	Principal State of Polarization
QAM	Quadrature Amplitude Modulation
QoS	Quality of Service
ReLU	Rectified Linear Unit
RF	Radio Frequency
RRC	Root Raised Cosine
SCM	Single Carrier Modulation
SDM	Space Division Multiplexing
SE	Spectral Efficiency
SER	Symbol Error Rate
SISO	Single-Input Single-Output
SMF	Single-Mode Fiber
SOA	Semiconductor Optical Amplifier
SP	Single Polarization
TDM	Time Division Multiplexing

WAN	Wide Area Network
WDM	Wavelength Division Multiplexing
ZF	Zero-Forcing

List of Symbols

$x(t)$	continuous-time baseband signal
$x[n]$	transmitted symbol
$\hat{x}[n]$	received compensated symbol
T_{symb}	symbol period
α_{rf}	roll-off factor
$E(t)$	electrical field
P_{source}	laser source power
ω	angular frequency
$\phi(t)$	laser phase
$V(t)$	driving voltage
V_{π}	half-wave voltage
V_{dc}	DC component
V_{pp}	peak-to-peak voltage
$A(z,t)$	wave packet
$\beta(\omega)$	propagation constant
α	attenuation
σ_3	third Pauli matrix
γ	nonlinearity coefficient
$h\nu_s$	photon energy
n_{sp}	spontaneous emission factor
N_{ASE}	PSD of ASE noise
P_s	signal power
B_{ref}	reference bandwidth
σ^2_{ASE}	variance of ASE noise
R	photodiode responsivity
$\Delta\omega$	angular frequency difference
$\mathbf{x}_{in}$	generic input signal
$\mathbf{x}_{out}$	generic output signal

g	gain imbalance
ϑ	phase imbalance
δf	laser linewidth
λ	wavelength
c	speed of light
$\mathcal{F}$	discrete Fourier transform
$\mathcal{F}^{-1}$	inverse discrete Fourier transform
θ	polarization angle
τ	differential group delay
ΔF	carrier frequency offset
$\mathbf{x}$	transmitted signal
$\mathbf{y}$	received signal
$x_{det}[n]$	detected symbol
$b_{tx}[n]$	transmitted bit
$b_{rx}[n]$	detected bit
N_{bits}	total number of bits

INTRODUCTION

High-speed digital communication represents a crucial issue in our modern societies and is a vector of progress in various fields (information, transport, industry, commerce, education, and others). The growing number of services and applications correlated with emerging technologies such as Fifth-generation technology standard for broadband cellular networks (5G) and Internet of Things (IoT) lead to increasing demand for high data rate communications. Single-Mode Fiber (SMF) optics transmission is thought to play a central role in meeting this challenge due to some key features, including bandwidth availability, reliability, and energetic efficiency superior to any other alternative technology. The coherent detection, by recovering amplitude and phase variations of the optical field, is an essential solution that can optimize the performance of long-haul and metro networks. Moreover, there is a growing interest in coherent detection systems for access networks. Combined with Wavelength Division Multiplexing (WDM) and Polarization Division Multiplexing (PDM), this approach permits a very high transmission capacity by using advanced modulation formats and Digital Signal Processing (DSP) algorithms. However, the performance of these systems can be severely degraded by hardware and channel imperfections. Moreover, at this data rate, imperfections can lead to communication interruptions that can significantly impact system performance.

In order to deliver a desirable quality of service, the compensation of imperfections impact should be performed. Generally, the compensation is performed using conventional DSP algorithms handling one or a few imperfections of the optical chain in particular scenarios. Although these techniques proved their effectiveness in compensating for specific imperfections, their performance may be significantly affected in practice due to the mutual influence between various impairments. Furthermore, most algorithms are developed for particular scenarios or/and modulation formats, and their effectiveness may be limited if the setup is changed.

Recently, Machine Learning (ML)/Deep Learning (DL) approaches proved their effectiveness in multiple scientific areas. Consequently, they have also been considered for imperfections compensation in coherent optical systems. However, it is difficult for these approaches to benefit from the model knowledge of the system, and their computational

complexity may be prohibitive for the moment. Moreover, these techniques require a large signal dataset and have difficulties tracking time-variant imperfections.

This thesis investigates the effectiveness of the conventional DSP algorithms in complex scenarios where multiple imperfections occur, representing its contribution's starting point. Then, a new DSP approach that aims to globally compensate for multiple imperfections is developed. In addition, a technique seeking to benefit from the advantages of both DSP and ML/DL is introduced. It consists of a model-based parametric network that can globally compensate for multiple imperfections of the coherent optical chain.

The thesis is structured into four chapters as follows.

Chapter 1 provides an introduction to the main concepts of coherent optical communications. It starts with a chronological review of optical fiber communications and then discusses different network topologies. Next, the principal elements and concepts of coherent optical systems are described, starting from the transmission to the optical channel and the receiver. Finally, the chapter states the objectives of the thesis.

Chapter 2 starts investigating the imperfections and the benchmark DSP algorithms used for compensation. Each effect is mathematically described, and its impact is analyzed. Then, some benchmark compensation algorithms are indicated. The chapter ends with an investigation of the effectiveness of the conventional DSP compensation algorithms in the presence of multiple imperfections. This is the basis for the investigations from the last two chapters.

Chapter 3 aims to alleviate the problems occurring when multiple imperfections are present by introducing an original DSP technique that mitigates all the impairments considered globally. The results reported by simulations, comparison to the conventional approach, and experimental investigation prove the effectiveness of the global DSP approach.

Chapter 4 explores the ML/DL abilities to compensate for coherent optical systems' impairments. It introduces an original network architecture based on the imperfections' parametric model. In addition, a training technique that uses reduced signal datasets and avoids overfitting is proposed. The results obtained using simulations, comparison to the conventional DL and DSP approaches, and experimental investigation illustrate the advantages of this technique.

Finally, the thesis is concluded at the end of the manuscript by highlighting the main contributions and some future perspectives.

Chapter 1

Fundamentals of coherent optical communications

Information is at the core of our society. Multiple industries and services are dependent on the fast and reliable exchange of information, and communication systems are the pillars that support this information transfer. Moreover, emerging technologies like 5G and IoT require more and more transmission capacity. Figure 1.1 presents Cisco's global traffic demand forecast between 2017 and 2022. During this interval, the global demand was predicted to increase from below 150 exabytes (1 exabyte = 10^{18} bytes) per month in 2017 to approximately 400 exabytes per month in 2022. On the other hand, there is a stringent requirement for energy efficiency and sustainable technologies, accelerated by the increase in greenhouse gas emissions that lead to climate change. In this context, optical fiber communication has a key role, as it is thought to be the only technology able to respond to high data rates and energy efficiency requirements.

The first predictions about the possibility of sending communication signals over the

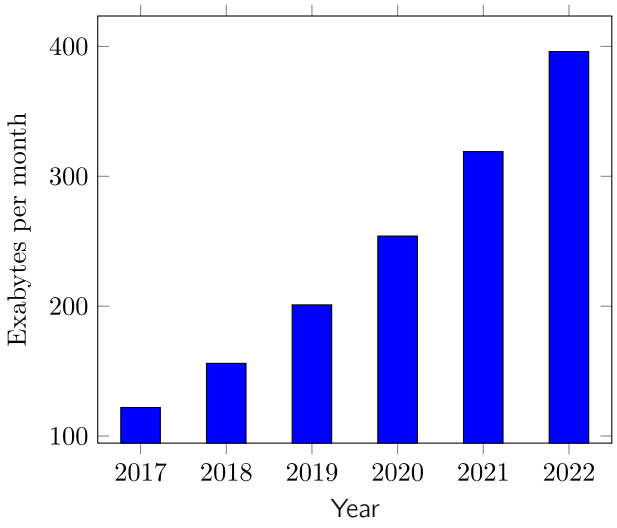

Figure 1.1 – Global traffic demand forecast [Cis21]

silica fiber and the first experimental demonstration were performed at the end of the '60s and the beginning of the '70s. At the end of the '70s, the first optical fiber systems were commercially operated [Agr+16]. Until now, fiber-optic communications evolved through different stages. First, the Intensity Modulation/Direct Detection (IM/DD) systems that use only the amplitude to encode information are imposed as the major commercial fiber transmission technology. This was mainly because of their simplicity and ability to respond to data rates demand. The IM/DD systems evolved in time from simple systems with data rates of a few Mb/s to more complex systems that used optical amplification, Dispersion Compensating Fibers (DCF), and multiplexing techniques such as Time Division Multiplexing (TDM) and WDM that could achieve data rates of dozens of Gb/s [Win+18]. In the 2000s, it was clear that these systems could not respond to the growing demand for high data rates imposed by the increase in Internet users and the quick expansion of mobile technologies. On the other hand, the Application-Specific Integrated Circuits (ASICs) benefited from a significant technological advance that started to permit DSP for fiber-optic communications [Lap+14]. In this context, the interest in coherent optical communications revived. Coherent optical communications were first investigated in the 80s [Lin+88; Oko+88], but the research was put on the background due to the difficulties associated with analog frequency and phase locking. Once these difficulties have been overcome, the era of coherent optical communications and DSP algorithms is underway [Win+18].

This chapter details the fundamentals of coherent optical communications and is organized as follows. First, the optical communications networks will be shortly described in section 1.1. Then a general description of a typical coherent optical system is given in section 1.2, where the transmitter and receiver architectures are presented, and the channel model is analyzed. Finally, the objectives of the thesis are discussed in section 1.3.

1.1 Optical communication networks

Optical communication networks can be classified into three main categories: Wide Area Networks (WANs) or core networks, Metropolitan Area Networks (MANs), and Local Area Networks (LANs) or access networks. In Figure 1.2, these three types of networks can be observed. This classification is mainly based on transmission distance, data rates, and cost. The core networks are, generally, long-distance networks that intercon-

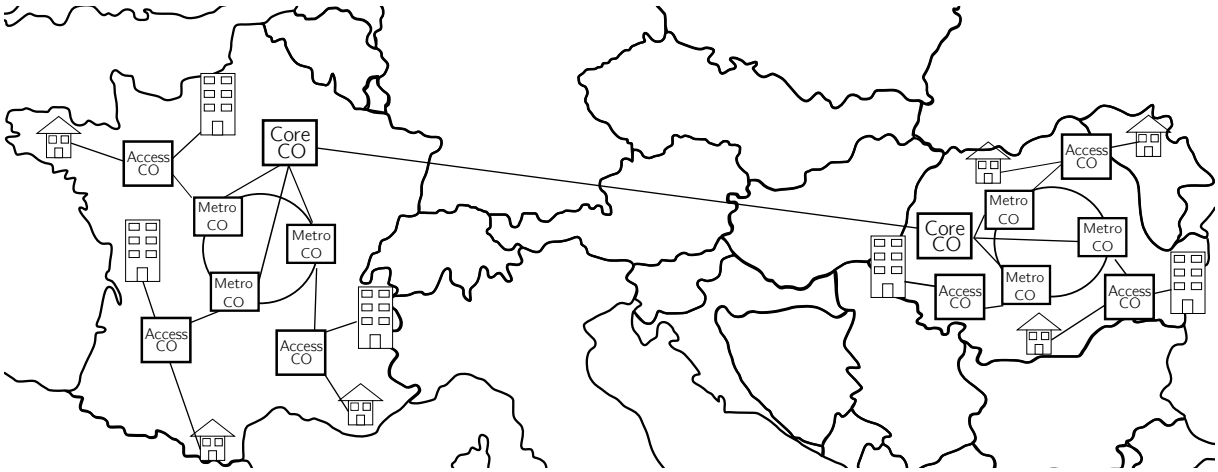

Figure 1.2 – Optical networks architectures, CO: Central Office

nect broad areas like countries and continents. These networks require a high data rate and have the highest cost. The access networks interconnect individual customers to the provider network. The data rates are the lowest compared to the other network types, the cost is restricted, and the coverage is limited to a few tens of kilometers at most. The MANs can be considered as an intermediary stage between the core and access networks regarding distance covered, data rate, and cost. MANs typically interconnect different regions or districts of a country.

Core networks have a distance coverage of more than 1000 kilometers. After the revival of coherent optical communications, these networks switched from the IM/DD to coherent detection, which is currently the primary technology. The coherent detection, together with PDM, WDM, and high-order modulations, allow core networks to reach enormous transmission rates. The achievable commercial data rates for a single channel are beyond 200 Gb/s aiming for 1 Tb/s [Buc+19; Lap+14; Mil+16; Ray+16]. This advance in transmission speed is driven by the research, as in laboratory tests, superior data rates were demonstrated [Por+22].

Metropolitan networks interconnect different areas located at a distance of several hundred kilometers. Considering the increase in global traffic, a switch to coherent detection systems is expected for this kind of network. Currently, the fiber transmission in the MANs can reach 40 Gb/s with a goal of 100 Gb/s in the future [ITU20].

Access networks cover relatively short distances up to 40 km [ITU18]. The central technology used is IM/DD, which can answer the demands and has lower cost. Considering the development of emerging technologies such as 5G and the IoT, the fiber-optic

is believed to become the main technology used by access networks. Currently, the commercial data rates provided by the fiber-optic access networks are up to 10 Gb/s.

1.2 Coherent optical systems

Coherent optical systems use, in addition to amplitude, carrier phase to encode information. This allows the employment of high-order modulations, which in addition to PDM, increase the spectral efficiency. Nevertheless, the receiver's complexity and cost are augmented compared to the IM/DD systems. In the following, the coherent optical system architecture is discussed.

The block diagram of a simplified coherent optical communication chain is depicted in Figure 1.3. The objective of a communication chain is to transmit a binary sequence from transmitter to receiver. This binary sequence is electrically modulated on the transmitter side, and different operations are performed by a DSP device. Then the signal is converted from the digital to the analog domain using a Digital-to-Analog Converter (DAC). Next, the resulting waveform is converted from the electrical to the optical domain using a laser source and an optical modulator and is transmitted over the optical channel. Generally, the channel consists of K_{span} spans, each having a typical length of 80 km with an optical amplifier. The signal is converted back to the electrical domain using a demodulator and another laser source on the receiver side. Then, by using an Analog-to-Digital Converter (ADC), the signal is transferred to the digital domain, where a DSP block performs a series of operations to recover the transmitted data.

The next subsections present the transmitter, optical channel, and receiver architecture and operations.

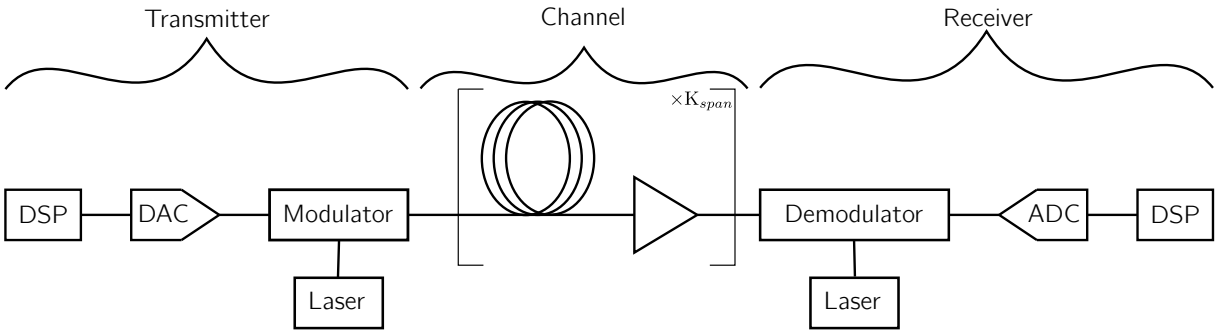

Figure 1.3 – Generic architecture of a coherent optical chain.

1.2.1 Transmitter

The transmitter's role is to encode the information bits, map the binary sequence into symbols, pre-compensate for imperfections, and modulate the optical carrier (electric-to-optical conversion). The transmitter comprises two main parts in optical communication systems: an electrical part and an optical one. The electrical part is similar to a typical transmitter used in electrical-based communications and, generally, consists of DSPs, ADCs, Radio Frequency (RF) amplifiers, and others. The optical part is specific, having the role of modulating the optical wave. It generally consists of a laser source and an electro-optical device that modulates the laser's wave.

The block diagram of Dual Polarization (DP) coherent optical transceiver is depicted in Figure 1.4. First, a binary sequence from the client's system is passed to the data interface, and then it is encoded using Forward Error Correction (FEC) codes. Then, the sequence is mapped into symbols using a particular modulation scheme. The symbols corresponding to both polarizations are digitally filtered, and then an analog-to-digital conversion is performed. After these steps are conducted in the electrical domain, optical modulation is performed using a continuous laser wave split by a Polarization Beam Splitter (PBS) and transmitted to the optical modulator. Finally, the optically modulated signals are recombined using a Polarization Beam Combiner (PBC), and the signal is transmitted.

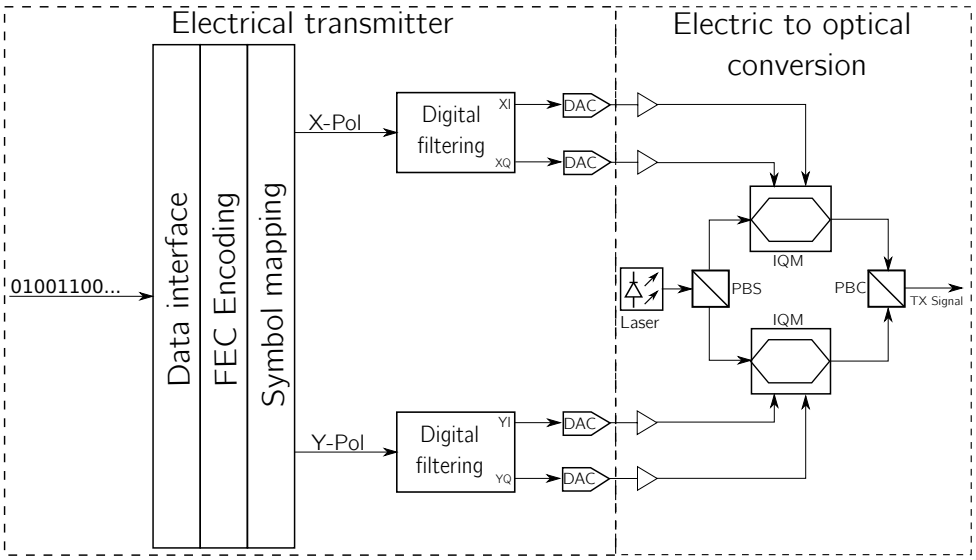

Figure 1.4 – Block diagram of a coherent optical transceiver, IQM: IQ Modulator, PBS: Polarization Beam Splitter, PBC: Polarization Beam Combiner.

1.2.1.1 Modulation formats

Originally, optical communications employed basic modulation formats that encoded information using the signal's power. Some of the most used modulation formats were the On-Off Keying (OOK) and Pulse Amplitude Modulation (PAM) [Agr12]. Then, coherent optical technology brought the ability to employ advanced modulation formats that encode information using both amplitude and phase components, producing two In-phase and Quadrature (IQ) signals. Current coherent optical communications use different Quadrature Amplitude Modulation (QAM) or QAM-based modulation formats that can be described as combining two PAM signals corresponding to the IQ components [Bos19]. Compared to the classical modulation formats employed until recently, QAM improves the Spectral Efficiency (SE). In addition, it benefits from an extra degree of freedom that leads to a more spread-out constellation for the same number of bits/symbol [Sim21].

A modulation format refers to a set of symbols denoted by $\mathbb{S} = \{s_1, \cdots, s_M\} \in \mathbf{C}^M$. Depending on the modulation format, each combination of bits is mapped to a particular complex-valued symbol s belonging to $\mathbb{S}$. The modulations can be employed using Single Carrier Modulation (SCM) or Multicarrier Modulation (MCM) formats. Even if there is an increased interest in MCM, especially the one using Orthogonal Frequency Division Multiplexing (OFDM) [Shi+08a; Shi+08b], the optical communications systems use mainly SCMs..

1.2.1.2 Baseband signal

The baseband continuous-time signal is obtained from the input symbols as follows:

$$x(t) = \sum_{n=-\infty}^{\infty} x[n]p(t - nT_{symb}), \tag{1.1}$$

where $x[n]$ is the transmitted symbol at the time $t = nT_{symb}$, $p(t)$ the pulse shape that satisfies the Nyquist's first criterion, and T_{symb} the symbol period.

Generally, a pulse shaping filter is used to limit the signals' bandwidth and avoid Intersymbol Interference (ISI). In coherent optical communications, it is generally accomplished by using Root Raised Cosine (RRC) filters. In addition to pulse shaping, a RRC filter is used on the receiver side for matched filtering. The frequency response

corresponding to the pulse shape $p(t)$ of such a filter can be expressed as in [Cub12]:

$$H(f) = \begin{cases} \sqrt{T_{symb}}, & \left(0 \leq |f| \leq \frac{1-\alpha_{rf}}{2T_{symb}}\right) \\ \sqrt{\frac{T_{symb}}{2}\{1 + \cos\left[\frac{\pi T_{symb}}{\alpha_{rf}}\left(|f| - \frac{1-\alpha_{rf}}{2T_{symb}}\right)\right]\}} & \left(\frac{1-\alpha_{rf}}{2T_{symb}} \leq |f| \leq \frac{1+\alpha_{rf}}{2T_{symb}}\right) \\ 0 & \left(|f| > \frac{1+\alpha_{rf}}{2T_{symb}}\right), \end{cases} \tag{1.2}$$

where f is the frequency and α_{rf} is the roll-off factor that determines the excess bandwidth.

Figure 1.5 presents the frequency response for different roll-off factors. For the case where $\alpha_{rf} = 0$, the pulse shape is known as the Nyquist pulse. It can be observed that increasing the roll-off factor introduces an excess bandwidth. Generally, the objective is to use roll-off factors as low as possible to increase spectral efficiency [Mor+15]. Still, a filter with a roll-off factor close to 0 cannot be efficiently implemented as it requires a high number of taps.

1.2.1.3 Laser source

The light sources are used to generate the optical carrier that is modulated to carry information. The light sources can be classified into Light-Emitting Diodes (LEDs) and semiconductor lasers (or laser diodes, injection lasers), depending on the recombination process. The recombination process is dominantly spontaneous in LEDs, while it is mainly

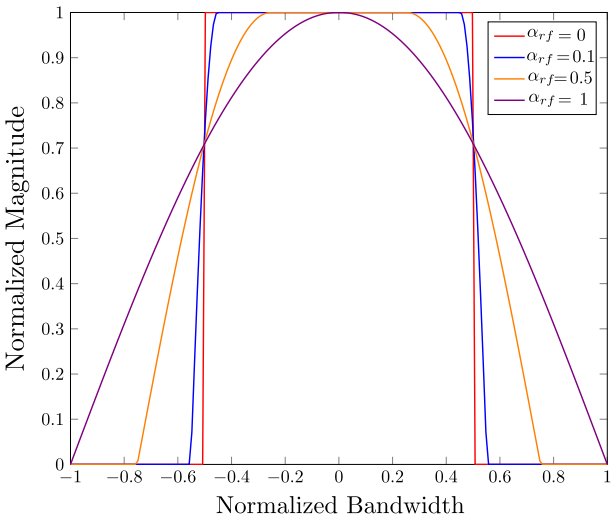

Figure 1.5 – The frequency response of RRC filters with different roll-off factors α_{rf}

done by stimulated emission in a semiconductor laser. Generally, LEDs are employed in low data rate applications. On the other hand, semiconductor lasers are usually operated in high data rate communications. Consequently, in coherent optical communications, semiconductor lasers are mainly used. The performance of the semiconductor lasers is mainly limited by the spontaneous emission that broadens the laser linewidth, typically measured at 3 dB attenuation, which results in a Lorentzian line shape (see Figure 1.6) [Bar+90; Di +10; Sai+81] of the laser as described by this expression:

$$E(t) = \sqrt{P_{source}} e^{j(\omega t + \phi(t) + \phi_0)}, \tag{1.3}$$

where $E(t)$ is the complex electrical field associated with the optical wave, P_{source} is the laser source power, ω is the laser angular frequency, $\phi(t)$ is the laser phase, and ϕ_0 is a random initial phase.

1.2.1.4 Optical modulation

Optical modulation is the process that allows the encoding of information on a carrier optical wave. It can be performed in two ways: directly modulating the laser source or using an external modulator. Direct modulation is less complex, but it is not adapted for high-speed coherent optical communications because of its frequency chirping related to the instantaneous change in power. As a consequence, coherent optical communication systems use mainly external modulation. The most versatile external modulator is the Mach-Zehnder Modulator (MZM) [Lia+05]. Its principle of operation is based on the linear electro-optic effect (Pokels effect), which states that the refractive index of some materials can be modified by applying an external electric field. Furthermore, the refrac-

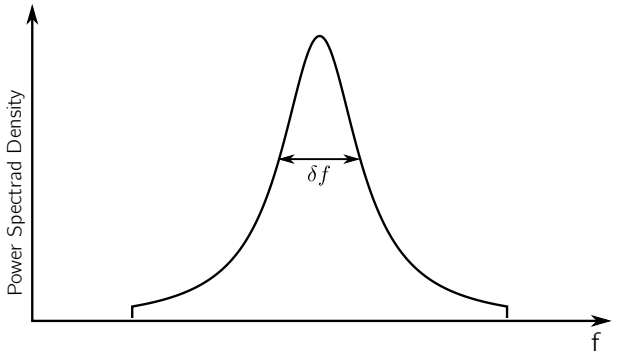

Figure 1.6 – The Lorentzian spectral shape of a laser corrupted by the phase noise, δf: Laser Linewidth

tive index change is proportional to the applied voltage and is instantaneous compared to the modulation operation, as its time scale is of the order of a few fs (1 fs = 10^{-15} s), while the one corresponding to the modulation is of the order of 10-100 ps (1 ps = 10^{-12} s) [Peu12]. One application that can be deducted from these properties is the realization of phase modulators by applying a voltage that modifies the material's refractive index, inducing a phase shift to the light wave propagating along the waveguide.

The architecture of the MZM is depicted in Figure 1.7. The input electrical field $E_{in}(t)$ is ideally split into two equal parts by a 3-dB coupler. Then, by applying a voltage $V(t)$ to each branch, where $i = 1$ for the upper branch and $i = 2$ for the lower branch, a phase shift is induced, and the wave is modulated. Then, at the output, the two branches' contributions are recombined by another 3-dB coupler resulting in the output electrical field $E_{out}(t)$. By this, the phase modulations are translated into amplitude modulation.

The phase shift induced by the driving voltage can be expressed as follows:

$$\phi_i(t) = \frac{\pi V_i(t)}{V_\pi}, \tag{1.4}$$

where V_π is the half-wave voltage that produces a π phase shift. The driving signals are defined as:

$$V_i(t) = V_{dc,i} + V_{pp,i} x_{norm,i}(t), \tag{1.5}$$

where V_{dc} is the Direct Current (DC) component, V_{pp} the peak-to-peak voltage, and

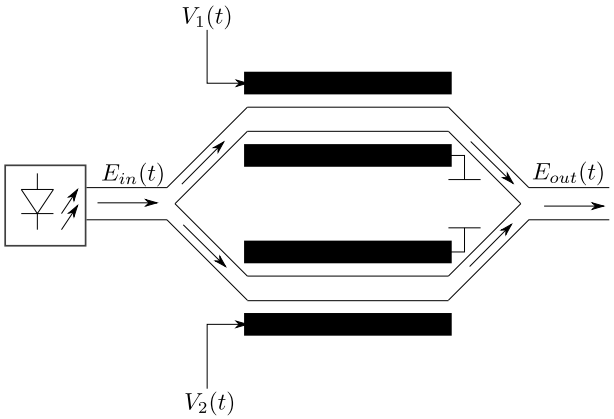

Figure 1.7 – Mach-Zehnder Modulator architecture. $E_{in}(t)$ and $E_{out}(t)$ are the electric fields associated with the optical wave at the input and output of the modulator, and $V_i(t)$ is the driving signal corresponding to $i - th$ arm

$x_{norm,i}(t) \in \left[-\frac{1}{2}, \frac{1}{2}\right]$ is the modulating signal's normalized waveform. When the MZM is operated in push-pull mode at the null point ($V_{dc,1} = V_{dc,2} = V_\pi$, $V_{pp,1} = V_{pp,2} = V_{pp}$, and $x_{norm,1}(t) = -x_{norm,2}(t) = \frac{x(t)}{2}$, we get the following relation between the input and output complex electric fields:

$$\begin{aligned} E_{out}(t) &= \frac{E_{in}(t)}{2}\left(e^{j\frac{V_\pi + V_{pp}x(t)}{2V_\pi}\pi} + e^{j\frac{V_\pi - V_{pp}x(t)}{2V_\pi}\pi}\right) \\ &= E_{in}(t)\sin\left(\frac{V_{pp}x(t)}{2V_\pi}\pi - \frac{\pi}{2}\right) \end{aligned} \tag{1.6}$$

By using a single MZM, Binary Phase Shift Keying (BPSK) and PAM modulations can be achieved. However, to be able to generate advanced modulation formats, an IQ Modulator (IQM) is needed. The IQM comprises two MZM and an electro-optic device that induces a $\frac{\pi}{2}$ phase shift for the Q component of the optical signal. In the ideal case, the relation between the input and the output of the IQM can be expressed as in [Nap+17]:

$$E_{out}(t) = \frac{E_{in}(t)}{2}\left[\sin\left(\frac{V_{pp}x_I(t)}{2V_\pi}\pi - \frac{\pi}{2}\right) + j\sin\left(\frac{V_{pp}x_Q(t)}{2V_\pi}\pi - \frac{\pi}{2}\right)\right], \tag{1.7}$$

where $x_I(t)$ and $x_Q(t)$ are the real and imaginary components of the original signal $x(t) = x_I(t) + jx_Q(t)$. In this way, the IQM can be used to generate any modulation format. In Figure 1.8, the architecture of the IQM is depicted. It can be seen that by applying two 4-PAM signals for each modulator, a 16-QAM signal is obtained at the output.

1.2.2 Optical channel

A typical optical chain comprises multiple spans (K_{span}) of optical fibers and amplifiers, as seen in Figure 1.9. These spans can stretch several hundreds of kilometers.

1.2.2.1 Optical fiber

An optical fiber is a thin dielectric waveguide made of silica to transmit information via light. Silica was identified as a suitable material for producing optical fiber in 1966 [Kao+66]. In a relatively short period, optical fiber production developed, and after 13 years, fibers with a loss of approximately 0.2 dB/km, approaching the minimum theoretical loss of silica, were produced. [Miy+79]. In Figure 1.10, the SMFs fiber attenuation for different wavelength values is depicted. In addition, the attenuation corresponding to

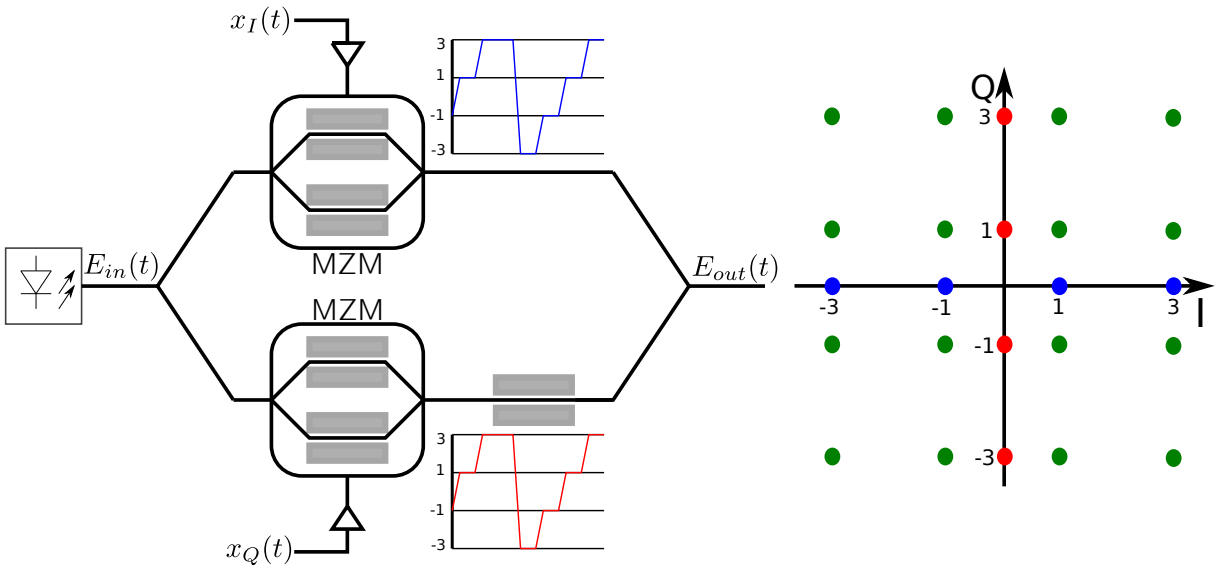

Figure 1.8 – IQ Modulator architecture and the generation of a 16-QAM signal using two 4-PAM signals

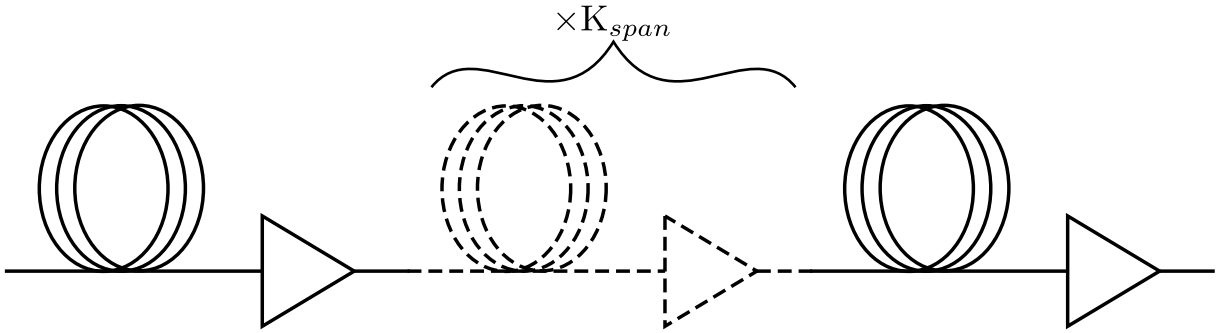

Figure 1.9 – The optical chain composed of multiple spans of fibers and amplifiers

transmission bands can be observed. It can be seen that the C band (1530-1565 nm) has the lowest attenuation.

A transmission fiber has three components: a coat, cladding, and core. The coat has the role of protecting the cladding and core against environmental conditions. The light is guided into the fiber by the total internal reflection. The light-guiding occurs as the refractive index of the core is higher than the cladding's [Sen+09]. The fiber can be of several types, including single-mode and multimode. This classification takes into consideration the core size. The SMF core size is reduced, allowing only a single path for the light. On the other hand, the multimode fibers' core is more prominent, allowing

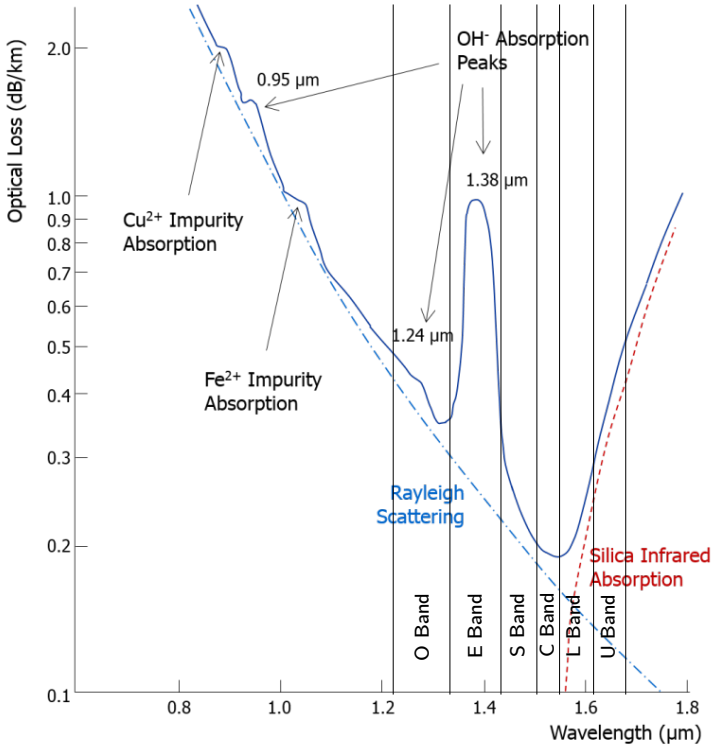

Figure 1.10 – SMF attenuation with wavelength and transmission bands [Opt17]

the light to reach several paths but exhibiting intermodal dispersion. In this thesis, the focus is on SMF as most optical communication networks are built using this type of fiber [Agr+16].

The propagation modes in fiber optics can be described starting from Maxwell's equations by considering the cylindrical symmetry and the boundary conditions at the core and cladding. In SMFs, a single mode can be transmitted due to the fabrication characteristics regarding the refractive index and the size of the core. The propagated mode on SMFs is the HE_{11} fundamental mode. To clarify the optical signals' propagation through fibers, the concept of wave packets is introduced in the following. The superposition of multiple plan waves of closely similar frequencies generates a packet of waves. In the case of optical communications, the wave packet is centered around the laser frequency. The following equation describes the wave packet $A(z,t)$ at time t and axial position z by superposing its spectral components [Fic21]:

$$A(z,t) \propto \int_{w=-\infty}^{\infty} \bar{A}(\omega) e^{j(\beta(\omega)z-\omega t)} d\omega, \tag{1.8}$$

where $\bar{A}(\omega)$ is obtained by Fourier transforming the wave function at $t = 0$, and $\beta(\omega)$ is the propagation constant. Another important definition refers to polarization which is the property of the transverse waves that specify the orientation of the oscillations [Shi+20]. If a line could describe the pulsation of the electrical field, we say that it is linearly polarized [Bor+13]. Generally, the wave's electric field describes an ellipse in the (x,y)-plane. However, considering a combination of two linear polarized fields along orthogonal axes, any polarization state can be expressed. Based on that, the single mode of propagation of SMF is defined as a combination of two orthogonal linear polarized modes. These two modes transmit independent streams of information over an optical channel, resulting in a PDM communication [Eva+92].

The wave packet equation (1.8) is only an approximation of fiber transmission. The transmission over optical fiber is better described by the coupled Nonlinear Schrödinger Equation (NLSE) [Agr00]:

$$\frac{\partial \mathbf{A}}{\partial z} = \underbrace{-\frac{\alpha}{2}\mathbf{A}}_{(1)} \underbrace{- j\frac{\Delta\beta_0(z)}{2}J(z)\mathbf{A} - \frac{\Delta\beta_1(z)}{2}J(z)\frac{\partial \mathbf{A}}{\partial \tau}}_{(3)} + \underbrace{\frac{\beta_2}{2}\frac{\partial^2 \mathbf{A}}{\partial \tau^2} + \frac{\beta_3}{6}\frac{\partial^3 \mathbf{A}}{\partial \tau^3}}_{(2)} \underbrace{- j\gamma\left[|\mathbf{A}|^2\mathbf{A} - \frac{1}{3}(\mathbf{A}^*\sigma_3\mathbf{A})\sigma_3\mathbf{A}\right]}_{(4)}, \tag{1.9}$$

where $\mathbf{A}$ is a Jones vector representing the wave packet, α denotes the attenuation, $\beta_i = \frac{\partial^i \beta}{\partial \omega^i}\Big|_{\omega=\omega_0}$, ω_0 the central angular frequency, $J(z)$ is a 2×2 unitary Jones matrix, τ is the time frame that moves along the wave-packet referential, σ_3 the third Pauli matrix, and γ the nonlinearity coefficient. It can be seen in eq. (1.9) that four terms describe fiber propagation. The term (1) represents the fiber attenuation, (2) the Chromatic Dispersion (CD), (3) the Polarization Mode Dispersion (PMD), and (4) the nonlinear Kerr effect. The first three terms correspond to the linear effects of fiber transmission, while the last to the nonlinear ones. These effects degrade communication performance and are highly investigated in the literature.

The current challenges related to the standard SMF transmission are related to the approaching of their information theory capacity limit, which is estimated at approximately 100-200 Tb/s [Agr+16]. In this context, important research advances have been made regarding the introduction of new technology for fiber optics, especially the Space Division Multiplexing (SDM) [Ric+13].

1.2.2.2 Optical amplifiers

The signals experience attenuation during the transmission over the fiber. Therefore, it is mandatory to ensure a received signal power higher than the receiver sensitivity to exploit the transmitted information. To meet these challenges, two different techniques were considered during the optical fiber communications evolution. First, from a chronological point of view, the Optical-Electrical-Optical (OEO) regenerators were considered. In this case, the optical signal is converted to an electrical signal, and the required compensations are achieved. Then the signal is again converted to the optical domain. Despite this approach's effectiveness, its cost is prohibitive and would have limited the extension of fiber-optic systems. The second option uses unregenerated systems by directly amplifying the optical systems. This approach appeared with the production of the first Erbium-Doped Fiber Amplifiers (EDFAs) in the late 80s [Des+87; Mea+87]. Therefore, by using optical amplifiers, the need for expensive OEO is limited to some continental long-haul systems. Furthermore, the average amplifier has a gain of approximately 20 dB, which means that, generally, an amplifier is used at about every 80 km [ITU11].

The EDFA amplifies the signal using the population inversion. The amplification process can be seen in Figure 1.11, where the energy level diagram of Erbium ions is represented. A pump laser operating at 980 or 1480 nm pushes the ion into an excited energy state. In the case of a pump laser at 980 nm, the ion arrives at an upper energy level, then goes to the metastable level by radiating heat. Finally, the ion goes to the lower

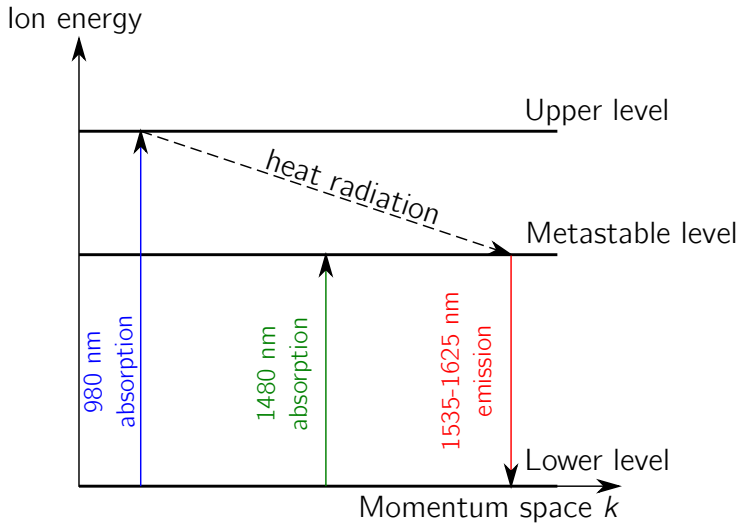

Figure 1.11 – Energy level diagram of Erbium ions

energy level producing a stimulated emission. In the case of the 1480 nm pump, the ion goes directly to the metastable level, then produces a stimulated emission by transiting to the lower energy level. On the top of the stimulated emission, EDFA introduces some noise characterized by its Noise Figure (NF), which typically ranges from 4 to 6 dB [Sil17]. The reason behind the noise introduction by EDFA is the Amplified Spontaneous Emission (ASE) that emerges when an ion randomly returns to the lower energy level state. ASE is modeled as an Additive White Gaussian Noise (AWGN) with a Power Spectral Density (PSD) denoted as N_{ASE} which can be defined as [Ess+10]:

$$N_{ASE} = N_A(e^{\alpha L_A} - 1)h\nu_s n_{sp}, \tag{1.10}$$

where N_A is the number of amplifiers existing on the transmission line, L_A the length of a fiber span, $h\nu_s$ is the photon energy, and $n_{sp} \leq 1$ the spontaneous emission factor [Bja93; Bor+13]. The ASE noise introduced by the EDFA degrades the Optical Signal-to-Noise Ratio (OSNR), which can be defined in relation with it as follows:

$$OSNR = \frac{P_s}{2B_{ref}N_{ASE}} = \frac{P_s}{\sigma^2_{ASE}}, \tag{1.11}$$

where P_s is the total average signal power, B_{ref} is a reference bandwidth (usually 0.1 nm), and σ^2_{ASE} is the variance of ASE noise.

During the time, multiple amplifiers were developed like Raman amplifiers and Semiconductor Optical Amplifiers (SOAs), but EDFA remains the most deployed one due to its excellent compatibility with transmission fibers, low cost, and energy efficiency [Bec+99].

1.2.3 Receiver

The receiver's role is to recover the transmitted data. The receiver has a particular architecture in optical communications compared to purely electrical-based receivers. Similar to the optical transmitter, it contains optical and electrical parts. The optical front end and the classical electrical receiver are the two main building blocks of the optical receiver. The optical front end converts the optical signal to the electrical domain and performs the demodulation. After this block, the down-converted electrical signal is obtained. Then, this signal is transmitted to a classical receiver which generally consists of RF amplifiers, ADCs, and DSPs. The role of these blocks is to transfer the signal back into the digital domain, perform the synchronization, compensate for different impair-

ments and effects of the global optical chain, and detect the originally transmitted data.

The configuration of a generic DP coherent receiver is depicted in Figure 1.12. The incoming signal is decomposed in its orthogonal polarization signals and is mixed with a Continuous Wave (CW) originating from a Local Oscillator (LO). In coherent optical systems, the two components are mixed using a 90° hybrid and two balanced photodetectors. After the photodetection, the electrical baseband signal can be recovered. Then the signal is converted by some ADCs, and the DSP performs multiple operations like synchronization, impairments compensation, symbol demapping, and FEC decoding. Finally, the recovered binary stream is transferred to the client's application.

1.2.3.1 Optical demodulation

In this thesis, intradyne detection is considered since it requires a minimum signal processing bandwidth, and it does not imply a frequency locking of the lasers, which may be problematic [Der92]. In an intradyne receiver, the phase is unlocked, and its estimation is performed in the electrical domain by DSP module. The following details the optical demodulation process for a Single Polarization (SP) system.

The received signal is mixed with the contribution of the LO. The optical down-

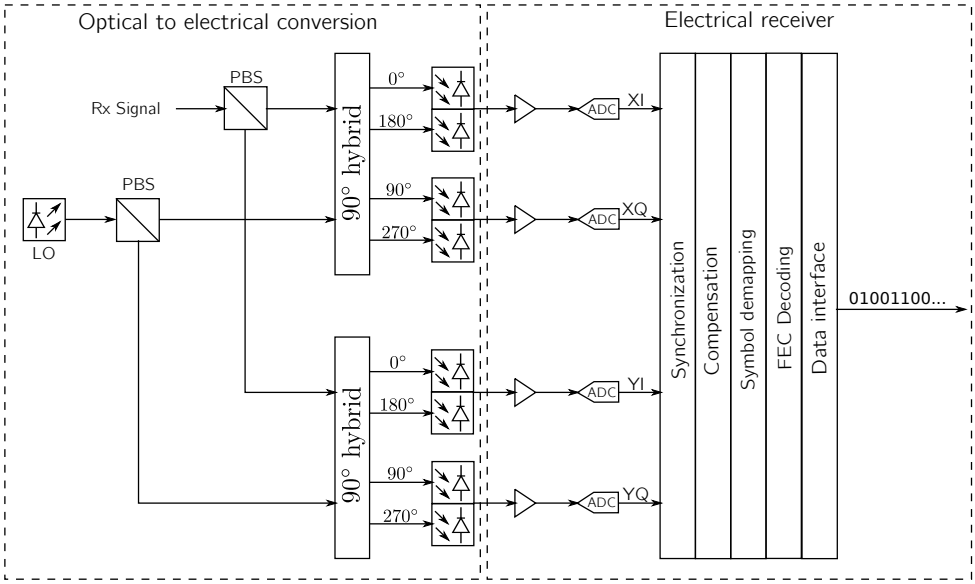

Figure 1.12 – The configuration of a generic DP coherent optical receiver, LO: Local Oscillator

conversion is performed using a 90° optical hybrid and two balanced photodetectors for each polarization signal. The 90° hybrid is a device assembled by optical fibers, couplers, and a 90° phase shifter [Gar91; Jeo+10]. The detailed diagram of such a system can be seen in Figure 1.13. This setup can recover both amplitude and phase information on the receiver side, and any modulation format could be detected [Ho05].

Let us consider the electric complex field of the transmitted signal as follows:

$$E_S(t) = A_S(t)e^{j(\omega_S t+\phi_S(t)+\phi_{n1}(t))}, \tag{1.12}$$

where $A_S(t)$ is the complex amplitude, ω_S is the optical carrier angular frequency, $\phi_S(t)$ is the signal phase, and $\phi_{n1}(t)$ is the phase noise introduced by the transmitter laser. Similarly, the LO contribution is expressed as:

$$E_{LO}(t) = A_{LO}e^{j(\omega_{LO}t+\phi_{n2}(t))}, \tag{1.13}$$

where A_{LO} is the complex constant amplitude, ω_{LO} is the angular frequency of the LO, and $\phi_{n2}(t)$ is the phase noise of the LO. By using the 90° optical hybrid from Figure 1.13, four components of the electrical field are obtained from two inputs. These components

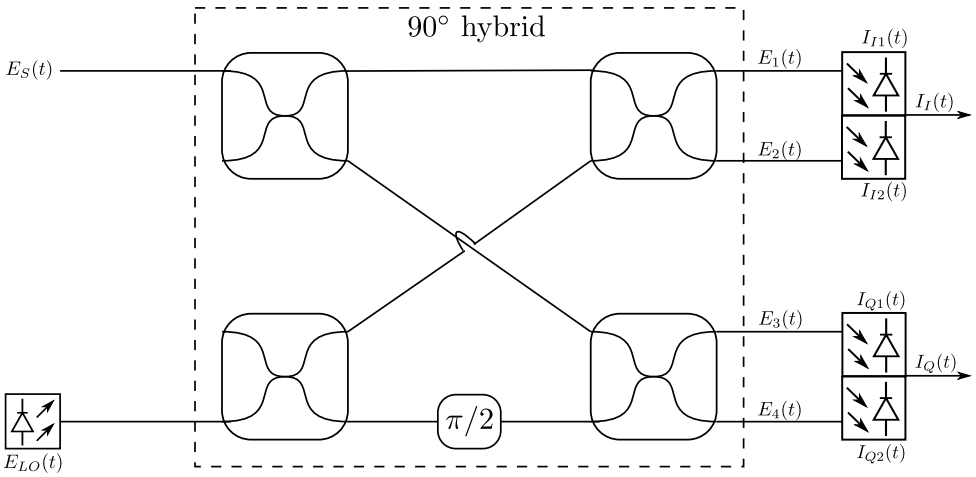

Figure 1.13 – The detailed diagram of a setup consisting of a 90° hybrid and a balanced photodetector used in SP coherent optical systems

are expressed with respect to $E_S(t)$ and $E_{LO}(t)$ as follows:

$$E_{1,2}(t) = \frac{1}{2}\left(E_S(t) \pm E_{LO}(t)\right), \tag{1.14}$$

$$E_{3,4}(t) = \frac{1}{2}\left(E_S(t) \pm jE_{LO}(t)\right). \tag{1.15}$$

The output photocurrents from the diodes can be expressed as follows [Kik15]:

$$\begin{aligned} I_{I_{1,2}}(t) &= R\left[\Re e\{\frac{A_S(t)e^{j\omega_S t+\phi_S(t)+\phi_{n1}(t)} \pm A_{LO}e^{j\omega_{LO}t+\phi_{n2}(t)}}{\sqrt{2}}\}\right]^{ms} \\ &= \frac{R}{2}\left[P_S(t) + P_{LO} \pm 2\sqrt{P_S(t)P_{LO}(t)}\cos(\Delta\omega t + \phi_S(t) + \phi_n(t))\right], \end{aligned} \tag{1.16}$$

$$\begin{aligned} I_{Q_{1,2}}(t) &= R\left[\Im m\{\frac{A_S(t)e^{j\omega_S t+\phi_S(t)+\phi_{n1}(t)} \pm A_{LO}e^{j\omega_{LO}t+\phi_{n2}(t)}}{\sqrt{2}}\}\right]^{ms} \\ &= \frac{R}{2}\left[P_S(t) + P_{LO} \pm 2\sqrt{P_S(t)P_{LO}(t)}\sin(\Delta\omega t + \phi_S(t) + \phi_n(t))\right], \end{aligned} \tag{1.17}$$

where ms denotes the mean square with respect to optical frequencies, R is the responsivity of the photodiodes, $P_S(t)$ is the signal power, P_{LO} the LO power, $\Delta\omega$ the angular frequency difference between the two lasers, $\phi_S(t)$, and $\phi_n(t) = \phi_{n1}(t) + \phi_{n2}(t)$ are the phase of the transmitted signal, and the accumulated phase noise, respectively. Finally, the output photocurrents from the balanced photodetectors are given by [Kik15]:

$$I_I(t) = I_{I,1}(t) - I_{I,2}(t) = R\sqrt{P_S(t)P_{LO}}\cos\left(\Delta\omega t + \phi_S(t) + \phi_n(t)\right), \tag{1.18}$$

$$I_Q(t) = I_{Q,1}(t) - I_{Q,2}(t) = R\sqrt{P_S(t)P_{LO}}\sin\left(\Delta\omega t + \phi_S(t) + \phi_n(t)\right). \tag{1.19}$$

Using this, we can restore the complex signal as follows:

$$I_C(t) = I_I(t) + jI_Q(t) = R\sqrt{P_S(t)P_{LO}}e^{j(\Delta\omega t+\phi_S(t)+\phi_n(t))}. \tag{1.20}$$

The extension to a DP coherent optical system is straightforward, and it can be done by splitting the two signals arriving on the fiber and from the LO in two orthogonal polarization and performing the optical demodulation by using two structures, as the one from Figure 1.13. After these steps, the baseband signal containing both polarizations' contributions is sent to the DSP for further processing.

1.2.3.2 Digital signal processing

After the optical front-end, the analog electric signal is converted to the digital domain using ADCs. As all the imperfections degrade the signal in the communication chain, a set of operations is performed to recover the transmitted data. First, the synchronization is operated, then the impact of different imperfections impacting the signal is compensated for, and the data is detected. These operations are detailed in the following.

— Synchronization aims to correct the delay and timing error between the transmitted and received signals. It is generally achieved in two steps. First, a coarse synchronization (acquisition) that can be performed using signal cross-correlation and interpolation [Bor+14; Sav10] is employed. Then a finer synchronization can be implemented using both non-data-aided [Gar86] or data-aided [Mue+76] techniques.

— Compensation is needed in order to combat the impact of different impairments that degrade the transmitted signal. This generally includes channel equalization, carrier frequency and phase recovery. A detailed analysis of the imperfections' impact and compensation is developed in Chapter 2.

— Detection is performed to recover the actual transmitted data. Generally, during this process, the received signal's symbols are classified as one of the elements of the constellation set $\mathbb{S}$.

After these steps, the FEC decoding is performed, and the information is sent to the client.

1.2.3.3 Performance metrics

Different methods can be used for performance evaluation in an optical communication system. First, the graphical representations of various signal aspects (time and frequency representations, signal constellation, etc.) can provide important insights into the system's performance. However, quantitative criteria should be introduced to evaluate the quality of communications. Some of them are applied before the signal's detection, using the signal after the compensation as a basis. These criteria are independent of the modulation format and reasonably estimate the system's final performance. However, the final objective of a transmission system is to recover the transmitted data. Consequently, the metrics computed after the detection express the final performance of an optical system. Nevertheless, these two classes of metrics are generally correlated. In simple situations

(e.g. AWGN channel), there are direct analytical relations between some of these metrics [Sch+11]. In this study, we focus on the criteria detailed in the following.

Pre-detection Metrics

— Mean Squared Error (MSE) is a metric that measures the average of the squared errors between real and estimated values. It is mostly used to assess the performance of an estimator. For example, the MSE between the real transmitted symbols and the estimated received symbols before detection can be expressed as:

$$\text{MSE} = \frac{1}{N}\left(\sum_{n=0}^{N-1} |x[n] - \hat{x}[n]|^2\right) \tag{1.21}$$

where $x[n]$ and $\hat{x}[n]$ are the $n-th$ transmitted and compensated symbols of the signal, respectively, and N is the total number of symbols.

— Error Vector Magnitude (EVM) is a quantitative metric that describes the impact of imperfections. It is represented by the vector between the ideal constellation symbol and the impaired received symbol, as can be seen in Figure 1.14. It can be

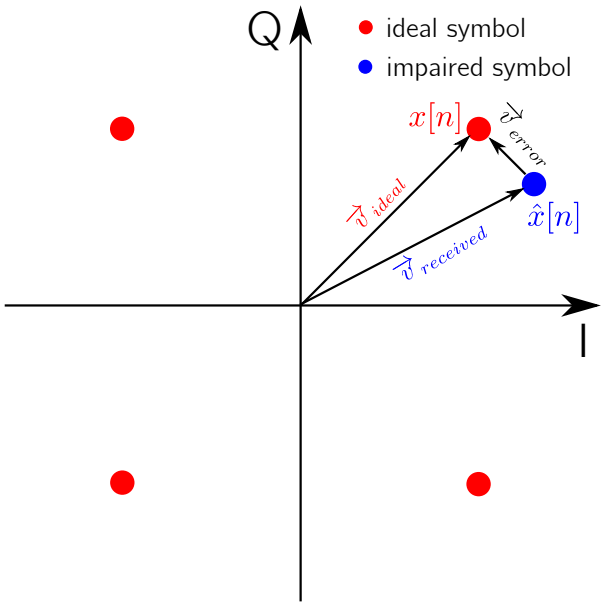

Figure 1.14 – EVM representation

obtained as follows:

$$\text{EVM} = \sqrt{\frac{\sum_{k=0}^{N-1} |x[n] - \hat{x}[n]|^2}{\sum_{k=0}^{N-1} |x[n]|^2}}. \tag{1.22}$$

The EVM is typically expressed in percentages. In this work, the Third Generation Partnership Project (3GPP) EVM reference [36118] will be used as a performance bound.

Post-detection Metrics

— Symbol Error Rate (SER) is a metric that quantifies the number of erroneous symbols from the total number of symbols. It can be defined as:

$$\text{SER} = \frac{\|x[n] - x_{det}[n]\|_0}{N}, \tag{1.23}$$

where $x_{det}[n]$ refers to the $n-th$ detected symbol, and $\|.\|_0$ denotes the L0-Norm.

— Bit Error Rate (BER) is the final metric of the communications systems. It is related to SER, but instead of symbols, it evaluates the number of erroneously received bits from the total transmitted bits:

$$\text{BER} = \frac{\|b_{tx}[n] - b_{rx}[n]\|_0}{N_{bits}}, \tag{1.24}$$

where $b_{tx}[n]$ and $b_{rx}[n]$ denote the $n-th$ transmitted and detected bits, and N_{bits} is the total number of bits. In this thesis, a pre-FEC BER threshold ("BER TH") of 4×10^{-3} is considered to obtain a post-FEC BER below 10^{-14} as indicated in Appendix I.9 of International Telecommunication Union - Telecommunication Standardization Sector (ITU-T) G975.1 recommendation [ITU04].

1.3 Objective of the thesis

This chapter analyzed the theoretical aspects of coherent optical communications. It can be stated that coherent optical technology is a key technology that could deliver very high data rate transmissions to respond to the customers' demands. At these data rates, imperfections can have a significant impact. Multiple impairments can impact the optical chain on the transmitter and receiver sides. Moreover, the channel-induced effects limit

the performance of the communications. These imperfections can be classified into two major groups: nonlinear and linear. Both have an important impact on the performance and have to be compensated for to achieve a good Quality of Service (QoS). However, while multiple DSP approaches have been operated in real-time communications to compensate for the linear imperfections impact, the compensation of the nonlinear effects cannot be implemented in real-time long-haul high data rate communications at this moment due to high computational requirements [Min+22]. Consequently, in this thesis, the main focus will be on the linear effects of the fiber channel, with perspectives on considering the nonlinear ones.

In the last two decades, the manufacturing of electronic devices has constantly improved, allowing the real-time compensation of coherent optical systems' imperfections using DSP algorithms. Several algorithms have their origin in the field of wireless communication, and many others were developed to compensate for specific impairments of the optical communication chain.

Recently, the ML/DL algorithms have proved their effectiveness in different research and engineering tasks. These techniques are data-driven, meaning they do not have knowledge of the system's model but achieve the objectives by learning from the data. The ML/DL networks are very flexible, as modifying their structures and adapting to different scenarios is easy. ML and DL approaches represent a hot research topic, and their applicability was also extended to coherent optical communications applications.

Considering all of these, the current thesis proposed three major objectives that will be detailed in the following:

— The first objective is to analyze the coherent optical systems' linear imperfections impact and the state-of-the-art algorithms used for compensations. Generally, the conventional approach consists of specialized algorithms designed to compensate for a particular imperfection. When multiple impairments occur, the conventional approach consists of cascading multiple DSP compensation algorithms. In this work, we investigate the effectiveness of this approach in situations where multiple imperfections occur.

— The second objective is to develop a new approach to linear imperfection compensation. This approach will also be based on DSP algorithms and consists of a joint estimation and compensation of all considered linear imperfections, with the aim of achieving better statistical performance.

— The third objective consists of developing a network that jointly compensates for

all the considered linear imperfections of the coherent optical systems. In addition, the model knowledge will be incorporated into the network architecture. By doing this, the aim is to combine the advantages of the DSP and ML/DL while minimizing their issues.

Chapter 2

Linear imperfections impact and state-of-the-art compensation techniques

Coherent optical systems may be impaired by multiple imperfections that could severely degrade communication performance. These imperfections can originate from multiple sources like the devices' manufacturing process, optical channel effects, aging of the equipment, etc. Imperfections can occur at any point in the communication chain, as they may impact electrical and optical-based devices. Consequently, a major area of research focuses on their compensation, which can also be performed in multiple manners. Even if there are different approaches dealing with imperfections mitigation, traditionally, impairments are compensated for by using DSP algorithms [Zha+19b]. In this chapter, we propose to analyze the impact of linear imperfections of the coherent optical chain and some benchmark DSP compensation techniques used to mitigate them.

2.1 Preliminaries

In this chapter, the impact of imperfections and compensation techniques are described by using the following generic signals: $\mathbf{x}_{in}$ and $\mathbf{x}_{out}$. $\mathbf{x}_{in}$ refers to a signal at the input of a system with imperfections. $\mathbf{x}_{out}$ describes the same signal at the system's output after being modified by impairments. Both signals can be defined similarly to:

$$\mathbf{x} = \begin{bmatrix} x[0] & x[1] & \dots & x[N-1]^T \end{bmatrix}, \tag{2.1}$$

where $\mathbf{x} \in \mathbb{C}^N$ and $\mathbf{x} = \mathbf{x}_I + j\mathbf{x}_Q$, N represents the total number of symbols, and $(.)^T$ denotes the transpose operation.

2.1.1 Signal Model

This chapter focuses on (widely) linear imperfections. For this class of impairments, the relationship between $\mathbf{x}_{in}$ and $\mathbf{x}_{out}$ can be described by:

$$\tilde{\mathbf{x}}_{out} = \mathbf{H}(\xi)\tilde{\mathbf{x}}_{in}, \tag{2.2}$$

where $\tilde{\mathbf{x}} = [\Re e(\mathbf{x}^T), \Im m(\mathbf{x}^T)]^T \in \mathbb{R}^{2N}$ is an augmented vector that contains the real and imaginary parts of $\mathbf{x}$ and $\mathbf{H}(\xi)$ is a $2N \times 2N$ real-valued matrix.

This chapter focuses more specifically on 5 impairments occurring in a coherent optical chain. These impairments are:

— IQ imbalance
— Laser Phase Noise (PN)
— CD
— PMD
— Carrier Frequency Offset (CFO).

These imperfections may be classified as corresponding to multiple criteria. One essential criterion in this work is time evolution. If a given impairment exhibits slow dynamics, it can be assumed as static. For any other kind of dynamics, the impairment is considered time-variant. Another key criterion is the impact on the two polarization signals. Some imperfections have a similar impact on the two signals, others impact them independently, while PMD has a coupling effect on the signals. In Table 2.1, a possible classification according to these criteria is found.

2.1.2 Compensation

The objective of a compensation algorithm is to recover $\mathbf{x}_{out}$ from $\mathbf{x}_{in}$, when the matrix $\mathbf{H}(\xi)$ is unknown.

The compensation algorithms may be classified considering multiple criteria. One of

Table 2.1 – Parameters classification with respect to the time evolution and polarization impact

Classif.	**PN**	**IQ imbalance**	**PMD**	**CD**	**CFO**
Time ev.	Variant	Static	Variant	Static	Static
Pol. imp.	Similar	Different	Coupled	Similar	Similar

the criteria is the use of known data on the receiver side. Such a classification is detailed in the following:

— *Data aided* technique: the compensation algorithm uses some known data such as preamble or/and pilots.
— *Blind* technique: the algorithm exploits the statistical properties of the signal and does not use any additional data.
— *Decision-aided* technique: the algorithm exploits the knowledge of the symbol constellation $\mathbb{S}$.
— *Hybrid* technique: the algorithm switches from a data-aided to a blind or decision-aided mode.

The following sections present the signal model and the associated compensation algorithms for the most critical imperfections and impairments occurring in a coherent optical chain.

2.2 IQ imbalance

IQ imbalance is one of the main impairments that can occur in a coherent optical communication [Far+13]. It arises if the power balance or the orthogonality between I and Q signals are not respected [Tub+05]. It can appear both on the transmitter and receiver sides. Moreover, it can be originated from electrical or/and optical devices.

On the transmitter side, the IQ imbalance can originate on the electrical part from different points, especially from the amplifiers that induce gain differences between the IQ signals. Moreover, during the optical modulation, an IQ imbalance can arise because of unequal split and/or combining ratio between the branches, different lengths for the circuit used to apply the driving voltages, unstable bias control, or diverse manufacturing problems of the IQM [Ngu+17; Zha+19a].

On the receiver side, the IQ imbalance can originate from the electrical part, mostly because of the imperfections related to the amplifiers, but not limited to that. On the optical side, imperfections can come from the 90° optical hybrid, where the couplers may not be perfectly balanced or the phase control is not properly performed. In addition, the mismatch of the photodiodes could introduce some IQ imbalance [Far+13; Zha+19a].

2.2.1 Signal model

The time-domain impact of the IQ imbalance can be modeled as in [Jal+19; Liu98; Meh+18]:

$$x_{out}[n] = \mu x_{in}[n] + \nu x_{in}^{*}[n]. \tag{2.3}$$

The distortion parameters μ and ν are related to the actual amplitude and phase imbalance as follows [Tan+07]:

$$\mu = \cos\left(\frac{\vartheta}{2}\right) + jg\sin\left(\frac{\vartheta}{2}\right), \tag{2.4}$$

$$\nu = g\cos\left(\frac{\vartheta}{2}\right) - j\sin\left(\frac{\vartheta}{2}\right), \tag{2.5}$$

where g refers to the gain difference between the two I and Q signals, and ϑ to the phase deviation from the ideal 90°. Furthermore, the gain imbalance is defined by [Tar+05]:

$$g = \frac{g_I - g_Q}{g_I + g_Q}, \tag{2.6}$$

where g_I and g_Q stand for the gain of I and Q signals.

In order to better understand the impact of IQ imbalance, in Figure 2.1 we consider its impact over a 4-QAM ideal constellation. In Figure 2.1a, the I component of the complex signal has a gain variation compared to the ideal case. It can be observed that this gain imbalance leads to a horizontal widening of the constellation. Next, in Figure 2.1b, the Q component has a gain variation. This leads to a vertically broadening of the constellation. Finally, in Figure 2.1c, a phase deviation from the ideal 90° is introduced, which conducts to the loss of the orthogonality of the signals. As it can be observed, a single type of IQ imbalance leads to a constellation distortion. However, in practice, the signal is usually impaired by a combination of these distortions. This is an important problem, as it is possible to misinterpret the symbol on the receiver side. Moreover, as the modulation order increases, the impact of the IQ imbalance can be more severe as the distance between the constellation points is reduced. This can be deducted from Table 2.2, where the impact of the receiver IQ imbalance for different QAM orders and without any compensation as a function of 1 dB OSNR penalty at a BER of 10^{-2} is summarized. However, it is important to notice that in the reference from Table 2.2, the IQ imbalance

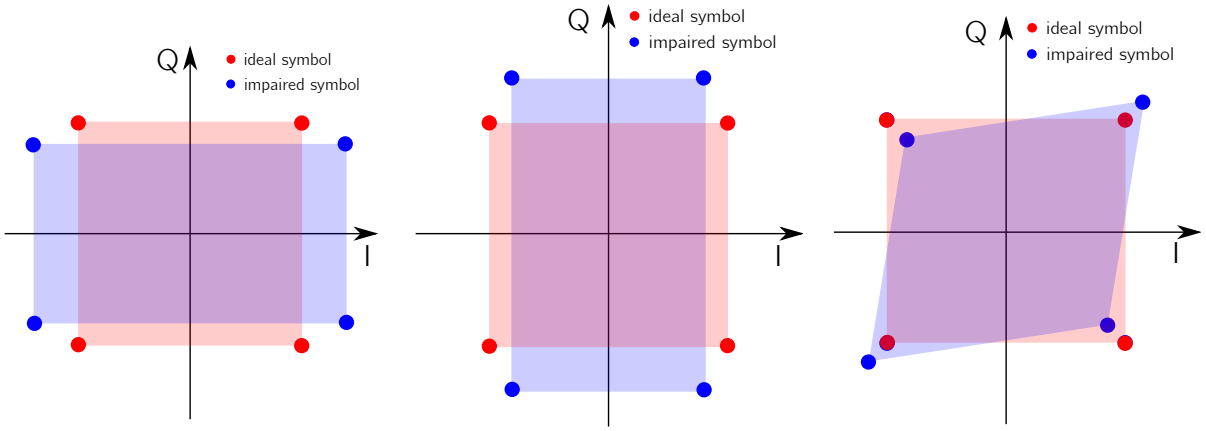

(a) Gain imbalance for the I component

(b) Gain imbalance for the Q component

(c) Phase deviation from the ideal 90°

Figure 2.1 – IQ imbalance impact on an ideal 4-QAM constellation

Table 2.2 – The impact of the receiver IQ imbalance for different QAM orders as a function of 1 dB OSNR penalty at a BER of 10^{-2} without any compensation [Far+17]

Modulation format	g **[dB]**	ϑ **[deg.]**
4-QAM	3.8	28
16-QAM	1.6	10.5
64-QAM	0.6	4
256-QAM	0.2	1.4

is modeled differently, as follows:

$$x_{out}[n] = x_{I,out}[n] + jx_{Q,out}[n] = g_I x_{I,in}[n] + g_Q x_{Q,out}[n] e^{j\left(\frac{\pi}{2}+\vartheta\right)}. \tag{2.7}$$

Another important aspect regarding the imperfections is their time evolution and frequency dependence. In the case of IQ imbalance, the time-evolution is very slow compared to the signal's, and it can be assumed static [Ma+15]. It is also important to note that the signal model in (2.3) leads to a simple approximation for the IQ imbalance impairment. In particular, more realistic models also include the presence of frequency-selective and/or nonlinear IQ imbalance [Skv+20].

2.2.2 Compensation

Multiple approaches have been proposed to compensate for the IQ imbalance in coherent optical communications. In the following, some of the DSP algorithms used for IQ imbalance compensation are reviewed.

One of the benchmark algorithms is based on the Gram-Schmidt Orthogonalization Procedure (GSOP) [Hay08]. This approach was investigated and demonstrated for the case of coherent optical communications in [Fat+08]. GSOP is a blind compensation algorithm that is based on the second-order statistics of the signal. Specifically, this method exploits the fact the real and imaginary parts of the input samples are orthogonal, so $\mathrm{E}\left[\mathbf{x}_{I,in}^2\right] = \mathrm{E}\left[\mathbf{x}_{Q,in}^2\right]$ and $\mathrm{E}\left[\mathbf{x}_{I,in}\mathbf{x}_{Q,in}\right] = 0$, where by $\mathrm{E}\left[.\right]$ is denoted the expected value. To force this property, the GSOP technique consists in linearly transforming the non-orthogonal samples into a set of orthogonal ones. The non-orthogonal IQ components of the impaired signal are denoted by $\mathbf{x}_{I,out}$ and $\mathbf{x}_{Q,out}$. To orthogonalize these signals, GSOP performs the following operations:

$$\hat{x}_{I,in}[n] = \frac{x_{I,out}[n]}{\sqrt{P_I}} \tag{2.8}$$

$$x^{'}_{Q,out}[n] = x_{Q,out}[n] - \frac{\rho x_{I,out}[n]}{P_I} \tag{2.9}$$

$$\hat{x}_{Q,in}[n] = \frac{x'_{Q,out}[n]}{\sqrt{P_Q}}, \tag{2.10}$$

where $\rho = \frac{1}{N}\sum_{n=0}^{N-1} x_{I,out}[n] \cdot x_{Q,out}[n]$ is the correlation coefficient, $P_I = \frac{1}{N}\sum_{n=0}^{N-1} x_{I,out}^2[n]$, and $P_Q = \frac{1}{N}\sum_{n=0}^{N-1} x_{Q,out}^{'2}[n]$.

In Figure 2.2, we can observe a 4-QAM constellation impacted by receiver IQ imbalance (1 dB in gain, and 20° for the phase), and AWGN associated with an OSNR of 20 dB. The constellation is distorted, but it can be observed that GSOP correctly compensates for the IQ imbalance, as we recover a constellation impaired mainly by the AWGN.

In Figure 2.3, we can observe a 4-QAM constellation impacted by transmitter IQ imbalance (1 dB in gain, and 20° for the phase), and AWGN associated to an OSNR of 20 dB. Different from the receiver IQ imbalance, it can be seen that the constellation still presents some distortion after compensation. The differences observed in figures 2.2 and 2.3 comes from the noise position in the communication chain. In the case illustrated in Figure 2.2, the noise is placed before the receiver IQ imbalance, so the noise undergoes this distortion. That explains the distorted constellation before the compensation. Then,

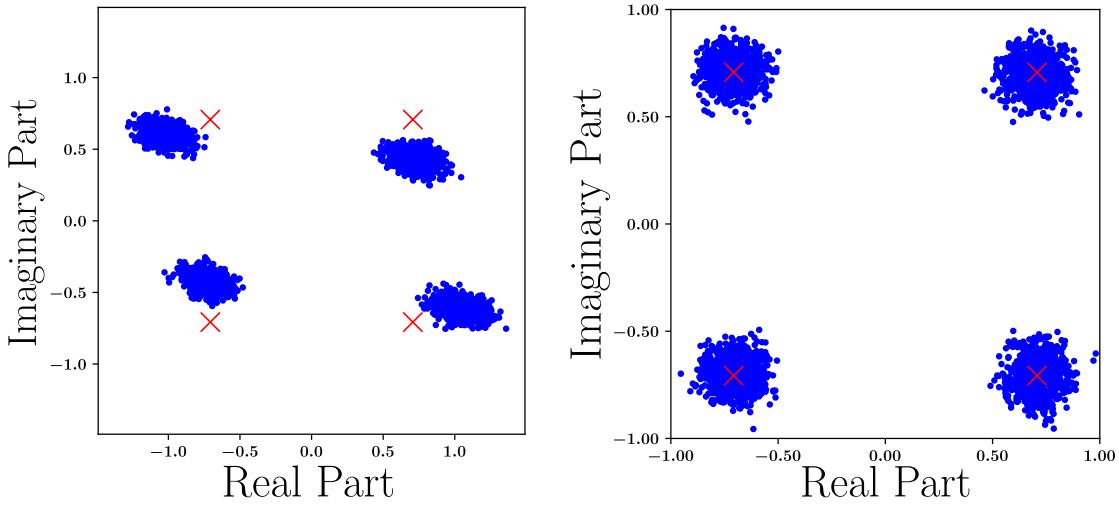

(a) Receiver IQ imbalance impact (b) Receiver IQ imbalance compensation

Figure 2.2 – Receiver IQ imbalance compensation using GSOP

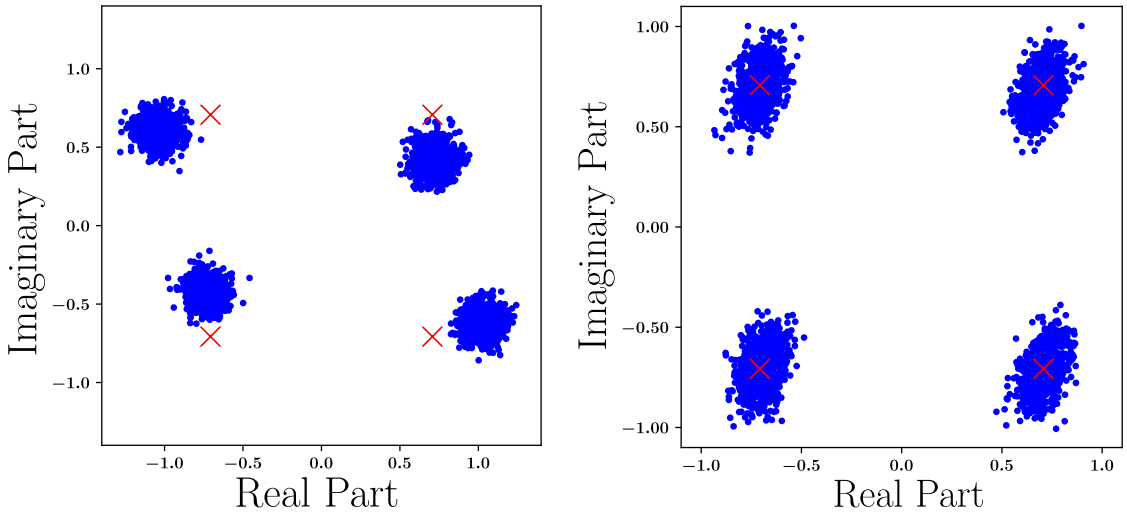

(a) Transmitter IQ imbalance impact (b) Receiver IQ imbalance compensation

Figure 2.3 – Transmitter IQ imbalance compensation using GSOP

GSOP reconstructs the received signal and noise orthogonality. As a consequence, we obtain the constellation that is mainly impaired by AWGN. On the other hand, in Figure 2.3, the noise is placed after the transmitter IQ imbalance, and it is not impacted by this imperfection. In this case, it can be seen that even if GSOP compensates for the IQ imbalance, the noise statistics are modified by it, and the compensated constellation still presents some distortion, which degrades the detection performance. The impact is more critical when higher modulation formats are employed. Based on these, it can be stated

Table 2.3 – Summary of the IQ imbalance compensation techniques

Reference	**Position**	**Polarization**	**Type**
[Fat+08]	Rx	Single	Blind
[Cha+09]	Rx	Single	Blind
[Far+13]	Rx	Dual	Hybrid
[Flu+16]	Tx	Dual	Data-aided
[Sil+16]	Rx	Dual	Hybrid
[Ngu+17]	Tx/Rx	Dual	Blind
[Zha+19a]	Tx/Rx	Single	Blind
[Lag+20]	Tx	Dual	Blind

that the GSOP-based compensation of the receiver side IQ imbalance is more effective, while the transmitter IQ imbalance GSOP-based compensation is less effective and has a higher performance penalty [Chu+10].

Apart from GSOP, multiple other compensation techniques are investigated like the one based on adaptive filters [Far+13; Flu+16; Lia+19; Sil+16], ellipse correction [Cha+09], blind adaptive source separation [Lag+20; Ngu+17], or machine-learning [Zha+19a]. Some of these techniques are designed to compensate for only one type of IQ imbalance (Tx or Rx), while others are effective in the presence of both imperfections (Tx and Rx). Some of these approaches are blind, and others are data-aided or hybrid. Also, some of the mentioned techniques were employed in SP systems, while others have been demonstrated in the DP systems. These informations are summarized in Table 2.3.

2.3 Laser phase noise

Another effect that has a major impact on the coherent optical systems' performance is the laser PN [Col+11]. This effect is due to the broadening of the laser linewidth. The phase noise is conveyed to the modulated signal in coherent communications, and, as a consequence, the received signal is impaired by it [Fic21]. Laser PN is a time-variant effect that can be characterized by the laser linewidth δf, which can vary from less than 100 kHz to a few MHz. This effect is induced by both transmitter and receiver lasers and needs to be compensated for to maintain an acceptable transmission quality.

2.3.1 Signal model

The impact of the laser phase noise on a generic signal can be expressed as [Mag+11; Mor+11]:

$$x_{out}[n] = x_{in}[n]e^{j\phi[n]}, \tag{2.11}$$

where $\phi[n]$ is the laser phase modeled as a Wiener process as follows:

$$\phi[n] = \sum_{k=-\infty}^{n} f[k], \tag{2.12}$$

with f an independent and identically distributed random Gaussian variable with zero mean and variance

$$\sigma_f^2 = 2\pi T_{symb}\delta f. \tag{2.13}$$

The impact on $\mathbf{x}_{out}$ can be seen in Figure 2.4. The rotation introduced by this impairment is proportional to δf and has a time-variant evolution that can lead to the incorrect detection of the data.

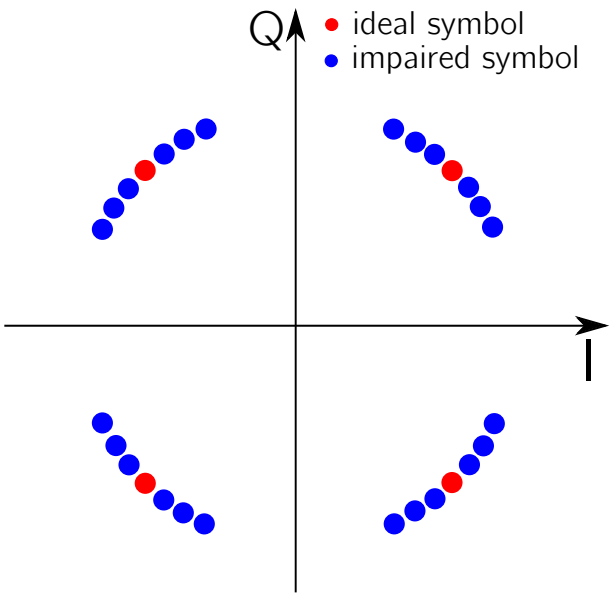

Figure 2.4 – Laser PN impact on an ideal 4-QAM constellation

2.3.2 Compensation

Generally, even if the coherent optical communications are impacted by both transmitter and receiver lasers phase noise, the compensation assumes their impact accumulated on the receiver side.

Starting from the signal model of the laser phase in equation 2.11, the objective is to estimate the parameter $\phi[n]$ corresponding to the $n-th$ symbol of the signal. Then, by using the estimate $\hat{\phi}[n]$, we can invert its impact to recover the desired signal $x_{in}[n]$.

Multiple approaches have been proposed to compensate for the impact of laser phase noise [Tay09]. These compensation algorithms can be classified as blind or data-aided algorithms and are implemented in feedback [Sat+10; Xie+12], or feedforward [Mor+11; Pfa+09] manner, with the feedforward way being preferable for hardware implementation.

The data-aided algorithms are able to track the laser phase in an interval between 0 and 2π, being more robust to cycle slips. Even if the use of additional data for laser phase tracking introduces an overhead, as these data experience the same impairments as the signal, it can be employed for other imperfections compensation. Generally, the data-aided techniques use pilot symbols inserted periodically with a rate of $1/R_P$ (one symbol in R_P is a pilot). The pilots are known on the receiver side.

The implementation of some benchmark pilot-based algorithms used for laser PN compensation is detailed in the following. First, we denote the $k-th$ input and output pilot symbols by $x_{1,in}[k]$ and $x_{1,out}[k]$, respectively. A simple laser phase estimation is performed by multiplying the received pilots with the complex conjugated transmitted pilots as in [Mag+12; Spa+11]:

$$\phi[k] = \arg\left(x_{1,out}[k] \cdot x^*_{1,in}[k]\right). \tag{2.14}$$

This estimation can be significantly improved by using an averaging filter. The impact of noise is reduced because of the averaging as L pilot symbols are used to obtain a single phase estimate as in [Mil+16; Paj+15; Zha+12]:

$$\phi[k] = \arg \sum_{l=k-L/2+1}^{l=k+L/2} \left(x_{1,out}[l] \cdot x^*_{1,in}[l]\right) \tag{2.15}$$

Then, an interpolation filter is applied to the resulting sequence, and the phase estimates are extracted. The concept of estimating the laser phase using pilot symbols and an averaging filter of length L is depicted in Figure 2.5. By using this technique, the estimation

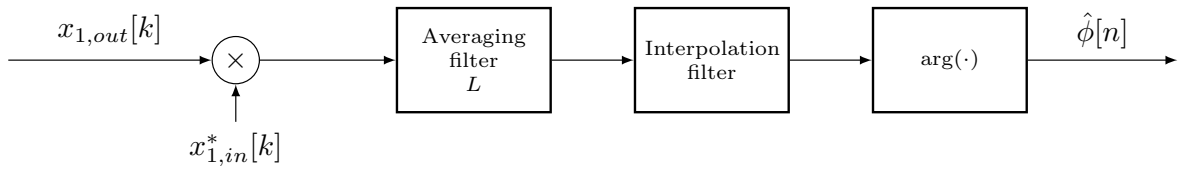

Figure 2.5 – Laser phase estimation using pilot symbols and an averaging filter of length L

of the laser phase is depicted in Figure 2.6 for a 4-QAM communication at an OSNR of 20 dB. Each $30th$ symbol is a pilot and is known on the receiver side. An averaging filter of length $L = 4$ is used, and zero-order interpolation is employed to reconstruct the laser phase. It can be seen that the algorithm is able to track the laser phase evolution even in the presence of noise. Furthermore, in Figure 2.7 the impact and compensation of the laser PN in the same scenario is shown. It can be observed that a rotation of constellation points is introduced by the laser PN. Then, after compensating for this effect, the constellation points are correctly recovered, being only impaired by AWGN.

Apart from the approach mentioned, multiple other techniques are used for laser PN compensation. Among the blind algorithms, for 4-QAM are the ones using the fourth-order statistics [Pev+09; Tay09; Vit+83]. For higher order QAMs, the performance of these algorithms may be degraded, and different techniques using only 4-QAM symbols [Sei08] or 4-QAM partitioning [Fat+10] were employed. Still, these techniques become complicated for modulation orders higher than 16-QAM. Another well-known blind algorithm is the binary phase search algorithm (BPS) [Pfa+09]. This approach has good tolerance, but its computational cost increases with the modulation order. Another conven-

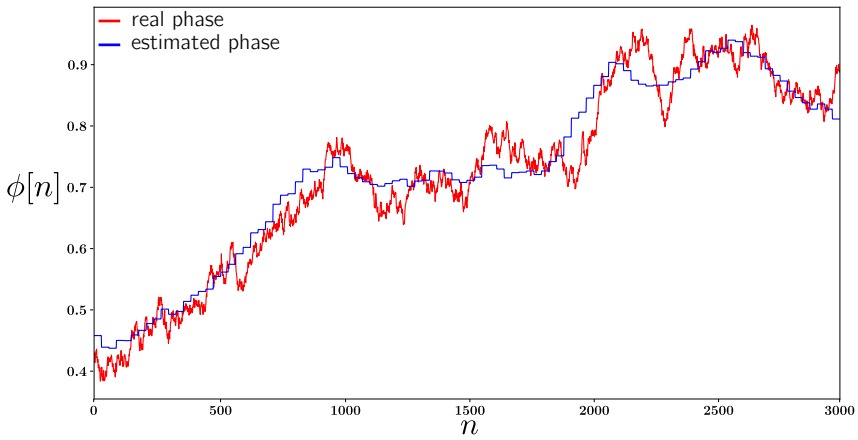

Figure 2.6 – Laser phase estimation

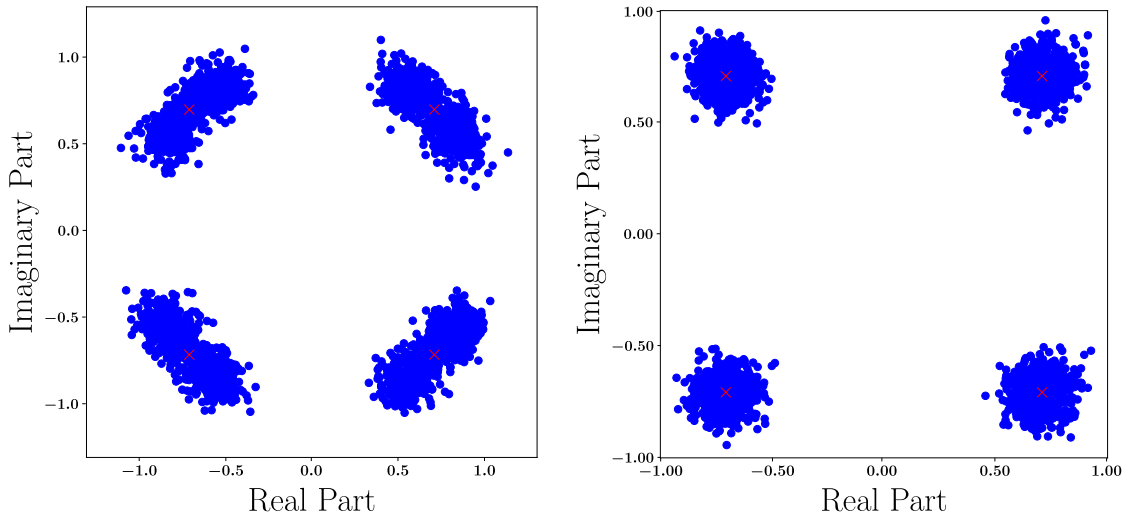

(a) Laser PN impact (b) Laser PN compensation

Figure 2.7 – Laser PN impact and compensation using pilot symbols

tional algorithm is the ML phase estimation [Kam86; Mor+11; Zha+12]. This algorithm could be employed in a decision-aided manner by having knowledge of the constellation.

Recently, multi-stage laser PN compensation is of much interest. This approach consists of a hardware-efficient coarse phase estimation, followed by a finer estimation. The choice of algorithms depends on the compromise between statistical performance and

Table 2.4 – Summary of the laser PN compensation techniques

Reference	**Position**	**Technique**	**Stages**	**Type**
[Xie+12]	Rx	Feedback	Single	Data-aided
[Sat+10]	Rx	Feedback	Single	Blind
[Pev+09]	Rx	Feedforward	Single	Blind
[Vit+83]	Rx	Feedforward	Single	Blind
[Sei08]	Rx	Feedforward	Single	Blind
[Fat+10]	Rx	Feedforward	Single	Blind
[Pfa+09]	Rx	Feedforward	Single	Blind
[Mag+12]	Rx	Feedforward	Two	Hybrid
[Mil+16]	Rx	Feedforward	Two	Hybrid
[Zha+12]	Rx	Feedforward	Two	Hybrid
[Paj+15]	Rx	Feedforward	Two	Hybrid
[Mor+11]	Rx	Feedforward	Two	Hybrid
[Col+11]	Tx/Rx	Feedforward	Single	Hybrid

computational complexity requirements. For example, a coarse estimation using pilots followed by a decision-directed ML estimation could be employed.

A short classification of the laser PN compensation techniques is given in Table 2.4.

2.4 Chromatic dispersion

The group velocity of the propagating signals in the fiber optics is frequency-dependent. This spreads in time the optical pulses leading to ISI and reducing the transmission rate or/and distance. This impairment is known as CD and occurs during the transmission over the optical channel [Elr+88; Sav10; Uda+13]. The CD is a static impairment that severely degrades the communication performance if not compensated for.

2.4.1 Signal model

The CD can be modeled as an all-pass filter having the frequency transfer function expressed as [Kus+09a; Xu+10]:

$$H_{CD}(\omega, Dz) = e^{-j\frac{Dz\lambda^2}{4\pi c}\omega^2}, \tag{2.16}$$

where Dz is the accumulated CD, with D denoting the dispersion coefficient and z the fiber length, λ the wavelength, c the speed of light, and ω the angular frequency depending on the sampling frequency f_s. The current SMFs used in coherent optical communications are generally described by a dispersion coefficient of approximately $D \simeq 17$ ps/nm-km.

The impact of the CD on the transmitted signal can be modeled as:

$$x_{out}[n] = \mathcal{F}^{-1}\left(H_{CD}(\omega, Dz)\mathcal{F}\left(x_{in}[n]\right)\right), \tag{2.17}$$

where $\mathcal{F}$ and $\mathcal{F}^{-1}$ represent the discrete Fourier transform and the inverse discrete Fourier transform operations, respectively.

The impact of CD on a transmitted pulse can be seen in Figure 2.8, where the transmitted pulse is broadened in time, leading to neighbor symbols overlapping.

2.4.2 Compensation

Originally, the CD was compensated for in the optical domain using DCFs or Dispersion Compensating Modules (DCMs) [Agr12]. Even if this approach proved effective,

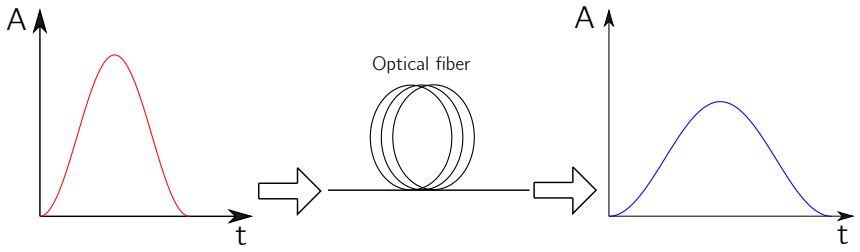

Figure 2.8 – Impact of CD on a transmitted pulse

it is difficult to adapt to different fiber properties and quality measures. Moreover, it introduces an undesirable latency [Dav+11].

With the advance in electronic devices manufacturing, the DSP compensation of CD is increasingly employed. A well-known approach for compensating the CD is to use an all-pass filter with the following transfer function [Far+17; Ip+07; Sav08]:

$$H_f(\omega) = \frac{1}{H_{CD}(\omega, Dz)} = e^{j\frac{Dz\lambda^2}{4\pi c}\omega^2}. \tag{2.18}$$

In Figure 2.9, the impact and compensation of an 17000 ps/nm accumulated CD on 4-QAM constellation at an OSNR of 20 dB is depicted. The severe impact of CD on the symbol constellation can be seen. Because of the ISI, the transmitted data cannot be recovered without proper compensation. In the specific scenario where the parameters

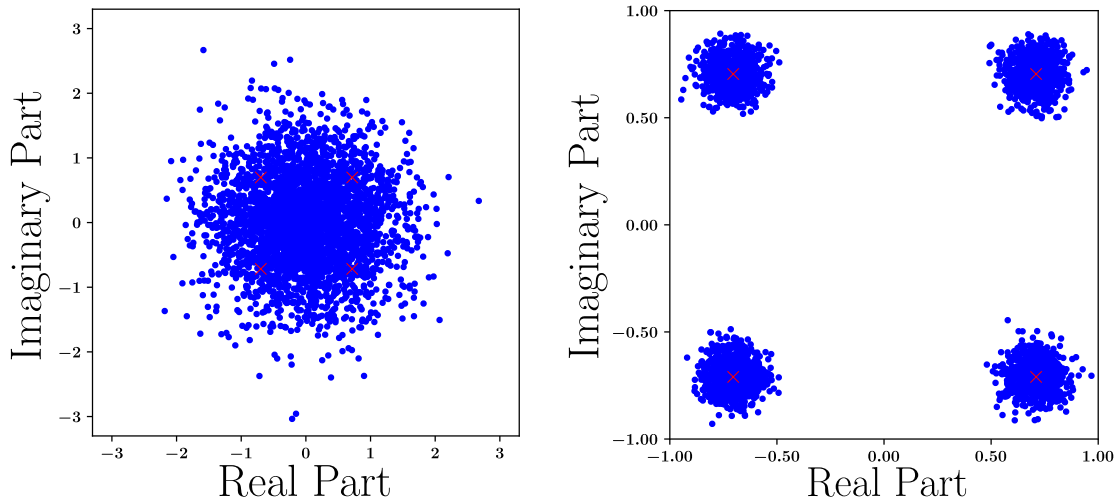

(a) CD impact (b) CD compensation

Figure 2.9 – CD impact and compensation using an ideal compensating filter in the frequency domain

describing the transfer function of the compensation filter (dispersion coefficient, fiber length, etc.) are well known, the dispersion can be perfectly compensated, as shown in the second column of Figure 2.9.

Although, in theory, the impact of CD can be easily compensated for, the design of such a filter is not trivial. Consequently, the compensation filter is approximated in the time or frequency domain and is implemented using Finite Impulse Response (FIR) or Infinite Impulse Response (IIR) filters. The filters can be static or adaptive. In addition, based on prior knowledge regarding the system's parameters, the CD compensation can be performed on the receiver or/and transmitter sides [Bul+08]. The compensation on the receiver side is known as post-compensation, while the one on the transmitter side is pre-compensation.

2.4.2.1 Time-domain equalizer

The impulse response of the filter can be expressed by applying the inverse Fourier transform of $H_f(\omega, Dz)$ as follows:

$$h(t, Dz) = \sqrt{\frac{c}{jDz\lambda^2}} e^{j\frac{\pi c}{Dz\lambda^2}t^2}. \tag{2.19}$$

This non-causal impulse response, infinite in duration, introduces aliasing since it passes all the frequencies at a finite sampling frequency. To solve these problems, in [Sav08], the filter response was truncated to a finite duration and implemented using a static FIR filter. Another approach was employed in [Egh+14] using a static FIR filter also. In this case, optimal tap weights of the filter were obtained using the Least-Squares (LS) criterion. The compensation was constrained to a particular bandwidth, relaxing the constraints outside of it. Another time-domain compensation technique was presented in [Xu+10], which uses an adaptive Least Mean Square (LMS) filter, and a static FIR filter. These two filters could also be coupled in a practical system to compensate for multiple impairments. The CD compensation can also be implemented using an IIR filter as in [Gol+07]. This technique reduces the number of taps compared to FIR filters, but it is difficult to implement it in a parallel structure, which is a key requirement for real-time processing [Pfa16].

Table 2.5 – Summary of CD compensation techniques

Reference	**Position**	**Domain**	**Type**
[Sav08]	Rx	Time	Blind
[Egh+14]	Rx	Time	Blind
[Xu+10]	Rx	Time & Frequency	Blind
[Gol+07]	Rx	Time	Blind
[Gey+10]	Rx	Frequency	Blind
[Kud+09]	Rx	Frequency	Blind
[Xu+11]	Rx	Frequency	Blind
[Kus+09a]	Rx	Time & Frequency	Blind
[Ip+07]	Rx	Frequency	Blind

2.4.2.2 Frequency-domain equalizer

Generally, the number of filter taps N_f required to compensate for CD is large, and by this, the computational complexity $\mathcal{O}(N_f)$ of time-domain compensation may become problematic. On the other hand, the filtering in the frequency domain is more efficient with a complexity of $\mathcal{O}(\log(N_f))$ [Shy+92].

The frequency compensation of CD is typically implemented using overlap-save [Gey+10; Kud+09; Xu+10] or overlap-add methods [Xu+11]. In [Kus+09a] an adaptive filtering technique is introduced. This technique has low complexity and can estimate arbitrarily large values of CD. In [Ip+07], the CD is jointly compensated for with PMD using a Fractionally Spaced Equalizer (FSE). This approach can compensate for any arbitrary amount of CD, and first-order PMD provided an oversampling rate of a minimum of 3/2 and a sufficient number of taps.

The discussed approaches used for CD compensation are summarized in Table 2.5.

2.5 Polarization mode dispersion

As the transmission rate increases, PMD is one of the most important impairments that impact coherent optical communications. In SMFs, two orthogonal polarization modes could be transmitted over the optical channel. In ideal conditions, these two modes should exhibit the same group delay. However, the manufacturing imperfections of fiber and/or the environmental changes introduce a birefringence. PMD arises from this birefringence and the random variation of the Principal State of Polarizations (PSPs) along the fiber

link. It is a time-variant impairment that distorts the signal pulses and degrades the system performance if not compensated for [Kam+02].

2.5.1 Signal model

The PMD is generally modeled using the following frequency transfer function [Ip+07]:

$$\boldsymbol{H}_{PMD}(\omega,\theta,\tau) = \begin{bmatrix} \cos(\theta) & -\sin(\theta) \\ \sin(\theta) & \cos(\theta) \end{bmatrix} \begin{bmatrix} e^{j\omega\tau/2} & 0 \\ 0 & e^{-j\omega\tau/2} \end{bmatrix} \begin{bmatrix} \cos(\theta) & \sin(\theta) \\ -\sin(\theta) & \cos(\theta) \end{bmatrix}, \tag{2.20}$$

where θ denotes the random polarization angle, and τ is the Differential Group Delay (DGD) between the PSPs. The impact of the PMD on the input signals can be expressed as follows:

$$\begin{bmatrix} x_{X,out}[n] \\ x_{Y,out}[n] \end{bmatrix} = \mathcal{F}^{-1}\left(\boldsymbol{H}_{PMD}(\omega,\theta,\tau)\mathcal{F}\left(\begin{bmatrix} x_{X,in}[n] \\ x_{Y,in}[n] \end{bmatrix}\right)\right), \tag{2.21}$$

where $\{X, Y\}$ denote the two polarizations.

In Figure 2.10, the illustration of the time-domain impact of PMD in a fiber can be observed. It can be seen that the launched pulse has an ideal distribution between the two polarization axes. Then, after the transmission on fiber, the pulse is broadened by the DGD. The PMD impact is generally expressed by the PMD coefficient. The coefficient is obtained by multiplying the mean DGD with the square root of the fiber length ($\overline{\tau} \cdot \sqrt{z}$), and is expressed in $\left[\text{ps}/\sqrt{\text{km}}\right]$. Modern fibers have typical coefficients such that PMD $< 0.1\text{ps}/\sqrt{\text{km}}$ [Agr12].

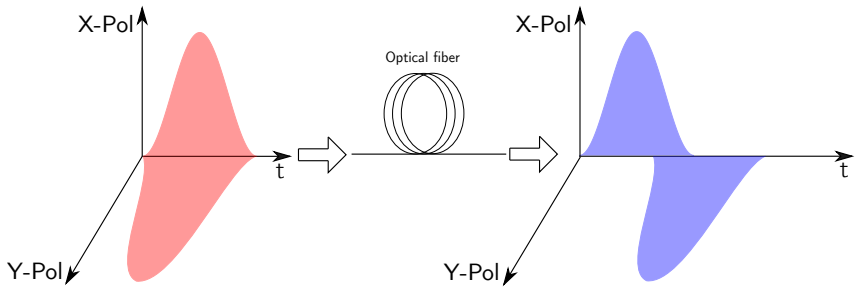

Figure 2.10 – Impact of PMD on a transmitted signal

2.5.2 Compensation

Formerly, the PMD was compensated for in the optical domain, mostly for the system not employing PDM [Buc+04; Hil+92]. However, this approach lacks flexibility and has an increased cost and complexity. As a consequence, the PMD compensation is mostly operated in the digital domain nowadays.

The impact of PMD is modeled by a frequency-dependent Jones matrix. Differently from the case of the CD, the Jones matrix describing the PMD is time-variant. Thus, an adaptive equalization should be employed to track the matrix variation and invert its impact. The equalizer required to compensate for PMD may be implemented using 4 FIR filters, in a 2×2 Multiple-Input Multiple-Output (MIMO)-based setup as in Figure 2.11 [Far+17; Sav08; Sav10]. The compensated signal at the output of the MIMO equalizer can be expressed as follows:

$$\hat{x}_{X,in}[n] = \sum_{m=0}^{M-1} h_{XX}[m]x_{X,out}[n-m] + h_{XY}[m]x_{Y,out}[n-m], \tag{2.22}$$

$$\hat{x}_{Y,in}[n] = \sum_{m=0}^{M-1} h_{YX}[m]x_{X,out}[n-m] + h_{YY}[m]x_{Y,out}[n-m], \tag{2.23}$$

where $\mathbf{h}_{XX}$, $\mathbf{h}_{XY}$, $\mathbf{h}_{YX}$, $\mathbf{h}_{YY}$ are the impulse responses of the adaptive filters of M taps length, and $(.)^H$ denotes the transpose of the complex conjugate operation, also known as the Hermitian transpose.

Generally, the adaptation algorithms are based on a cost function minimization using variants of gradient descent (stochastic gradient descent) [Rud16]. One of the most

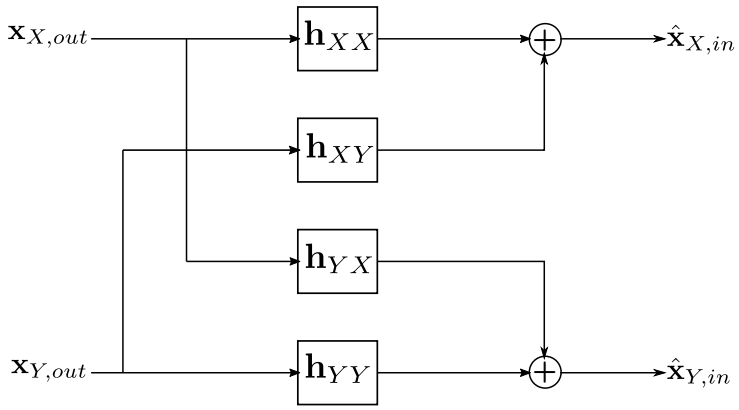

Figure 2.11 – MIMO equalizer composed of FIR filters

employed cost functions is the one that minimizes the following errors:

$$\epsilon_X[n] = R_2 - |\hat{x}_{X,in}[n]|^2, \tag{2.24}$$

$$\epsilon_Y[n] = R_2 - |\hat{x}_{Y,in}[n]|^2, \tag{2.25}$$

where:

$$R_2 = \frac{E|x_{ideal}|^4}{E|x_{ideal}|^2} \tag{2.26}$$

represents the real-valued constant depending on the distribution of ideal symbol x_{ideal}. Specifically, the update equations are given by:

$$h_{XX}[n+1] = h_{XX}[n] + \lambda_s \epsilon_X[n] \hat{x}^*_{X,in}[n] x_{X,out}[n] \tag{2.27}$$

$$h_{XY}[n+1] = h_{XY}[n] + \lambda_s \epsilon_X[n] \hat{x}^*_{X,in}[n] x_{X,out}[n] \tag{2.28}$$

$$h_{YX}[n+1] = h_{YX}[n] + \lambda_s \epsilon_Y[n] \hat{x}^*_{Y,in}[n] x_{Y,out}[n] \tag{2.29}$$

$$h_{YY}[n+1] = h_{YY}[n] + \lambda_s \epsilon_Y[n] \hat{x}^*_{Y,in}[n] x_{Y,out}[n], \tag{2.30}$$

where the λ_s denotes the step size parameter. The filter taps are initialized with 0s, except for the central tap of h_{XX} and h_{YY}, which are initialized with 1s. This technique is known as Constant-Modulus Algorithm (CMA) [God80; Joh+98]. It is usually employed for 4-QAM communication, as in the case of this modulation, ideal symbols have equal amplitude [Sav+07]. However, at large values of DGD, the algorithm may converge to the same output. To alleviate this problem, different techniques were investigated [Far+10; Kik11; Liu+09].

In Figure 2.12, the impact and compensation of PMD can be seen on 4-QAM constellation at an OSNR of 20 dB. The transmitted signal was twofold oversampled in order to obtain a reasonable compensation efficiency [Kus+09b] and filtered with an RRC filter. Then, the signal was matched filtered on the receiver side by another RRC filter. After the matched filtering, the compensation was performed using the MIMO equalizer with filters of 8 taps length and CMA as an adaptation algorithm. In this context, the filters' update was performed for every two samples. Then, the downsampling was implemented. The PMD corresponds to a DGD τ of 30 ps and a rotation θ of $\frac{\pi}{4}$. It can be seen that before compensation, the constellation is highly impacted by PMD. After the compensation, the transmitted data can be correctly recovered.

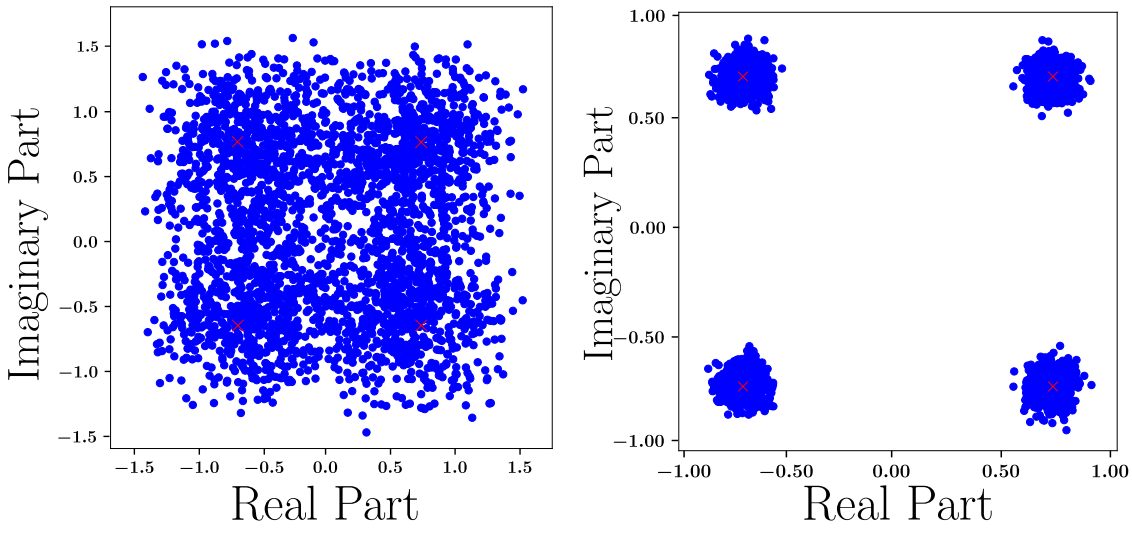

(a) PMD impact (b) PMD compensation

Figure 2.12 – PMD impact and compensation using a MIMO equalizer with CMA

CMA has been designed for constant modulus modulations, but most of the modulations employed for high-speed coherent optical communications are not constant-modulus (e.g 16-QAM, 256-QAM, etc.). Nevertheless, the CMA can be adapted for higher-order modulations using a radially directed equalizer that considers the radius of all possible constellation rings [Lav+15; Rea+90].

Another classical algorithm used for filter adaption is Decision-Directed Least-Mean-Square (DD-LMS) [Qur85]. In this case, the knowledge of modulation formats is exploited. The received signal is detected, and a feedback loop is used to adapt the filter weights. For a better understanding, in Figure 2.13, the blocks used for update in the case of CMA and DD-LMS are depicted. This approach is generally employed after a training symbols-based technique, or a CMA-based algorithm because using it before can lead to poor results as the most detected symbols may be wrong initially. Another possible solution is to use training symbols, and the LMS algorithm as in [Han+05]. Recursive LS is another technique that can be used for filter adaption. This technique benefits from a faster convergence but has a higher computational cost [Hay08].

In [Far+13; Ngu+15], the PMD and IQ imbalance compensation is operated using digital filters, while in [Lag+20] using Blind Adaptive Source Separation (BASS) with a global updating of the Equivariant Adaptive Separation via Independence (EASI). In [Ip+07], the PMD and CD are mitigated using a FSE. In [Büt+20; Häg+20b], the fiber nonlinearity and PMD are compensated for using model-based ML. The summary of

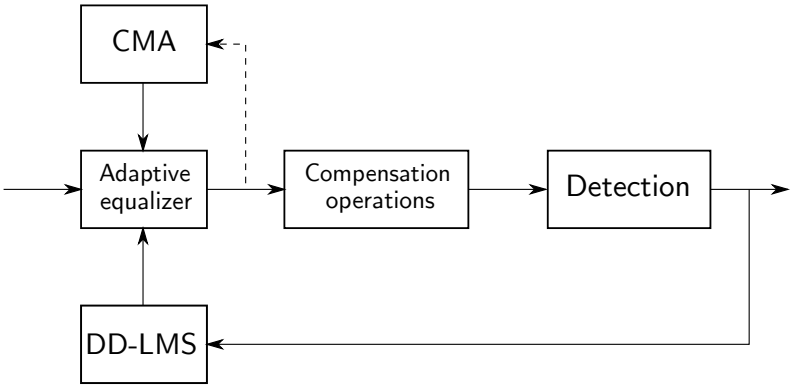

Figure 2.13 – The blocks used for update in the case of CMA and DD-LMS

Table 2.6 – Summary of PMD compensation techniques

Reference	**Method**	**Scenario**	**Type**
[Sav+07]	CMA	Compensation	Blind
[Lav+15]	CMA-based	Compensation	Blind
[Han+05]	LMS	Demultiplexing	Data-aided
[Far+13]	DD-LMS	Compensation	Hybrid
[Ngu+15]	DD-LMS	Demultiplexing	Blind
[Lag+20]	EASI	Demultiplexing	Blind
[Ip+07]	FSE	Compensation	Blind
[Büt+20]	ML	Compensation	Data-aided
[Häg+20b]	ML	Compensation	Data-aided

PMD mitigation approaches can be found in Table 2.6. Depending on the scenario, two different terms were used. If the DGD is neglected or has very little influence on overall performance, the term “Demultiplexing” is used, while the term “Compensation” is used when DGD is also present.

2.6 Carrier frequency offset

In coherent optical communications, the two lasers (transmitter and receiver) should be operated at the same frequency. However, during the lifetime of a tunable laser, a CFO of ± 2.5 GHz may be experienced [For15]. The frequency mismatch between the two lasers can be corrected based on a feedback loop. Otherwise, the two lasers may be free-running, and the CFO between them must be compensated for by using DSP algorithms.

2.6.1 Signal model

The impact of CFO on a transmitted signal can be expressed as follows [Mei+13]:

$$x_{out}[n] = x_{in}[n]e^{j2\pi n\frac{\Delta F}{f_s}}, \tag{2.31}$$

where ΔF is the frequency offset between the two lasers.

Relatively similar to the impact of laser PN, the CFO introduces a rotation of the constellation points, as can be seen in Figure 2.14. The rotation of constellation points is proportional to the value of ΔF and can be clockwise or counterclockwise, depending on the sign of the parameter. As it can be seen, the transmitted symbols cannot be correctly detected on the receiver side if no compensation is performed to mitigate CFO.

2.6.2 Compensation

The objective of the compensation is to invert the impact of ΔF in order to recover the transmitted data. In literature, multiple techniques have been proposed for CFO compensation [Far+17].

The data-aided techniques used for CFO compensation can mitigate a wide range of frequency offsets and are modulation-format independent at the expense of an overhead [Zho+11]. The training symbols may consist of a preamble block or multiple pilot symbols

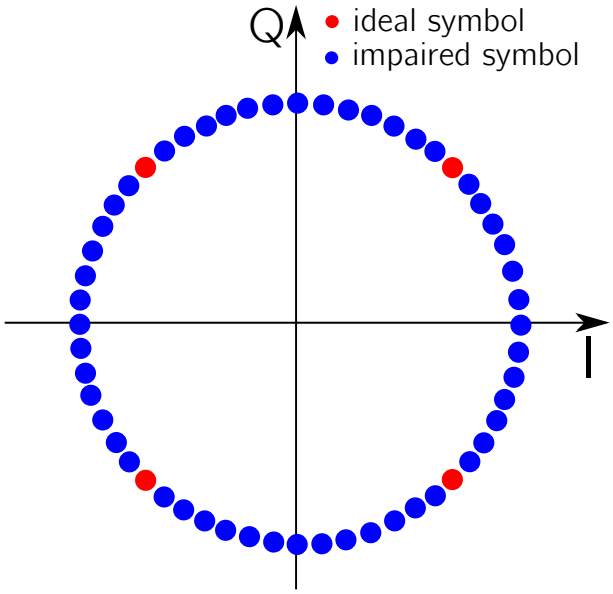

Figure 2.14 – CFO impact on a 4-QAM constellation

inserted periodically into the data frame. In the following, an efficient CFO compensation technique is presented. First, the modulation phase is removed by multiplying the complex conjugated transmitted preamble with the received preamble as in [Zho+11]:

$$\phi[n] = \arg\left(x_{0,out}[n] \cdot x^*_{0,in}[n]\right), \tag{2.32}$$

where $x_{0,out}$ and $x_{0,in}$ are the received and transmitted preamble symbols. Then, the CFO is estimated by performing a LS linear fit on the phase evolution vector, and its impact is inverted. In Figure 2.15, the impact and compensation of CFO using the presented approach is depicted for 4-QAM constellation. The simulated CFO has a value of 200 MHz for a signal bandwidth of 20 GHz and a sampling frequency f_s of 20 GHz, too. The OSNR value is 20 dB. Three thousand symbols were employed, and from these, 300 were used as a preamble. The high impact of CFO can be seen in the first figure, where a correct detection of symbols cannot be performed. On the other hand, after the compensation, the symbols are only impacted by the noise, and the detection can be correctly done. The CFO can also be compensated for using pilots as training data. In [Zha+15], the CFO is estimated by using the pilots location in the spectrum.

Apart from data-aided compensation techniques, several well-known blind methods may be used for CFO mitigation. One of the benchmark algorithms is the one based on $4th$ order statistics [Fat+11; Hof+08; Lev+07]. Despite their efficiency for 4-QAM, these algorithms' performance is limited in the case of higher-order modulations. However,

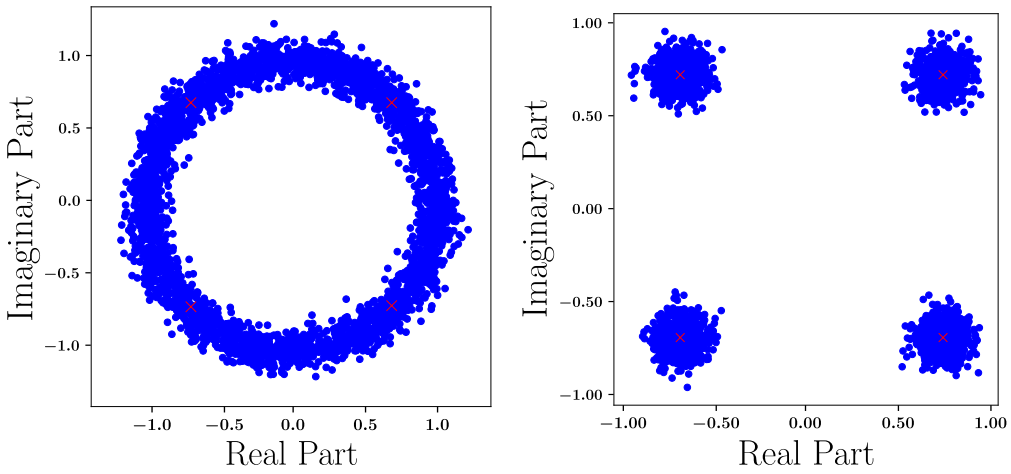

(a) CFO impact (b) CFO compensation

Figure 2.15 – CFO impact and compensation using a preamble data block

Table 2.7 – Summary of the CFO compensation techniques

Reference	**Technique**	**Domain**	**Type**
[Zho+11]	Feedforward	Time	Data-aided
[Lev+07]	Feedforward	Time	Blind
[Hof+08]	Feedforward	Time	Blind
[Zha+15]	Feedforward	Frequency	Blind
[Nak+10]	Feedforward	Frequency	Blind
[Nak+11]	Feedforward	Frequency	Blind
[Sel+09]	Feedforward	Frequency	Blind
[Wan+01]	Feedforward	Frequency	Blind
[Fat+11]	Feedforward	Time	Blind
[Mei+13]	Feedback	Time	Decision-Aided
[Mor+13]	Feedback	Time	Decision-Aided
[Xie+12]	Feedback	Time	Blind

by performing some statistical processings, the extension to higher order QAM modulation is possible [Sel+09; Wan+01]. Alternatively, spectrum-based compensation methods are used for CFO compensation [Nak+10; Nak+11]. Generally, these techniques perform better than those based on $4th$ power operation, but their complexity increases for higher-order modulations. Apart from these feedforward techniques, feedback compensation techniques were also highly investigated [Mei+13; Mor+13; Xie+12]. The feedback techniques are independent of the modulation format, but they may be problematic because of the feedback delay. A summary of the CFO compensation techniques can be found in Table 2.7.

2.7 Coherent optical transmission under the impact of multiple imperfections

The previous sections investigated the impact of certain linear imperfections in coherent optical communications. Nevertheless, the transmitted data is usually impaired by multiple linear imperfections simultaneously. The following details the signal model of such a system and a common compensation approach.

2.7.1 Objective

A coherent optical communication system impaired by multiple linear imperfections can be generically described by the following equation:

$$\tilde{\mathbf{y}} = \mathbf{M}(\boldsymbol{\alpha})\tilde{\mathbf{x}} + \tilde{\mathbf{b}}, \tag{2.33}$$

where the tilde denotes the augmented real-valued data corresponding to the original complex vectors [1], the ideal transmitted signal is denoted by $\mathbf{x}$, the impaired received signal by $\mathbf{y}$, $\mathbf{M}(\boldsymbol{\alpha})$ is a real-valued transfer matrix of the whole system depending on the unknown vector parameter $\boldsymbol{\alpha}$ corresponding to the impairments, and $\mathbf{b}$ describes the noise contribution. On the receiver side, the objective is to detect the transmitted data from the received one and to minimize the BER.

2.7.1.1 General approach

Using as a basis (2.33) and assuming Gaussian noise and independent and identically distributed symbols, the detection problem can be obtained by minimizing the LS cost function as follows:

$$\{\hat{\boldsymbol{\alpha}}, \mathbf{x}_{det}\} = \arg \min_{\boldsymbol{\alpha}, \mathbf{x} \in \mathbb{S}^N} \|\tilde{\mathbf{y}} - \mathbf{M}(\boldsymbol{\alpha})\tilde{\mathbf{x}}\|_2^2. \tag{2.34}$$

This minimization problem can be difficult to address in its original form. To simplify this problem, the detection can be divided into two main steps as follows:

— Estimation of system parameters $\hat{\boldsymbol{\alpha}}$ using a data-aided technique;

— MIMO detection of transmitted data:

$$\mathbf{x}_{det} = \arg \min_{\mathbf{x} \in \mathbb{S}^N} \|\tilde{\mathbf{y}} - \mathbf{M}(\hat{\boldsymbol{\alpha}})\tilde{\mathbf{x}}\|_2^2. \tag{2.35}$$

The MIMO detection can be performed by using the Maximum-Likelihood Detector (MLD) [Zhu+02] that achieves optimal performance. However, its complexity is NP-hard. To reduce the computational complexity, suboptimal linear detectors such as the Minimum Mean Squared Error (MMSE) and Zero-Forcing (ZF) detectors are often used [Tri+12]. MMSE has a better accuracy than ZF, especially at low-medium values of OSNR, while ZF requires less computational effort. For simplicity reasons, this thesis

1. For example: $\tilde{\mathbf{x}} = \begin{bmatrix} \Re e\{\mathbf{x}\}^T & \Im m\{\mathbf{x}\}^T \end{bmatrix}^T$

focuses on the ZF detector. The ZF detection consists of the following operations:

— Compensation of imperfections:

$$\hat{\tilde{\mathbf{x}}} = \mathbf{M}^{-1}(\hat{\boldsymbol{\alpha}})\tilde{\mathbf{y}}; \tag{2.36}$$

— Hard detection of symbols:

$$x_{det}[n] = \arg\min_{s\in\mathbb{S}} \|\hat{x}[n] - s\|_2^2, \tag{2.37}$$

where $x_{det}[n]$ denotes the detected symbol.

2.7.1.2 Cascaded local compensation

In literature, a commonly used technique to implement (2.36) is to cascade multiple individual DSP algorithms that compensate for the imperfections without explicitly estimating $\boldsymbol{\alpha}$, then a hard projection is operated. Each of the algorithms compensates for a particular imperfection, and by cascading them, the aim is to mitigate all imperfections' impact. Starting from now, this approach will be denoted *local* compensation. Using a local compensation approach, a strategy to cascade the DSP algorithms should be developed to achieve good performances, as there are many possible options. Imperfections may be compensated for both on the transmitter and receiver sides, or the compensation may be split between the transmitter and receiver. In coherent optical systems, the compensation of most imperfections is typically performed on the receiver side because the transmitter side compensation requires a feedback channel for most of the imperfections, which is not typical in optical systems, as it introduces a delay. Even in the case of receiver-side compensation, there are many possible strategies that may be used. A common approach is to apply the compensation scheme from Figure 2.16 [Far+17]. The functionality of the DSP blocks can be summarized as follows:

— the amplitude and phase mismatch between the I and Q components of the signal is compensated for;

— the CD impact is compensated for using a static filter;

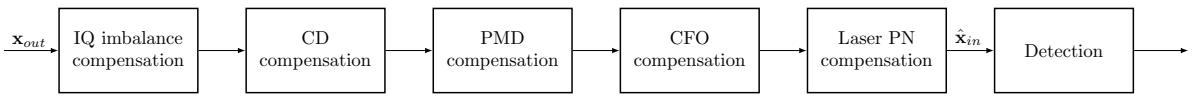

Figure 2.16 – DSP sequence of compensation operations in a coherent optical receiver

— the PMD impact is compensated for using an adaptive filter;
— the CFO between the two lasers is corrected;
— the laser PN is mitigated;
— the transmitted symbols are detected;

It is essential to notice that, depending on the scenario, more adapted compensation schemes may exist.

2.7.2 Simulation results

In this subsection, the effectiveness of the local compensation approach is investigated using simulations in two simplified scenarios. An SP coherent optical communication with multiple impairments is considered. The communication link is assumed to be dispersion compensated. As a consequence, the impairments that impact the considered communication chain are IQ imbalance, CFO, and laser PN. Moreover, the impact of laser PN is accumulated on the receiver side.

To be able to compensate for these imperfections, a classical hybrid strategy regarding data allocation is considered. This strategy consists of using a preamble and multiple pilots that are known on the receiver side. The preamble data is used for the mitigation of static imperfections, while the pilot symbols are employed in the tracking of time-variant imperfections. The frame structure is depicted in Figure 2.17. It can be observed that it contains a preamble of N_0 symbols and multiple data blocks with N_b symbols. Each data block contains P pilots inserted periodically. The preamble and each block contain 300 symbols ($N_0 = N_b = 300$).

The system and imperfections parameters are detailed in Table 2.8.

Two scenarios detailed in the following are considered to investigate the effectiveness of the local compensation approach.

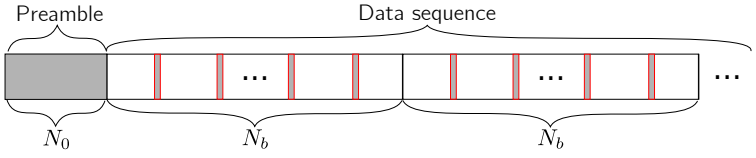

Figure 2.17 – The frame structure consisting of a preamble and multiple data blocks containing pilots inserted periodically

Table 2.8 – System and imperfections parameters

BW [GHz]	**f_s [GHz]**	**g [dB]**	**ϑ [deg.]**	**ΔF [MHz]**	**δf [kHz]**
20	20	1	10	200	100

2.7.2.1 Multiple impairments without transmitter IQ imbalance

First, it can be seen that in Figure 2.18 that the transmitted signal is impaired by AWGN on the channel, and by CFO, IQ imbalance, and laser PN on the receiver side. For multiple impairment compensation, the following scheme is used:

— First, the IQ imbalance is compensated in a blind manner using GSOP [Fat+08];

— Secondly, using the preamble data, the CFO is estimated and compensated for. The modulation phase is removed by multiplying the complex conjugated transmitted preamble with the received preamble as in [Zho+11], then the CFO is estimated using a LS linear fit;

— Finally, the impact of laser PN is mitigated using the pilot symbols. First, a correlation between the transmitted and received pilots is performed [Mag+12]. An averaging filter of length 4 is applied to reduce the AWGN [Zha+12]. After that, a second estimation stage is operated by using maximum likelihood phase estimation in a decision-directed manner [Mor+11]. Finally, the averaging filter is applied once again.

In Figure 2.19, the simulation results obtained by using the considered compensation scheme and a single realization of a 16-QAM transmission at OSNR value of 20 dB can be seen. The BER simulated performance for a channel impacted only by Gaussian noise is denoted as "AWGN Ch." and is used as a performance bound, while the BER performance of the employed compensation scheme is denoted as "DSP v1". The simulations were performed for 4-QAM and 16-QAM cases. It can be seen in Figure 2.19a that the compensation approach employed is effective as its performance is relatively close to the one over an AWGN channel. After the OSNR values of 9 dB and 16.2 dB, the perfor-

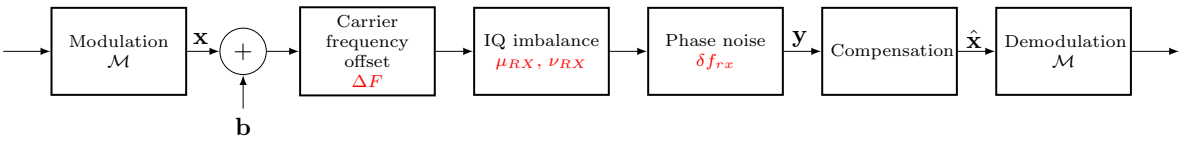

Figure 2.18 – Communication system impaired by CFO, receiver IQ imbalance, and laser PN

mance of the DSP compensation technique is below the imposed threshold (see 1.2.3.3) for 4-QAM, and 16-QAM, respectively. Based on that, it can be stated that the discussed compensation scheme introduces penalties of 0.6 dB for 4-QAM and 1.2 dB for 16-QAM compared to the performance bounds imposed. In Figure 2.19b, the signal constellation before any compensation can be observed. The constellation consists of multiple ellipses, as CFO and laser PN rotate the constellation, while IQ imbalance make the constellation non-orthogonal. After the GSOP, the constellation has the form of multiple concentric circles, as its orthogonality is recovered. Then, after CFO compensation, the constellation is only impacted by laser PN and noise. Finally, in the last figure, the transmitted data can be correctly detected, being impacted only by the noise.

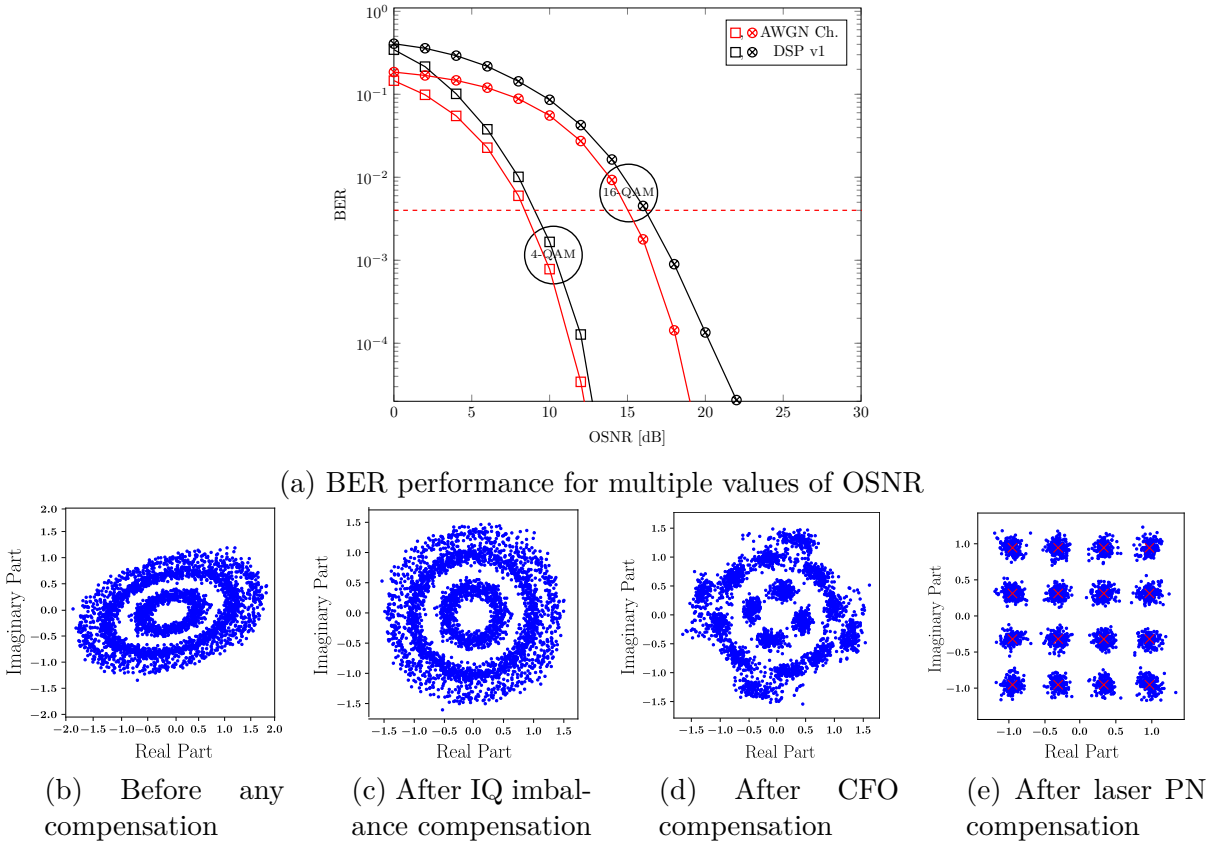

(a) BER performance for multiple values of OSNR

(b) Before any compensation

(c) After IQ imbalance compensation

(d) After CFO compensation

(e) After laser PN compensation

Figure 2.19 – Performance of the first compensation scheme in the presence of IQ imbalance on the receiver side

2.7.2.2 Multiple impairments with transmitter IQ imbalance

In the second scenario, an IQ imbalance is also present on the transmitter side, as shown in Figure 2.20. For compensation, the same compensation scheme is considered. The results obtained for this case can be found in Figure 2.21. It can be observed that the DSP compensation technique gives poor results, especially for 16-QAM case, where the performance does not reach the imposed QoS. Concerning the constellations for a single realization, it can be seen that the impact of the transmitter IQ imbalance is not correctly compensated for. Moreover, the performance of the laser PN compensation algorithm is impaired by the presence of IQ imbalance.

For performance improvement, another DSP approach is now considered to mitigate transmitter IQ imbalance. In [Flu+16], the transmitter IQ imbalance is compensated for using FIR filters with a single tap in a MIMO configuration. The paper's authors place the filters after the carrier phase estimation and suggest performing another phase estimation after it to achieve better results. In Figure 2.22a, the results obtained for this compensation technique ("DSP v2") are depicted. It can be seen that there is an improvement compared to the first compensation scheme ("DSP v1"), but the results are still far from the performance bounds, and the "flooring" effect for 16-QAM still persists. On the constellations, it can be observed that the transmitter IQ imbalance is compensated for, but the laser PN compensation method is highly impacted by its presence. This reduced the final performance of the "DSP v2" technique.

Finally, to improve the method's performance, another compensation scheme, denoted "DSP v3" is proposed. Unlike the "DSP v2", before the transmitter IQ imbalance compensation, only a constant constellation rotation is applied using the pilot symbols. The rest of the compensation scheme remains unchanged. In Figure 2.23 it can be seen that this compensation approach achieves better performance for both 4-QAM and 16-QAM. Moreover, the performance of 16-QAM is better than the imposed threshold above 20 dB OSNR. Seeing the constellations for a single realization, it can be seen that the constant rotation introduced manages to perform a coarse laser PN compensation, sufficient enough

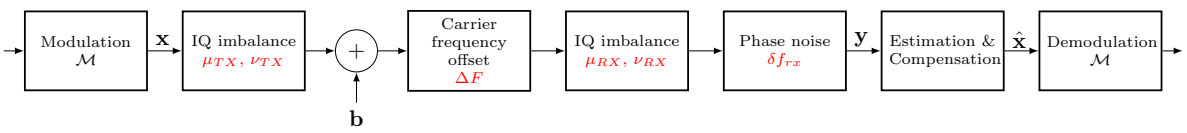

Figure 2.20 – Communication system impaired by transmitter IQ imbalance, CFO, receiver IQ imbalance, and laser PN

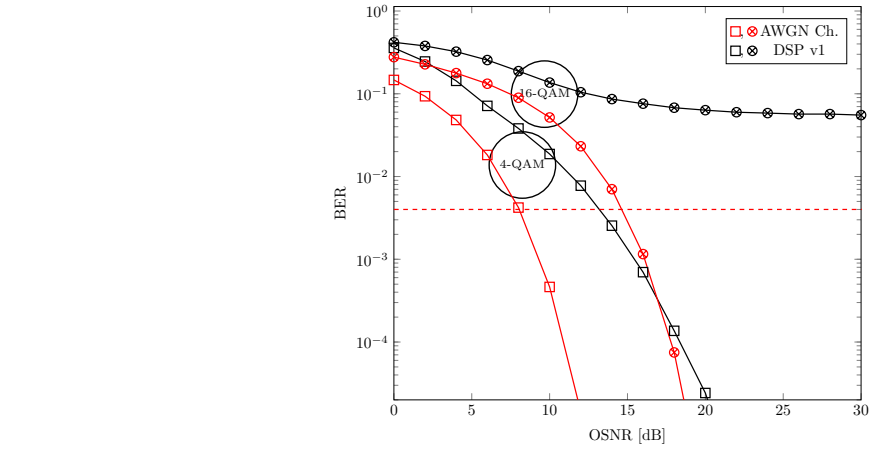

(a) BER performance for multiple values of OSNR

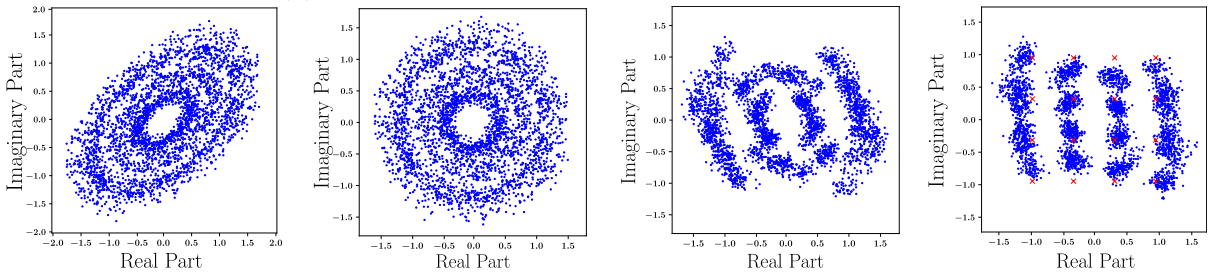

(b) Before any compensation

(c) After IQ imbalance compensation

(d) After CFO compensation

(e) After laser PN compensation

Figure 2.21 – Performance of the first compensation technique in the presence of IQ imbalance on the transmitter and receiver sides

for the FIR filters to not converge to the same output. Finally, after the transmitter IQ imbalance compensation, the more complex strategy for laser PN compensation operates correctly.

The simulation results proved that choosing the optimal strategy using the local compensation approach becomes far from trivial as the number of imperfections increases. Multiple attempts should be performed in order to achieve an acceptable performance. Moreover, this *ad-hoc* strategy is dependent on the imperfections of the optical chain and the compensation algorithms used for a particular impairment compensation.

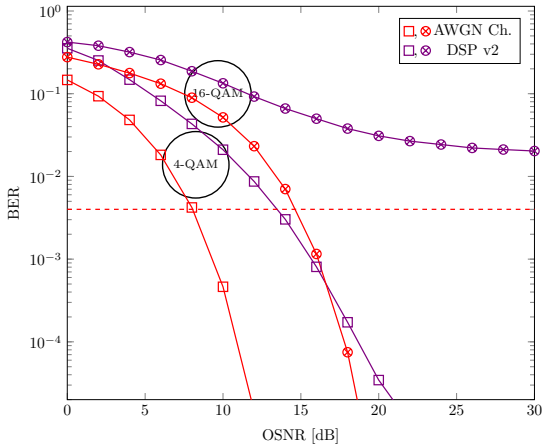

(a) BER performance for multiple values of OSNR

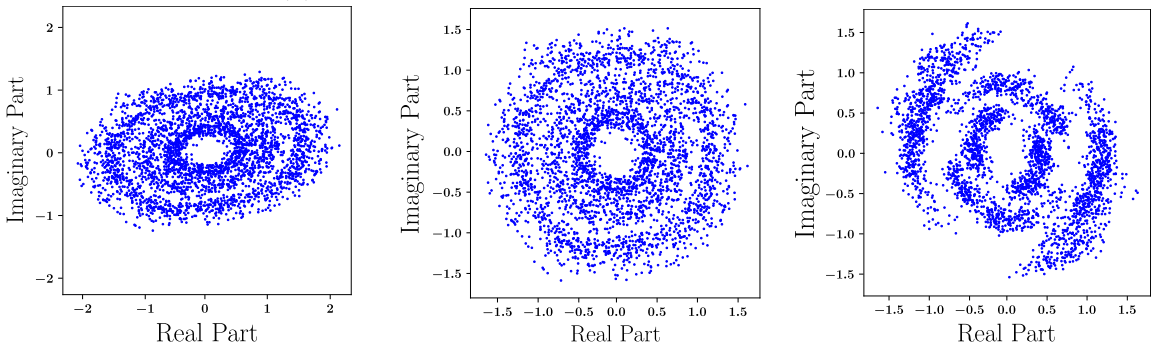

(b) No compensation

(c) Receiver IQ imbalance compensation

(d) CFO compensation

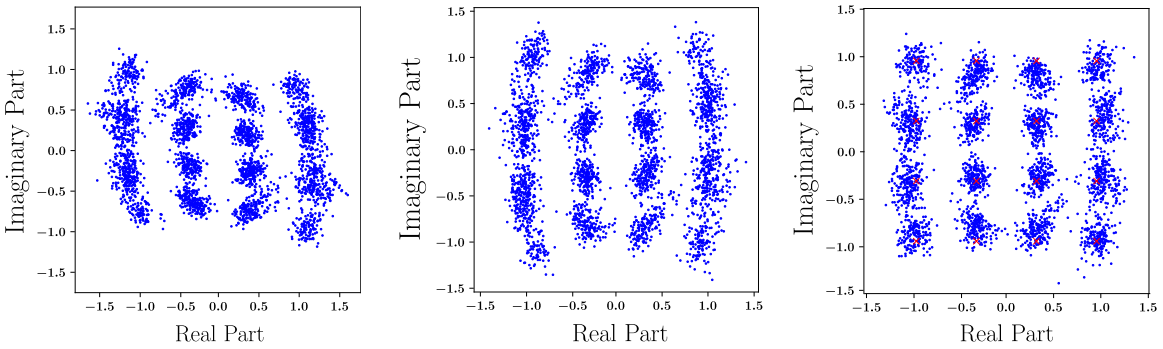

(e) First laser PN compensation

(f) Transmitter IQ imbalance compensation

(g) Second laser PN compensation

Figure 2.22 – Performance of the second compensation scheme in the presence of IQ imbalance on the transmitter and receiver sides

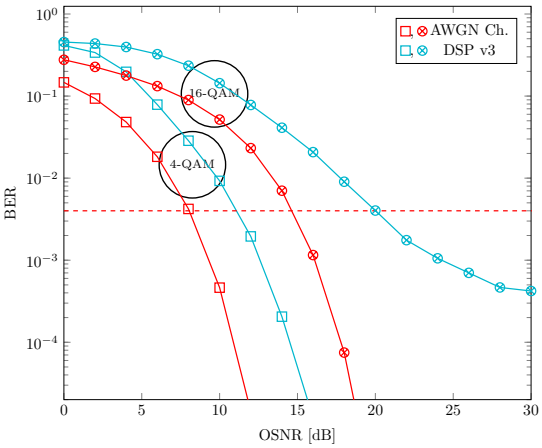

(a) BER performance for multiple values of OSNR

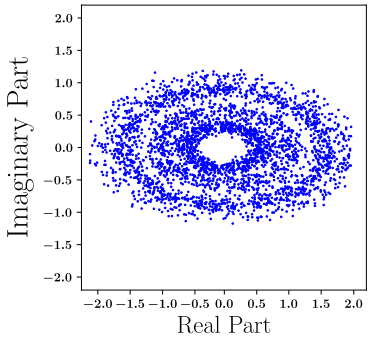

(b) No compensation

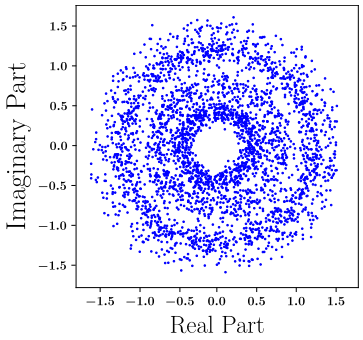

(c) Receiver IQ imbalance compensation

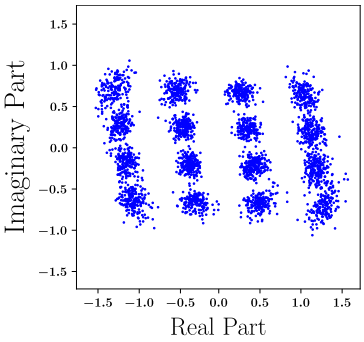

(d) CFO compensation

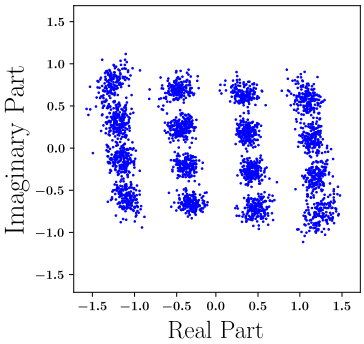

(e) First laser PN compensation

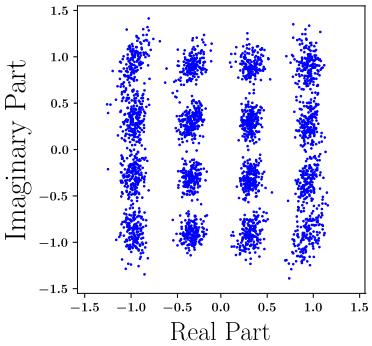

(f) Transmitter IQ imbalance compensation

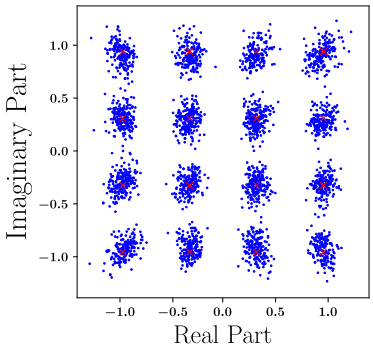

(g) Second laser PN compensation

Figure 2.23 – Performance of the third compensation scheme in the presence of IQ imbalance on the transmitter and receiver sides

2.8 Conclusion and discussion

In this chapter, the linear imperfections of the physical layer in coherent optical communications were investigated. The origin of these imperfections can be multiple like manufacturing faults, channel effects, environmental changes, etc. The linear imperfections analyzed may negatively impact the communication performance, and compensation is required. Consequently, multiple local DSP algorithms have been investigated to compensate for one or a few imperfections. These algorithms are well-studied and have proven their effectiveness in compensating for particular effects. However, coherent optical communications are typically affected by multiple impairments. In this context, the conventional strategy consists in cascading multiple local DSP algorithms to compensate for all chain's imperfections. In this chapter, the effectiveness of this *ad-hoc* approach has been investigated in a simplified scenario where transmission over a dispersion-compensated link was impaired only by IQ imbalance, CFO, and accumulated laser PN on the receiver side. First, the impact of IQ imbalance was simulated only on the receiver side. In this case, the approach consisting of using local DSP algorithms proved to perform well as low penalties were observed at the BER threshold compared to the case where only the AWGN impaired the transmitted signal. On the contrary, the approach seemed to be problematic in the second case, where the IQ imbalance was also present on the transmitter side. First, while the GSOP was efficient in compensating for receiver IQ imbalance, its performance is penalized by the presence of transmitter IQ imbalance. Secondly, the presence of the transmitter IQ imbalance seems to degrade the laser PN compensation performance. Finally, a considerable improvement was obtained after multiple attempts regarding the cascading of compensation algorithms. Nevertheless, the algorithms' choice and arrangement in the DSP block is a difficult task. Many algorithms work in particular simplified scenarios and/or for particular modulation formats. However, general scenarios corresponding to coherent optical communications tend to become more complex. In addition, the increasing demand for flexible optical communications requires adapting the system to different modulation formats. Furthermore, the interaction between multiple local DSP algorithms may be complicated and difficult to interpret. For all the abovementioned reasons, this thesis investigates a different compensation strategy. Instead of cascading multiple local compensation algorithms, the next chapters consider the development of global compensation schemes. The joint compensation of linear imperfections was already considered in the literature, but it was applied only to a limited number

of imperfections. In the table from Appendix A, it can be seen that just a few references from the one discussed earlier consider joint compensation. In addition, this joint compensation generally considers 1 or 2 impairments. It is important to notice that the classification from Appendix A takes into consideration only the results presented in the mentioned references. Many other references exist, and some implement a joint compensation of more imperfections, but it can be deduced that a global compensation of the linear impairments was not achieved until now.

Chapter 3

Global DSP-based compensation of linear imperfections

The previous chapter investigated the impact of linear effects and some benchmark compensation techniques. Even if the impact of a single impairment may be severe, the conventional DSP algorithms are usually efficient in compensating for it. However, coherent optical systems are typically impaired by multiple imperfections. In this scenario, the standard technique for compensation is to cascade multiple DSP algorithms. Each one compensates for a particular effect, with the final aim of recovering the transmitted data. Unfortunately, the cascading of the DSP compensation algorithms is often far from trivial. It was shown that the compensation performance of this cascaded approach might be drastically reduced in the presence of multiple impairments, as some of the techniques designed to compensate for one specific impairment may have poor performance in the presence of others. Moreover, most of the algorithms operate in a specific context or for particular modulation formats, limiting their flexibility. Finally, the interpretability of this approach is a complicated task, as it is unclear how the imperfections and/or the compensation algorithms interact.

To overcome these challenges, a global DSP compensation technique is proposed and discussed in this chapter. This approach aims to estimate and compensate for multiple imperfections globally. Furthermore, the proposed algorithm is modulation-format independent, being suitable for future flexible optical systems. The chapter is organized as follows. First, the global estimation and compensation technique is detailed. Then, this approach is applied in the case of a coherent optical system. Finally, the results obtained by simulations and experimental investigation are analyzed.

3.1 Global estimation and compensation

As seen in Chapter 2, the relation between the transmitted and received data can be mathematically expressed using a linear transformation as follows:

$$\tilde{\mathbf{y}} = \mathbf{M}(\boldsymbol{\alpha})\tilde{\mathbf{x}} + \tilde{\mathbf{b}}, \tag{3.1}$$

where $\mathbf{M}(\boldsymbol{\alpha})$ is a real-valued augmented transfer matrix depending on the unknown vector parameter $\boldsymbol{\alpha}$.

The objective on the receiver side is to detect the transmitted data. Assuming a Gaussian noise and independent and identically distributed symbols, this can be done using a parametric approach as follows:

$$\{\hat{\boldsymbol{\alpha}}, \mathbf{x}_{det}\} = \arg \min_{\boldsymbol{\alpha}, \mathbf{x} \in \mathbb{S}^N} \|\tilde{\mathbf{y}} - \mathbf{M}(\boldsymbol{\alpha})\tilde{\mathbf{x}}\|_2^2. \tag{3.2}$$

However, this minimization problem is hard to solve. To address this problem, one solution is to decouple the estimation problem into multiple parts.

— Estimation of the channel parameters. The unknown parameter $\boldsymbol{\alpha}$ is estimated using a data-aided approach. Specifically, we assume that some data $\mathbf{x}_{DA}$ are known on the receiver side. These data experience the same impairments as useful data. Based on that, a simple approach to estimate the unknown parameter $\boldsymbol{\alpha}$ is to use a Nonlinear Least-Squares (NLS) estimator:

$$\hat{\boldsymbol{\alpha}} = \arg \min_{\boldsymbol{\alpha}} \|\tilde{\mathbf{y}}_{DA} - \mathbf{H}(\boldsymbol{\alpha})\tilde{\mathbf{x}}_{DA}\|_2^2, \tag{3.3}$$

where $\mathbf{y}_{DA}$ represents the received signal corresponding to the known transmitted signal $\mathbf{x}_{DA}$.

— Detection step. By replacing the unknown parameters $\boldsymbol{\alpha}$ by their estimates, the detection step reduces to a classical MIMO detection problem:

$$\mathbf{x}_{det} = \arg \min_{\mathbf{x} \in \mathbb{S}^N} \|\tilde{\mathbf{y}} - \mathbf{M}(\hat{\boldsymbol{\alpha}})\tilde{\mathbf{x}}\|_2^2. \tag{3.4}$$

In this work, for simplicity and computational complexity reasons, we propose to use a simple ZF detector. This detector performs two operations. First, the ZF is

employed for compensation:

$$\hat{\tilde{\mathbf{x}}} = \mathbf{M}^{-1}(\hat{\boldsymbol{\alpha}})\tilde{\mathbf{y}}. \tag{3.5}$$

Then, a hard detection of the transmitted symbols is done as follows:

$$x_{det}[n] = \arg\min_{s\in\mathbb{S}} \|\hat{x}[n] - s\|_2^2. \tag{3.6}$$

Equations (3.3), (3.5), and (3.6) are the backbone of our proposed global estimation and compensation algorithms. The global estimation and compensation technique differs from the conventional approach where the compensation is performed using cascaded DSP algorithms. The proposed approach aims to avoid the difficulties arising from the choice of DSP compensation algorithms and their order in the compensation sequence. In addition, this approach is not limited to particular scenarios or modulation formats. The following sections investigate the proposed technique for the case of SP coherent optical systems.

3.2 Global estimation and compensation in coherent optical systems

An SP coherent optical systems impaired by transmitter and receiver laser PN and IQ imbalance, CD, and CFO is considered. The diagram of the considered system is depicted in Figure 3.1, where marked in red are the parameters related to the imperfections.

3.2.1 Signal model

For a clearer understanding of the order of imperfections impacting the transmitted signal, in Figure 3.2, the block diagram of the communication chain can be seen. First, the transmitted signal $\mathbf{x}$ is impaired by laser PN and IQ imbalance. Then, the signal is sent to the optical channel, where the CD occurs, and the AWGN impact is accumulated at the end of the optical channel. Next, the signal is impaired by CFO, IQ imbalance, and laser PN on the receiver side. Then, the impaired received signal $\mathbf{y}$ goes through a DSP estimation and compensation of impairments to detect the transmitted data.

The impact of imperfections can be modeled as a cascaded Single-Input Single-Output (SISO) signal model, where the transmitted signal encounters multiple imperfections be-

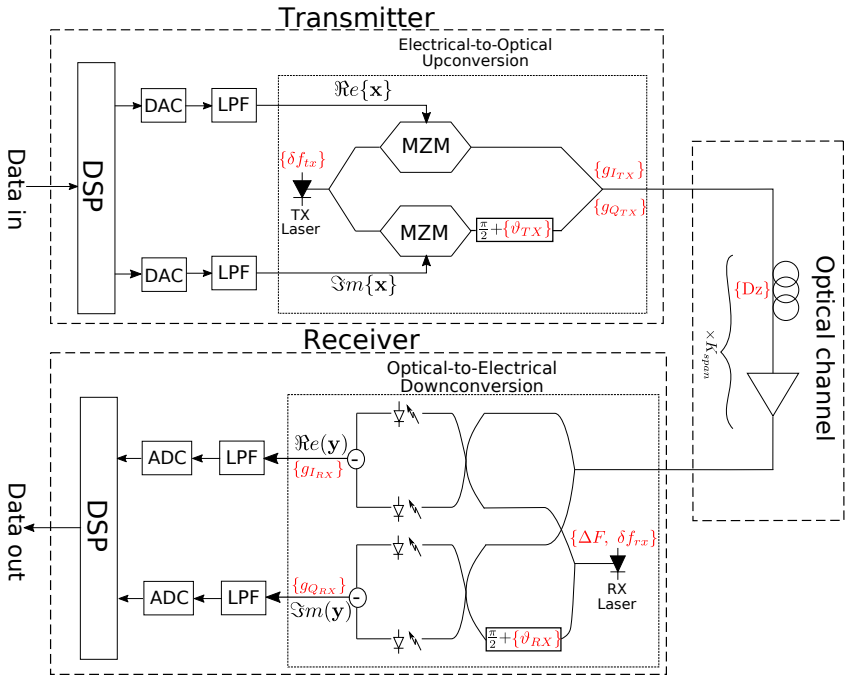

Figure 3.1 – SP coherent optical system impaired by laser PN, IQ imbalance, CD, and CFO; LPF: Low-pass filter

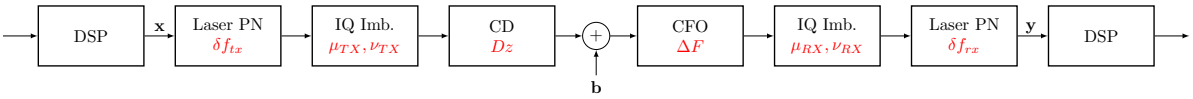

Figure 3.2 – Block diagram of the SP coherent optical system under the impact of multiple linear imperfections

fore being detected on the receiver side. First, the signal is impaired by transmitter laser PN. The impact of transmitter laser PN can be expressed as:

$$\mathbf{z}_1 = \mathbf{\Phi}(\boldsymbol{\phi}_{tx})\mathbf{x}, \tag{3.7}$$

where

$$\mathbf{\Phi} = diag(e^{j\phi_0}, e^{j\phi_1}, \cdots, e^{j\phi_{N-1}}). \tag{3.8}$$

The $diag(.)$ represents the diagonal matrix that contains on the main diagonal its argument elements, and N corresponds to the total number of samples. Then, the signal is

impaired by transmitter IQ imbalance, and can be expressed as follows:

$$\mathbf{z}_2 = \mu_{TX}\mathbf{z}_1 + \nu_{TX}\mathbf{z}_1^*. \tag{3.9}$$

Next, the resulting signal is transmitted over the fiber channel, where it is impaired by CD. The CD impact is modeled in the frequency domain. As a consequence, the impaired signal is expressed by:

$$\mathbf{z}_3 = \mathbf{W}^H\mathbf{D}_1(Dz)\mathbf{W}\mathbf{z}_2, \tag{3.10}$$

where:

— $\mathbf{W}$ is an $N \times N$ Vandermonde matrix corresponding to the Discrete Fourier Transform (DFT) and is defined as:

$$\mathbf{W} = \frac{1}{\sqrt{N}}\begin{bmatrix} 1 & 1 & \dots & 1 \\ 1 & z & & z^{N-1} \\ 1 & z^2 & & z^{2(N-1)} \\ \vdots & \vdots & & \vdots \\ 1 & z^{N-1} & \dots & z^{(N-1)^2}, \end{bmatrix} \tag{3.11}$$

with $z = e^{-2j\pi/N}$. This matrix computes the DFT in the angular frequency range $\left[0, 2\pi\frac{(N-1)f_s}{N}\right]$ in rad/s, where f_s is the sampling frequency.

— $\mathbf{D_1}(Dz)$ is an $N \times N$ diagonal matrix that contains the effect of the CD. The n-th diagonal element of $\mathbf{D_1}(Dz)$ can be expressed by:

$$[\mathbf{D}_1(Dz)]_{nn} = \begin{cases} H_{CD}(2\pi n f_s/N, Dz) & \text{if } n < \frac{N}{2} \\ H_{CD}(2\pi(n-N)f_s/N, Dz) & \text{if } n \geq \frac{N}{2} \end{cases}. \tag{3.12}$$

After the fiber channel, the signal arrives on the receiver side, where it is first impaired by CFO:

$$\mathbf{z}_4 = \mathbf{D}_2(\Delta F)\mathbf{z}_3, \tag{3.13}$$

where $\mathbf{D}_2(\Delta F)$ is an $N \times N$ diagonal matrix whose $n-th$ diagonal element is given by:

$$[\mathbf{D}_2(\Delta F)]_{nn} = e^{j\frac{2\pi n\Delta f}{f_s}}. \tag{3.14}$$

After the CFO impact, the signal undergoes receiver IQ imbalance:

$$\mathbf{z}_5 = \mu_{RX}\mathbf{z}_4 + \nu_{RX}\mathbf{z}_4^*, \tag{3.15}$$

and laser PN:

$$\mathbf{z}_6 = \mathbf{\Phi}(\boldsymbol{\phi}_{rx})\mathbf{z}_5. \tag{3.16}$$

Combining all the above models involved during the communication and adding the noise contribution, we arrive at the following global expression:

$$\begin{aligned}\mathbf{y} = {} & \mu_{RX}\mu_{TX}\mathbf{\Phi}(\boldsymbol{\phi_{rx}})\mathbf{G}(\boldsymbol{\kappa})\mathbf{\Phi}(\boldsymbol{\phi_{tx}})\mathbf{x} \\ & + \mu_{RX}\nu_{TX}\mathbf{\Phi}(\boldsymbol{\phi_{rx}})\mathbf{G}(\boldsymbol{\kappa})\mathbf{\Phi}^*(\boldsymbol{\phi_{tx}})\mathbf{x}^* \\ & + \nu_{RX}\mu_{TX}^*\mathbf{\Phi}(\boldsymbol{\phi_{rx}})\mathbf{G}^*(\boldsymbol{\kappa})\mathbf{\Phi}^*(\boldsymbol{\phi_{tx}})\mathbf{x}^* \\ & + \nu_{RX}\nu_{TX}^*\mathbf{\Phi}(\boldsymbol{\phi_{rx}})\mathbf{G}^*(\boldsymbol{\kappa})\mathbf{\Phi}(\boldsymbol{\phi_{tx}})\mathbf{x} + \mathbf{b}\end{aligned} \tag{3.17}$$

where $\mathbf{G}(\boldsymbol{\kappa}) = \mathbf{D}_2(\Delta F)\mathbf{W}^H\mathbf{D}_1(Dz)\mathbf{W}$ is a $N \times N$ matrix that describes the combined effects of CD and CFO, and $\boldsymbol{\kappa} = \begin{bmatrix} Dz & \Delta F \end{bmatrix}^T$.

3.2.2 Parametric estimation and compensation

3.2.2.1 Assumptions

As discussed previously, the proposed algorithm is composed of two steps: estimation of the channel parameters using a data-aided approach, and ZF compensation and detection.

Regarding the estimation of the channel parameters, as some imperfections can be considered quasi-static (IQ imbalance, CD, CFO) while others are time-variant (the transmit-

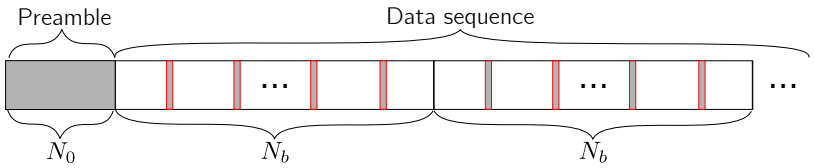

Figure 3.3 – The data frame structure, which consists of a preamble and multiple pilot symbols inserted periodically into the data blocks

Allocation strategy	Data frame	Allocation matrix
Preamble-based	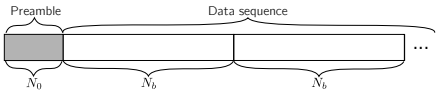	$\mathbf{P}_0 = \begin{bmatrix} \mathbf{I}_{N_0} & 0_{N_0 \times (N-N_0)} \end{bmatrix}$
Pilot-based	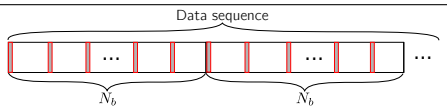	$\mathbf{P}_1 = \mathbf{I}_P \otimes \begin{bmatrix} 1 & 0 & \cdots & 0 \end{bmatrix}$
Hybrid	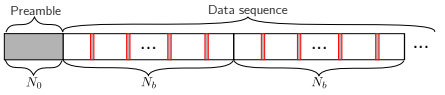	$\mathbf{P}$

Table 3.1 – Different allocation strategies and their corresponding extraction matrices

ter and receiver laser PN), we propose to use both preamble and pilot data. Specifically, the proposed algorithm relies on the frame structure presented in Figure 3.3. This structure consists of a preamble of N_0 length and multiple pilot symbols P inserted periodically into the data blocks of size N_b. The preamble is used to perform a global estimation of the system's parameters, while the pilot symbols are used to perform phase tracking over the data blocks. This allocation scheme requires the employment of an extraction matrix on the receiver side. This matrix extracts the training data and contains 0s on all of its entries, except the ones corresponding to the training symbols' positions in the data blocks, which contain 1s. For a better understanding, in Table 3.1 multiple allocation strategies and the corresponding extraction matrices are shown.

In the following, to address the data-aided estimation problem, we express the signal model in a more convenient form as follows:

$$\mathbf{y} = \mathbf{A}(\mathbf{x}, \boldsymbol{\kappa}, \boldsymbol{\phi})\boldsymbol{\chi} + \mathbf{b}, \tag{3.18}$$

where:

— $\mathbf{A}(\mathbf{x}, \boldsymbol{\kappa}, \boldsymbol{\phi})$ is an $N \times 4$ matrix describing the combined effects of the CD, CFO, and PN:

$$\mathbf{A}(\mathbf{x}, \boldsymbol{\kappa}, \boldsymbol{\phi}) = \begin{bmatrix} \boldsymbol{\Phi}(\boldsymbol{\phi}_{rx})\mathbf{G}(\boldsymbol{\kappa})\boldsymbol{\Phi}(\boldsymbol{\phi}_{tx})\mathbf{x} \\ \boldsymbol{\Phi}(\boldsymbol{\phi}_{rx})\mathbf{G}(\boldsymbol{\kappa})\boldsymbol{\Phi}^*(\boldsymbol{\phi}_{tx})\mathbf{x}^* \\ \boldsymbol{\Phi}(\boldsymbol{\phi}_{rx})\mathbf{G}^*(\boldsymbol{\kappa})\boldsymbol{\Phi}^*(\boldsymbol{\phi}_{tx})\mathbf{x}^* \\ \boldsymbol{\Phi}(\boldsymbol{\phi}_{rx})\mathbf{G}^*(\boldsymbol{\kappa})\boldsymbol{\Phi}(\boldsymbol{\phi}_{tx})\mathbf{x} \end{bmatrix}^T, \tag{3.19}$$

with $\boldsymbol{\phi} = \begin{bmatrix}\boldsymbol{\phi}_{tx}^T & \boldsymbol{\phi}_{rx}^T\end{bmatrix}^T$ denoting the transmitter and receiver lasers' phases.

— $\boldsymbol{\chi}$ is a column vector describing the IQ imbalance parameters:

$$\boldsymbol{\chi} = \begin{bmatrix} \mu_{RX}\mu_{TX} \\ \mu_{RX}\nu_{TX} \\ \nu_{RX}\mu_{TX}^* \\ \nu_{RX}\nu_{TX}^* \end{bmatrix}. \tag{3.20}$$

— $\mathbf{b}$ is a column vector containing the AWGN.

Equation (3.18) serves as the basis for the estimation algorithm. In (3.18), some parameters are nonlinear ($\boldsymbol{\kappa}$, $\boldsymbol{\phi}$), while others are linear ($\boldsymbol{\chi}$) with respect to the received signal $\mathbf{y}$.

In (3.18), the laser phase is usually modeled as a Wiener noise. Using this model requires estimating N parameters for a single laser phase. As N is greater than the number of preamble and pilot samples, the unique identification of the model parameter is impossible. In practice, it is important to note that the laser phase has a slower evolution compared to the signal phase [Kik15]. Based on these, we have considered two different low-dimensional models for the laser phase.

— *Common phase model*: The common phase model assumes that the laser phase is constant for several K consecutive symbols [Hua+13]. Using this assumption, the matrix containing the laser phase samples can be redefined as follows:

$$\boldsymbol{\Phi}_{CP}(\boldsymbol{\phi}) = diag(e^{j\phi_0}, e^{j\phi_1}, \cdots, e^{j\phi_{N/K-1}}) \otimes \mathbf{I}_K, \tag{3.21}$$

where $\boldsymbol{\Phi}_{CP}(\boldsymbol{\phi})$ is the common phase representation of the laser phase, $\mathbf{I}_K$ an identity matrix of size K, and $\otimes$ denotes the Kronecker product. It can be stated that this model does not follow the exact evolution of the laser phase.

— *Polynomial model*: The polynomial model assumes that the laser phase can be modeled as a polynomial of order A. Using this model, the laser phase is expressed as follows:

$$\boldsymbol{\Phi}_{PN}(\boldsymbol{\phi}) = \begin{bmatrix} 1 & x_0 & x_0^2 & \cdots & x_0^A \\ 1 & x_1 & x_1^2 & \cdots & x_1^A \\ & & \vdots & & \\ 1 & x_{N-1} & x_{N-1}^2 & \cdots & x_{N-1}^A \end{bmatrix} \begin{bmatrix} a_0 \\ a_1 \\ \vdots \\ a_A \end{bmatrix}, \tag{3.22}$$

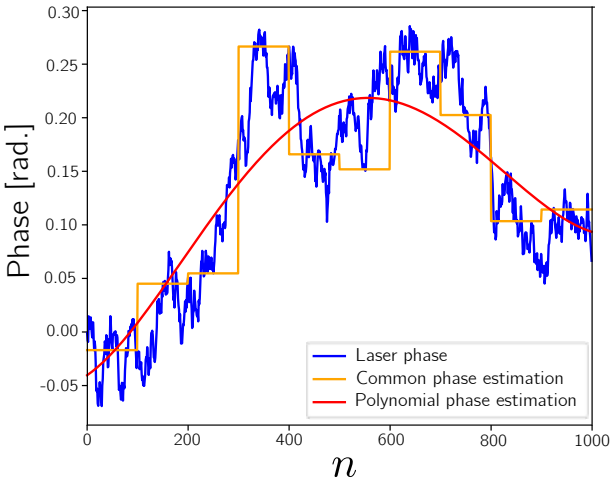

Figure 3.4 – Laser phase tracking using common phase and polynomial models

where $\mathbf{\Phi}_{PN}(\boldsymbol{\phi})$ is the polynomial representation of the laser phase. This model may be more adapted than the common phase one, as it can better reproduce the dynamics of the laser phase.

Both discussed laser phase models provide a good compromise as it reduces the computational complexity by diminishing the number of parameters to be estimated. An example of laser phase tracking using these two models is depicted in Figure 3.4.

3.2.2.2 Preamble-based estimation

The preamble sequence is generally of short length (from a few tens to a few hundreds of symbols). In this case, the laser phase can be assumed to be constant during the whole preamble length. Hence, the common phase model of the laser phase can be readily employed, and the matrices $\mathbf{\Phi}(\boldsymbol{\phi}_{tx})$ and $\mathbf{\Phi}(\boldsymbol{\phi}_{rx})$ reduce to scalar matrices as follows:

$$\mathbf{\Phi}(\boldsymbol{\phi}_{tx}) = e^{j\phi_{tx,0}}\mathbf{I}_{N_0}, \tag{3.23a}$$

$$\mathbf{\Phi}(\boldsymbol{\phi}_{rx}) = e^{j\phi_{rx,0}}\mathbf{I}_{N_0}. \tag{3.23b}$$

In this context, the impact of laser PN can be transferred to the IQ phase imbalance. Using this, the signal equation (3.18) can be rewritten as:

$$\mathbf{y} = \mathbf{A}(\mathbf{x}, \boldsymbol{\kappa})\boldsymbol{\chi}_{\phi} + \mathbf{b}, \tag{3.24}$$

where:

— $\mathbf{A}(\mathbf{x}, \boldsymbol{\kappa}) = \mathbf{A}(\mathbf{x}, \boldsymbol{\kappa}, 0)$ is an $N_0 \times 4$ matrix describing the impact of the CD and CFO, and is defined as:

$$\mathbf{A}(\mathbf{x}, \boldsymbol{\kappa}) = \begin{bmatrix} \mathbf{G}(\boldsymbol{\kappa})\mathbf{x} & \mathbf{G}(\boldsymbol{\kappa})\mathbf{x}^* & \mathbf{G}^*(\boldsymbol{\kappa})\mathbf{x}^* & \mathbf{G}^*(\boldsymbol{\kappa})\mathbf{x} \end{bmatrix}. \tag{3.25}$$

— $\boldsymbol{\chi}_\phi$ is a column vector consisting of the IQ imbalance parameters and the lasers' PNs, and is obtained as follows:

$$\boldsymbol{\chi}_\phi = \mathbf{D}_\phi \boldsymbol{\chi}, \tag{3.26}$$

with $\mathbf{D}_\phi$ the diagonal matrix represented as:

$$\mathbf{D}_\phi = e^{j\phi_{rx,0}} diag(e^{j\phi_{tx,0}}, e^{-j\phi_{tx,0}}, e^{-j\phi_{tx,0}}, e^{j\phi_{tx,0}}). \tag{3.27}$$

The assumption of a constant laser phase over the whole preamble reduces the number of nonlinear parameters. It can be observed that only 2 nonlinear parameters have to be estimated. By this, the computational complexity is limited.

The estimation can be naturally performed by using NLS, which minimizes the squared error between the received signal and the model output:

$$\{\hat{\boldsymbol{\kappa}}, \hat{\boldsymbol{\chi}}_\phi\} = \arg\min_{\boldsymbol{\kappa}, \boldsymbol{\chi}_\phi} \|\mathbf{y} - \mathbf{A}(\mathbf{x}, \boldsymbol{\kappa})\boldsymbol{\chi}_\phi\|^2. \tag{3.28}$$

Assuming circular Gaussian noise, the NLS estimator corresponds to the Maximum Likelihood Estimator (MLE), which is asymptotically optimal. For this particular signal model, it was demonstrated that the global estimation could be split into two steps. This technique is named Separable NLS [Gol+73; Kay93] and is performed as follows:

1. Estimation of the nonlinear parameters $\boldsymbol{\kappa}$:

$$\hat{\boldsymbol{\kappa}} = \arg\min_{\boldsymbol{\kappa}} \|\mathbf{f}_{\boldsymbol{\kappa}}\|^2, \tag{3.29}$$

where $\mathbf{f}_{\boldsymbol{\kappa}}$ computes the vector of residuals:

$$\mathbf{f}_{\boldsymbol{\kappa}} = \boldsymbol{\Pi}_{\mathbf{A}}(\mathbf{x}, \boldsymbol{\kappa})\mathbf{y}, \tag{3.30}$$

with $\boldsymbol{\Pi}_{\mathbf{A}}(\mathbf{x}, \boldsymbol{\kappa}) = \mathbf{I}_{N_0} - \mathbf{P}_{\mathbf{A}}(\mathbf{x}, \boldsymbol{\kappa})$, $\mathbf{I}_{N_0}$ is an $N_0 \times N_0$ identity matrix, and $\mathbf{P}_{\mathbf{A}}(\mathbf{x}, \boldsymbol{\kappa})$ the projection matrix onto the column space of $\mathbf{A}(\mathbf{x}, \boldsymbol{\kappa})$. $\mathbf{P}_{\mathbf{A}}(\mathbf{x}, \boldsymbol{\kappa})$ is obtained as

$\mathbf{P}_{\mathbf{A}}(\mathbf{x}, \boldsymbol{\kappa}) = \mathbf{A}(\mathbf{x}, \boldsymbol{\kappa})\mathbf{A}^{\dagger}(\mathbf{x}, \hat{\boldsymbol{\kappa}})$, where $\mathbf{A}^{\dagger}(\mathbf{x}, \hat{\boldsymbol{\kappa}})$ is the pseudoinverse of $\mathbf{A}(\mathbf{x}, \boldsymbol{\kappa})$ and is defined as $\mathbf{A}^{\dagger}(\mathbf{x}, \hat{\boldsymbol{\kappa}}) = (\mathbf{A}^{H}(\mathbf{x}, \boldsymbol{\kappa})\mathbf{A}(\mathbf{x}, \boldsymbol{\kappa}))^{-1}\mathbf{A}^{H}(\mathbf{x}, \boldsymbol{\kappa})$,

2. Estimation of the linear parameters $\boldsymbol{\chi}_{\phi}$ using the estimate $\hat{\boldsymbol{\kappa}}$ as:

$$\hat{\boldsymbol{\chi}}_{\phi} = \mathbf{A}^{\dagger}(\mathbf{x}, \hat{\boldsymbol{\kappa}})\mathbf{y}. \tag{3.31}$$

In the proposed estimation algorithm, the most complicated task is the minimization problem in (3.29). Indeed, the cost function may have multiple local minima as illustrated in Figure 3.5. To overcome this problem, a global optimization algorithm should be used. However, these kinds of algorithms are very computationally demanding and require many iterations to obtain acceptable results. As a consequence, in this work, a hybrid technique is exploited. This technique switches from a global optimization approach that performs a coarse estimation of the parameters to local optimization. The local optimization performs a finer estimation of the parameters and is less computationally demanding. Specifically, we propose the following methodology.

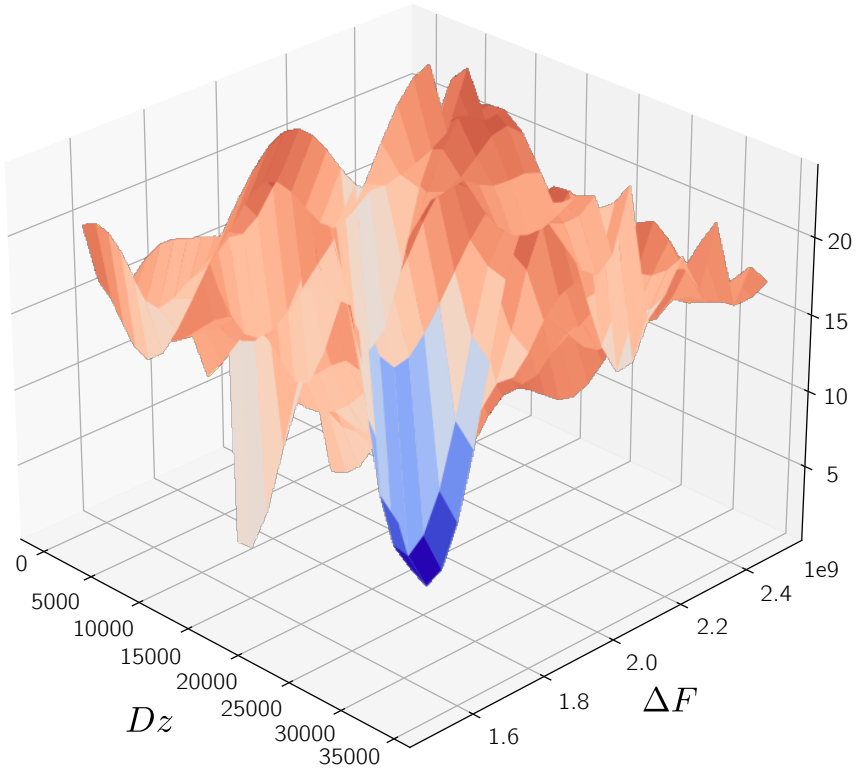

Figure 3.5 – A graphical representation of the cost function corresponding to the nonlinear parameters $Dz \in [0, 35000]$ ps/nm and $\Delta F \in [1.5, 2.5]$ GHz

— *Coarse estimation*: A grid search is first performed in a two-dimensional space to obtain an initial estimate of $\boldsymbol{\kappa}$. The grid search computes the values of the cost function for each point of a 2D grid $\mathcal{K}$ as follows:

$$\hat{\boldsymbol{\kappa}}_0 = \arg\min_{\boldsymbol{\kappa}\in\mathcal{K}} \|\mathbf{f}_{\boldsymbol{\kappa}}\|^2, \tag{3.32}$$

where $\mathcal{K} = \{(Dz_0, \Delta F_0), \cdots, (Dz_{L_1-1}, \Delta F_{L_2-1})\}$ contains combinations of candidate values, with L_1 and L_2 being their total number for Dz and ΔF, respectively.

— *Finer estimation*: The local optimization is initialized with the output of the coarse estimation $\hat{\boldsymbol{\kappa}}_0$. For local optimization, we propose to use the Levenberg-Marquardt (LM) algorithm [Mor78]. LM algorithm is an iterative approach that relies on interpolation between the gradient descent and Gauss-Newton algorithms. It is robust in avoiding local minima and has an adaptive convergence rate that can approach one of the Gauss-Newton algorithm. The update is performed as follows:

$$\boldsymbol{\kappa}_{k+1}^T = \boldsymbol{\kappa}_k^T - [\mathbf{J}_{\boldsymbol{\kappa}}^T\mathbf{J}_{\boldsymbol{\kappa}} + \lambda_{\boldsymbol{\kappa}}\mathbf{I}_2]^{-1}\mathbf{J}_{\boldsymbol{\kappa}}^T\mathbf{f}_{\boldsymbol{\kappa}}\Big|_{\boldsymbol{\kappa}=\boldsymbol{\kappa}_k}, \tag{3.33}$$

where $\mathbf{J}_{\boldsymbol{\kappa}}$ is an $N_0 \times 2$ Jacobian matrix of $\mathbf{f}_{\boldsymbol{\kappa}}$, $\mathbf{I}_2$ is a 2×2 identity matrix, and $\lambda_{\boldsymbol{\kappa}}$ is a damping parameter controlling the update step. The Jacobian matrix related to $\mathbf{f}_{\boldsymbol{\kappa}}$ can be obtained as follows:

$$\mathbf{J}_{\boldsymbol{\kappa}} = \begin{bmatrix} \frac{\partial \mathbf{f}_{\boldsymbol{\kappa}}}{\partial \kappa_0} & \frac{\partial \mathbf{f}_{\boldsymbol{\kappa}}}{\partial \kappa_1} \end{bmatrix} = \begin{bmatrix} \frac{\partial \mathbf{P}_{\mathbf{A}}^{\perp}(\boldsymbol{\kappa})}{\partial \kappa_0}\mathbf{y} & \frac{\partial \mathbf{P}_{\mathbf{A}}^{\perp}(\boldsymbol{\kappa})}{\partial \kappa_1}\mathbf{y} \end{bmatrix}, \tag{3.34}$$

where the derivative of the orthogonal projector is computed as in [Vib+91]:

$$\frac{\partial \boldsymbol{\Pi}_{\mathbf{A}}(\boldsymbol{\kappa})}{\partial \kappa_i} = -\mathbf{P}_{\mathbf{A}}^{\perp}(\boldsymbol{\kappa})\frac{\partial \mathbf{A}(\boldsymbol{\kappa})}{\partial \kappa_i}\mathbf{A}^{\dagger}(\boldsymbol{\kappa}) - \left(\mathbf{P}_{\mathbf{A}}^{\perp}(\boldsymbol{\kappa})\frac{\partial \mathbf{A}(\boldsymbol{\kappa})}{\partial \beta_i}\mathbf{A}^{\dagger}(\boldsymbol{\kappa})\right)^H, \tag{3.35}$$

and κ is the i-th element of $\boldsymbol{\kappa}$.

3.2.2.3 Pilot-based tracking and compensation

Static and time-variant imperfections impair the considered setup. During the preamble-based estimation, the system's parameters were globally estimated. However, the lasers' phases change in time and must be re-estimated during communication. In this work, this is achieved by using pilot symbols that are inserted periodically into the data block N_b.

Using the same mathematical development as in [Fru+21a], the real-valued augmented model of the system can be rewritten as:

$$\tilde{\mathbf{y}} = \tilde{\mathbf{\Phi}}(\boldsymbol{\varphi_{rx}})\mathbf{M}\tilde{\mathbf{\Phi}}(\boldsymbol{\varphi_{tx}})\tilde{\mathbf{x}} + \tilde{\mathbf{b}}, \tag{3.36}$$

where

— $\mathbf{M}$ is an $2N_b \times 2N_b$ augmented matrix which is defined as:

$$\mathbf{M} = \begin{bmatrix} \Re e(\mathbf{M}_1) & -\Im m(\mathbf{M}_2) \\ \Im m(\mathbf{M}_1) & \Re e(\mathbf{M}_2) \end{bmatrix}, \tag{3.37}$$

with:

$$\mathbf{M}_1 = (\boldsymbol{\chi}_\phi^T(\mathbf{e}_0 + \mathbf{e}_1))\mathbf{G}(\boldsymbol{\kappa}) + (\boldsymbol{\chi}_\phi^T(\mathbf{e}_2 + \mathbf{e}_3))\mathbf{G}^*(\boldsymbol{\kappa}), \tag{3.38a}$$
$$\mathbf{M}_2 = (\boldsymbol{\chi}_\phi^T(\mathbf{e}_0 - \mathbf{e}_1))\mathbf{G}(\boldsymbol{\kappa}) + (\boldsymbol{\chi}_\phi^T(\mathbf{e}_3 - \mathbf{e}_2))\mathbf{G}^*(\boldsymbol{\kappa}), \tag{3.38b}$$

while $\mathbf{e}_k$ is a unit column vector containing a single 1 value at the $k-th$ row and 0s elsewhere,

— $\tilde{\mathbf{\Phi}}(\boldsymbol{\varphi_{tx}})$ and $\tilde{\mathbf{\Phi}}(\boldsymbol{\varphi_{rx}})$ are $2N_b \times 2N_b$ augmented matrices defined similarly to $\tilde{\mathbf{\Phi}}(\boldsymbol{\varphi})$ as follows:

$$\tilde{\mathbf{\Phi}}(\boldsymbol{\varphi}) = \begin{bmatrix} \Re e(\mathbf{\Phi}(\boldsymbol{\varphi})) & -\Im m(\mathbf{\Phi}(\boldsymbol{\varphi})) \\ \Im m(\mathbf{\Phi}(\boldsymbol{\varphi})) & \Re e(\mathbf{\Phi}(\boldsymbol{\varphi})) \end{bmatrix}. \tag{3.39}$$

Using this re-parametrization of the model, the laser phase can be estimated using the P pilot symbols by minimizing the following function:

$$\{\hat{\boldsymbol{\varphi}}\} = \arg\min_{\boldsymbol{\varphi}} \|\mathbf{f}_{\boldsymbol{\varphi}}\|^2. \tag{3.40}$$

where $\boldsymbol{\varphi} = \begin{bmatrix} \boldsymbol{\varphi}_{tx}^T & \boldsymbol{\varphi}_{rx}^T \end{bmatrix}^T$, and $\mathbf{f}_{\boldsymbol{\varphi}}$ is a function that computes the vector of residuals. By using the fact that $\tilde{\mathbf{\Phi}}^{-1}(\boldsymbol{\varphi}) = \tilde{\mathbf{\Phi}}^T(\boldsymbol{\varphi})$, the function can defined as:

$$\mathbf{f}_{\boldsymbol{\varphi}} = \tilde{\mathbf{x}}_1 - \tilde{\mathbf{P}}_1\tilde{\mathbf{\Phi}}^T(\boldsymbol{\varphi_{tx}})\mathbf{M}^{-1}\tilde{\mathbf{\Phi}}^T(\boldsymbol{\varphi_{rx}})\tilde{\mathbf{y}}, \tag{3.41}$$

where $\mathbf{x}_1$ are the transmitted pilot symbols. It is essential to notice that by using the before-mentioned relation, the algorithm directly estimates the matrices that compensate

for the laser PN. This way, the matrix inversion is avoided, and a transpose is computed instead, reducing computational complexity. Moreover, the inversion of $\mathbf{M}$ is performed only once, as it does not depend on the time-variant parameters.

The minimization of the function from (3.40) can also be performed in multiple manners. In this case, the cost function is assumed to be convex and can be minimized using a local optimization algorithm. By establishing this, the optimization is also performed using the LM algorithm. First, the laser phase is initialized with 0s values, and then the update is performed similarly to the one in (3.33). The $2P \times P$ Jacobian matrix corresponding to the function $\mathbf{f}_{\boldsymbol{\varphi}}$ is expressed as:

$$\mathbf{J}_{\boldsymbol{\varphi}} = \left[\frac{\partial \mathbf{f}_{\boldsymbol{\varphi}}}{\partial \varphi_{tx,0}} \quad \cdots \quad \frac{\partial \mathbf{f}_{\boldsymbol{\varphi}}}{\partial \varphi_{tx,P/2-1}} \quad \frac{\partial \mathbf{f}_{\boldsymbol{\varphi}}}{\partial \varphi_{rx,P/2}} \quad \cdots \quad \frac{\partial \mathbf{f}_{\boldsymbol{\varphi}}}{\partial \varphi_{rx,P-1}} \right], \tag{3.42}$$

where:

$$\frac{\partial \mathbf{f}_{\boldsymbol{\varphi}}}{\partial \varphi_{tx,i}} = -\tilde{\mathbf{P}}_1 \frac{\partial \tilde{\boldsymbol{\Phi}}^T(\boldsymbol{\varphi_{tx}})}{\partial \varphi_{tx,i}} \mathbf{M}^{-1} \tilde{\boldsymbol{\Phi}}^T(\boldsymbol{\varphi_{rx}}) \tilde{\mathbf{y}}, \tag{3.43a}$$

$$\frac{\partial \mathbf{f}_{\boldsymbol{\varphi}}}{\partial \varphi_{rx,i}} = -\tilde{\mathbf{P}}_1 \tilde{\boldsymbol{\Phi}}^T(\boldsymbol{\varphi_{tx}}) \mathbf{M}^{-1} \frac{\partial \tilde{\boldsymbol{\Phi}}^T(\boldsymbol{\varphi_{rx}})}{\partial \varphi_{rx,i}} \tilde{\mathbf{y}}. \tag{3.43b}$$

As both lasers' phases used for compensation are jointly estimated, the estimation in (3.40) introduces a phase indetermination. Consequently, a constant difference between real and estimated phase values is generally visible. Figure 3.6 shows a single realization of the global estimation of both lasers' phases related to 100 kHz laser linewidth in a noiseless 16-QAM transmission. In this figure, the constant difference is removed artificially for ease of comparison. In contrast to the conventional DSP algorithms, which cannot discriminate between the two lasers' phases, it can be seen that the proposed technique can track both transmitter and receiver lasers' phases jointly.

After the global estimation of parameters using the preamble data and tracking the time-variant lasers' phases, the impact of imperfections can be mitigated, and the transmitted data can be recovered. The ZF equalizer compensates for the imperfections' impact. It consists of an inversion of the channel transfer matrix to recover the transmitted symbols:

$$\hat{x}[n] = (\mathbf{e}_n + j\mathbf{e}_{n+N_b})^T \tilde{\boldsymbol{\Phi}}^T(\hat{\boldsymbol{\varphi}}_{tx}) \mathbf{M}^{-1} \tilde{\boldsymbol{\Phi}}^T(\hat{\boldsymbol{\varphi}}_{rx}) \tilde{\mathbf{y}}. \tag{3.44}$$

A detection is finally performed using a hard projector:

$$x_{det}[n] = \arg\min_{s\in\mathbb{S}} \|\hat{x}[n] - s\|_2^2. \tag{3.45}$$

where $x_{det}[n]$ represents the $n-th$ estimated constellation symbol.

3.3 Results

In this section, the performance of the proposed approach is evaluated. The section is divided into three subsections. First, the performance is assessed by using numerical simulations in a complex scenario where all considered imperfections impact the transmitted signal. The second subsection presents a comparative study by considering a few conventional DSP algorithms. Finally, the last subsection is dedicated to an experimental demonstration of the approach using a simplified scenario.

The implementation of the transmission systems impaired by multiple imperfections is done using Python scientific libraries such as NumPy [Har+20], and SciPy [Vir+20]. The LM algorithm is implemented by calling a wrapper over the LS algorithm from MINPACK [Mor+80].

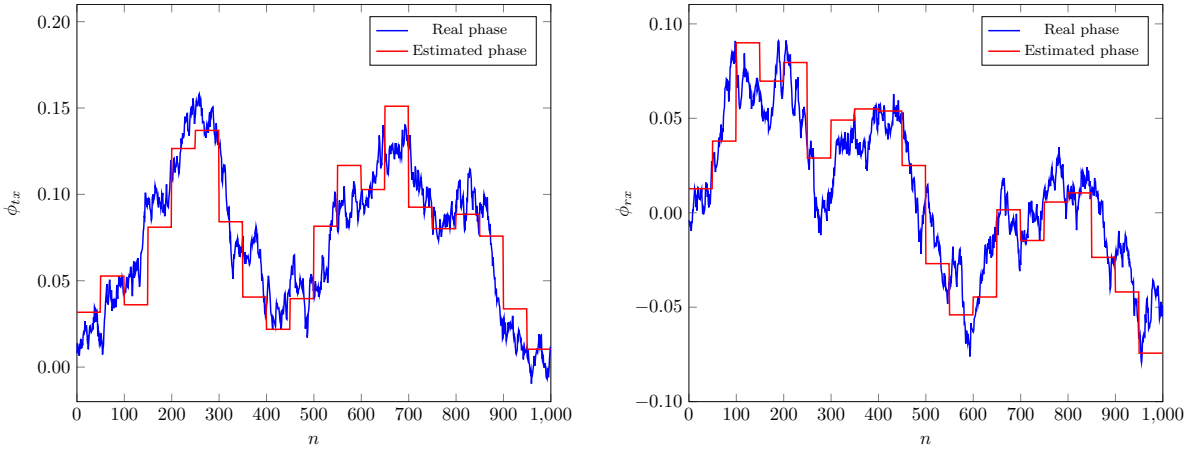

(a) Transmitter laser phase tracking (b) Receiver laser phase tracking

Figure 3.6 – Laser phase estimation for an ideal 16-QAM transmission

3.3.1 Simulation results

This chapter considers an $\mathcal{M}$-QAM coherent optical system impacted by multiple impairments. The system's parameters can be seen in Table 3.2. The communication is achieved at the wavelength of 1550 nm with bandwidth and a sampling frequency f_s of 30 GHz. The preamble consists of 100 symbols belonging to the payload constellation set $\mathbb{S}$. The data blocks have a length of 300 symbols, of which some are pilot symbols. The considered imperfections' parameters are reported in Table 3.3. The transmitted signal is impaired by an IQ imbalance of (1 dB, 10°), both on the transmitter and receiver sides. The lasers' PNs are related to laser linewidth between 100 kHz and 500 kHz, the accumulated CD is of 17000 ps/nm, corresponding to a fiber length of $z = 1000$ km with a dispersion coefficient of $D = 17$ ps/nm-km, and the CFO is of 2 GHz.

Considering this scenario, the estimation and compensation results are analyzed in the following.

3.3.1.1 Preamble-based estimation performance

This subsection presents the performance of the preamble-based estimation technique. This estimation is conducted using the preamble data and is divided into two parts: the estimation of the nonlinear parameters $\boldsymbol{\kappa}$ and the estimation of the linear parameters $\boldsymbol{\chi}$. In the following, the estimation performance is only reported for the nonlinear parameters $\boldsymbol{\kappa}$ because the estimation of linear parameters directly depends on the estimation performance of the nonlinear parameters (see eq. (3.31)).

As previously discussed in 3.2.2.2, the nonlinear parameters are estimated using a hybrid strategy. First, a global optimization using grid search is carried out. In this case, a search interval for grid search should be introduced. This interval is tuned according to the following rules:

— In the case of accumulated CD, prior knowledge about the corresponding parameter Dz can be assumed. In the following, an interval of fiber length between 950 km and 1050 km is considered. In this way, the computational demands are also

Table 3.2 – System parameters

BW [GHz]	**f_s [GHz]**	**λ [nm]**	**N_0**	**N_b**
30	30	1550	100	300

Table 3.3 – Imperfections parameters

$g_{TX/RX}$ [dB]	$\vartheta_{TX/RX}$ [deg.]	Dz [ps/nm]	ΔF [GHz]	$\delta f_{tx/rx}$ [kHz]
1	10	17000	2	[100;500]

reduced as a lower number of iterations may provide a good initialization value;

— In the case of the CFO parameter ΔF, there is no prior knowledge, so a search interval $\pm$ 3 GHz is considered, as over the lifetime of a typical tunable laser, the CFO can be as large as $\pm$ 2.5 GHz [For15].

Secondly, the optimization switch to the LM algorithm, which uses the grid search's estimated values as initialization values.

Initially, an ideal case where the communication is not impacted by laser PN ($\boldsymbol{\phi}_{tx} = \boldsymbol{\phi}_{rx} = \mathbf{0}$) over the whole preamble is considered. In this scenario, we have also derived the expression of the Cramér Rao Lower Bound (CRLB) to compare the performance of the NLS estimator technique with the optimal one. The CRLB is the variance's lower bound of any unbiased estimator [Kay93]. The CRLB is determined by inverting the Fisher information matrix. Its computation can be found in Appendix B.

As in this work, the AWGN contribution is considered before the receiver IQ imbalance, the noise statistics are modified, and the circularity property does not hold (see eq. (3.28)). In Figure 3.7, the evolution of the MSE by varying N_0 for a single OSNR value of 20 dB is shown. The N_0 variation is done with a step size of 1, while the curves' markers are

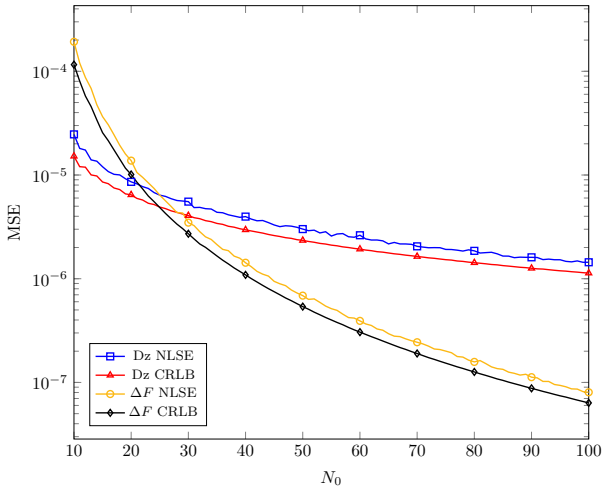

Figure 3.7 – MSE evolution of the NLS estimator and CRLB for an OSNR of 20 dB for multiple values of N_0

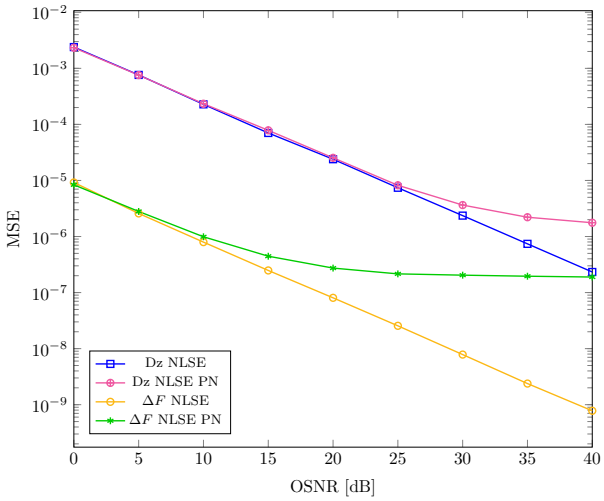

Figure 3.8 – MSE evolution of the NLS estimator for multiple values of OSNR

displayed every 10 samples. It should be noted that the NLS estimator has a similar evolution to the CRLB, but it is not optimal, as a performance gap can be observed.

In practice, the impact of the laser PN cannot be neglected. In the following, the influence of laser PN on the estimation performance of the nonlinear parameters $\boldsymbol{\kappa}$ is analyzed. A scenario where the laser PN occurs over the preamble data is considered to evaluate the estimation performance. "NLSE PN" denotes the estimator used in this case. In Figure 3.8, the evolution of the MSE for different values of OSNR using a fixed-length preamble of 100 symbols is depicted. The performance is compared to the one obtained in the scenario where the transmission is not impaired by laser PN. It can be seen that the estimation in the presence of laser PN reaches a floor for both parameters. This is due to the approximate model of the laser phase employed. However, at this point, the MSE values are reduced.

3.3.1.2 Compensation performance

This subsection analyses the performance of the proposed technique using the BER metric. In each simulation, the impairments parameters are replaced by their estimates.

First, the performance of the compensation method is assessed with respect to the number of pilots P. In the following simulations, the BER performance of the approach is computed for 16-QAM communications with laser linewidths of $\delta f_{tx} = \delta f_{rx} = 100$. Multiple pilot symbols are used (0, 2, 4, 6, 12, and 30 pilot symbols). Regarding the common phase model, the number of constant phase levels assumed is equal to $K = N_b/P$.

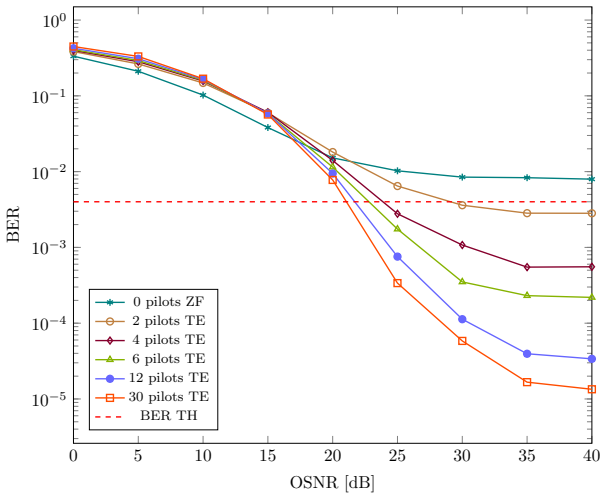

Figure 3.9 – BER evolution for multiple values of OSNR with $\delta f_{tx} = \delta f_{rx} = 100$ kHz, and different values for the number of pilots P

When no pilot symbol is used, the algorithm does not perform any tracking of the lasers' phases and is denoted as "ZE". On the other hand, the equalizer performing phase tracking is denoted as "TE". In Figure 3.9, it can be seen that the performance of the "TE" approach increases with the number of pilot symbols. For the case where no pilot symbol is used, the performance does not even reach the required QoS. On the contrary, when 30 pilot symbols are used, the BER decreases to values of approximately 10^{-5}. It can also be observed that better performance is obtained for a low number of pilots at low to medium OSNRs. On the other hand, better performances are obtained when more pilot symbols are employed after medium OSNR values. On low-medium values of OSNR, the pilot-based estimation is highly impacted by noise, and overfitting occurs. When the noise contribution is reduced, the model with multiple pilots describes the laser phase dynamics more accurately, and better performance is obtained. To maintain a good compromise between performance and computational complexity, all the following simulations consider 12 pilot symbols and 12 constant levels of the phase ($K = 25$).

Next, the robustness of the proposed approach to the laser PN is measured. To do that, in Figure 3.10, the performance of the approach for 16-QAM communication with different values for the lasers' linewidths is evaluated at different OSNR values. It can be observed that the algorithm can meet the required QoS even for values of 500 kHz for the two lasers' linewidths at high OSNRs. As the values of lasers linewidths decrease, the approach performance is improved, reaching values of BER below 10^{-5} for the case where $\delta f_{tx} = \delta f_{rx} = 50$ kHz.

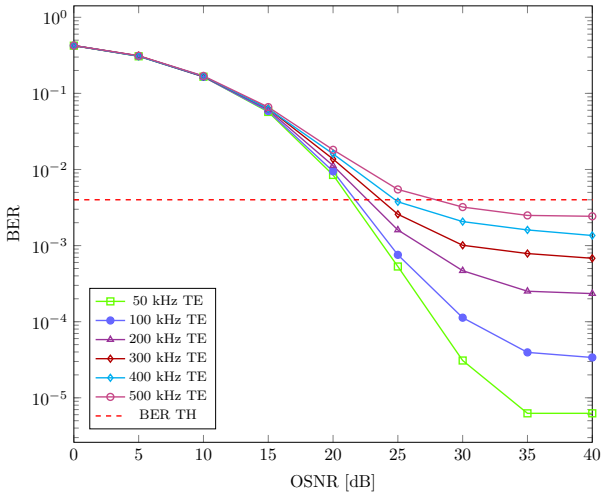

Figure 3.10 – BER evolution for multiple values of OSNR for $N_0 = 100$ with different values of $\delta f_{tx} = \delta f_{rx}$, and $P = 12$ pilot symbols

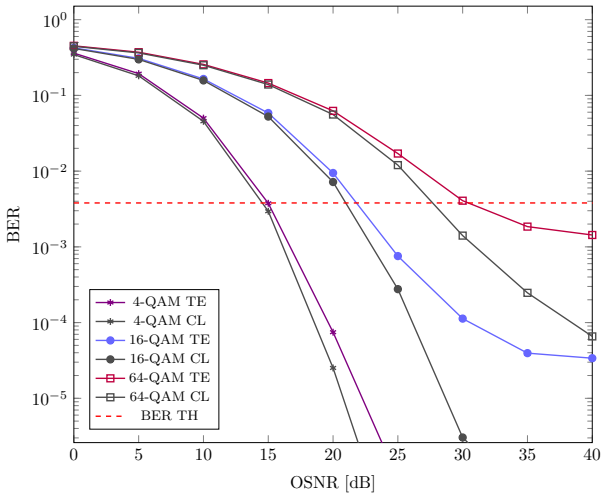

Figure 3.11 – BER evolution for different $\mathcal{M}$-QAM for multiple values of OSNR

Finally, in Figure 3.11, the compensation performance is computed for different $\mathcal{M}$-QAMs and compared to a modified Clairvoyant equalizer [Kay93] that has perfect knowledge about the quasi-static parameters (Dz, ΔF, $\mu_{TX/RX}$, $\nu_{TX/RX}$), and is denoted by "CL". At low OSNR values, the proposed method has similar performance values to the modified Clairvoyant equalizer, but as the OSNR increases, its performance is more degraded. For a 4-QAM, the BER values are below the imposed threshold for OSNRs higher than 15 dB and a 0.5 dB OSNR penalty with respect to the modified Clairvoyant equalizer is observed. In the 16-QAM case, the BER reach the imposed threshold at

approximately 21.8 dB OSNR, by introducing a 0.8 dB OSNR penalty compared to the modified Clairvoyant equalizer. Even for the 64-QAM case, for OSNRs higher than 30.4 dB, the proposed algorithm reaches the imposed threshold while inserting a 2.7 dB OSNR penalty compared to the modified Clairvoyant equalizer.

3.3.1.3 Complexity analysis

After evaluating the proposed algorithm's performance, its computational complexity is analyzed, taking into consideration the number of operations.

The computational complexity is discussed separately for the preamble-based estimation and the tracking and compensation, as the preamble-based estimation is performed only once, while the pilot-based tracking is performed for each data block. Furthermore, for the preamble-based estimation, the analysis can be divided into two parts: the nonlinear and linear parameters estimation. The nonlinear parameters estimation is the most computationally demanding, requiring a grid search over a two-dimensional space and a LM optimization. On the other hand, the linear parameters are estimated by performing a pseudoinverse operation. In Table 3.4, the approximate number of operations for a single iteration can be seen. The computational complexity of the estimation algorithm approaches $\mathcal{O}(N_0^2)$ for $N_0 \to \infty$, with the Jacobian matrix computation being the most demanding step. The convergence of the algorithm was approximated as in [Sto+13]. Initially, the LM algorithm converges linearly, then the order of convergence increases to values between 1 and 2, and at the solution, the convergence returns to a linear evolution. However, all these operations are iteratively performed except for the pseudoinverse computation. For the grid search, 10 candidate values for Dz and 15 for ΔF were used, leading to 150 computations of the cost function. The residual function and the Jacobian matrix require fewer iterations (typically between 5 and 30).

Similarly, the complexity analysis can be divided into two steps: phase tracking and

Table 3.4 – Approximative number of operations needed for the preamble-based estimation algorithm

Computation	**Number of operations**
Grid search	$48N_0^2 + 2N_0 \log N_0 + 70N_0$
Residual function	$80N_0^2 + 2N_0 \log N_0 + 36N_0$
Jacobian matrix	$178N_0^2 + 6N_0 \log N_0 + 35N_0$
Pseudoinverse matrix	$48N_0^2 + 4N_0 \log N_0 + 50N_0$

Table 3.5 – Approximative number of operations needed for the phase tracking and compensation algorithm

Computation	**Number of operations**
Residual function	$4N_b^2 + 12N_b + 2P$
Jacobian matrix	$16N_b^2P + 48N_bP$
ZF Equalizer	$12N_b^3 + 37N_b^2 + 13N_b$

compensation. The lasers' phase estimation is operated using the LM algorithm. The compensation consists of a matrix inversion, while the constellation enforcement is based on the arg min operation. In table 3.5, the approximate number of operations required for a single iteration of each step is shown. It can be seen that the computational complexity of the phase tracking step approaches $\mathcal{O}(N_b^2)$ for $N_b \to \infty$, while the compensation approaches $\mathcal{O}(N_b^3)$ for $N_b \to \infty$, being the most demanding step. Similar to the preamble-based estimation, the LM algorithm starts converging linearly, then the order of convergence increases to values between 1 and 2. At the solution, the convergence returns to a linear evolution. As previously mentioned, the number of iterations has an important impact on the total complexity of the approach. The residual function and the Jacobian matrix are computed iteratively (typically between 5 and 30 iterations), while the inverse of the matrix $\mathbf{M}$ is computed only once.

3.3.2 Comparison to the conventional DSP compensation algorithms

This subsection presents a comparison to the conventional DSP compensation algorithms to further validate the proposed approach. To compare the two techniques, exactly the same local DSP compensation techniques as in 2.7 are considered. The system diagram can be seen in Figure 3.12, while the system parameters are provided in Table 3.6. It is important to notice that, in this case, the number of constant phases is decoupled from the number of pilot symbols. Even if there are 10 pilot symbols used for tracking,

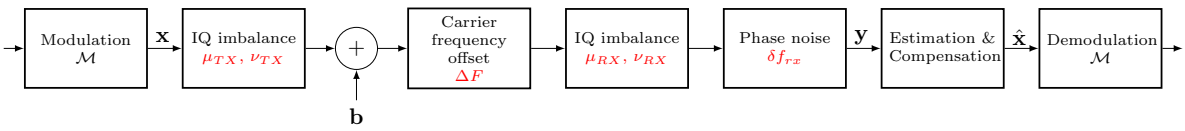

Figure 3.12 – Diagram of the system used for comparison

Table 3.6 – System and imperfections parameters

BW [GHz]	**f_s [GHz]**	**$g_{tx/rx}$ [dB]**	**$\vartheta_{tx/rx}$ [deg.]**	**ΔF [MHz]**	**δf_{rx} [kHz]**	**P [symb.]**	**K[symb.]**
20	20	1	10	200	100	10	100

the laser phase has only 3 constant levels ($K = 100$). This is done to enforce an averaging over the pilot symbols, similar to the one operated by the averaging filter in the case of conventional DSP algorithms.

First, the BER performance comparison is carried out, then a complexity analysis regarding the number of operations is conducted. In Figure 3.13, the BER evolution of the two techniques with respect to OSNR for 4-QAM and 16-QAM is depicted. It can be seen that for 4-QAM, only the "DSP v3" has better performance than the proposed approach at medium to high OSNR values. On the other hand, for the 16-QAM, the global approach proposed has better performance than all local compensation techniques considered for any OSNR value. Moreover, the global approach has better performance at low OSNR values even in the case of 4-QAM. This can be due to the fact that $K = 100$ for the proposed global approach. This reduces the noise impact at low OSNR levels. On the other hand, at high values, it does not reproduce the dynamic of the laser phase very well. Moreover, it is important to notice that the global approach does not use any decision-directed step.

In Table 3.7, the approximate number of operations for the global approach can be

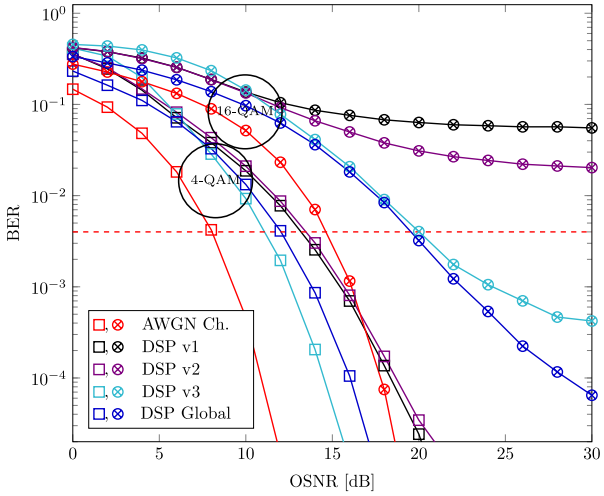

Figure 3.13 – BER evolution of the competing approaches with respect to OSNR for $\mathcal{M}$-QAM communications ($\mathcal{M} = 4$ and $\mathcal{M} = 16$)

Table 3.7 – The approximate number of operations for the global approach for the preamble-based estimation, phase tracking, and compensation

Operation	Residual	Jacobian	Others
Preamble Est.	$36N_0^2$ $+25N_0$	$16N_0^2$+$41N_0$+N_0/K($40N_0^2$+$24N_0$)	$16N_0^2$+$40N_0$
Track. & Comp.	$4N_b^2$ $+4N_b$	N_b/K($4N_b^2$ + $4N_b$)	$8N_b^3$+$4N_b^2$+$20N_b$

Table 3.8 – The approximate number of operations for the local approach in the case "DSP v3" scenario

Impairment	Estimation and compensation
RX IQ imbalance	$7N_b$
CFO	$7N_b$ + $5N_0$
Laser PN	$24N_b + 4P(2 + P * N_{avg} + N_b * N_{avg})$
TX IQ imbalance	$4N_b + 4N_{taps} * N_b$

seen. This is divided into two parts corresponding to the preamble-based estimation and phase tracking and compensation. It can be seen that for the preamble-based estimation, the complexity approaches $\mathcal{O}(N_0^2)$, while for the compensation, the complexity approaches $\mathcal{O}(N_b^3)$.

In Table 3.8, the number of operations performed by the local DSP approach after the training of the filter used for transmitter IQ imbalance can be seen. The terms N_{avg} and N_{taps} denote the length of the averaging filter and the number of filter taps, respectively. It can be noted that its complexity approaches $\mathcal{O}(N_b)$. Based on that, it can be concluded that the computational complexity of the global DSP approach is higher than that of the local DSP technique. However, the global approach does not perform any decision-directed step, which is an advantage from the computational time point of view.

3.3.3 Experimental demonstration

In this subsection, an experimental demonstration in a simplified back-to-back setup is performed to further validate the approach's effectiveness. The system is impaired only by the transmitter IQ imbalance and laser PN. In this case, a polynomial model of the laser phase is employed for the phase tracking. The parameters estimation can be expressed as follows:

$$\{\hat{\boldsymbol{\phi}}, \hat{\boldsymbol{\chi}}_{TX}\} = \arg\min_{\boldsymbol{\phi}, \boldsymbol{\chi}_{TX}} \|\mathbf{Py} - \mathbf{PA}(\boldsymbol{\phi})\boldsymbol{\chi}_{TX}\|^2, \tag{3.46}$$

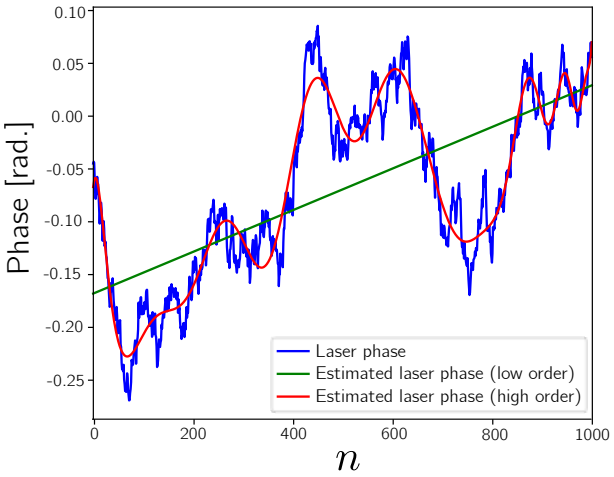

Figure 3.14 – Laser phase estimation using different polynomial orders

where $\boldsymbol{\chi}_{TX} = \begin{bmatrix} \mu_{TX} & \nu_{TX} \end{bmatrix}^T$. When using the polynomial phase model, the polynomial order should be set carefully. A low order may lead to a poor estimation of the laser phase because the dynamics of the phase cannot be accurately described. On the contrary, a high order may be more impacted by the additive noise and can also produce undesirable results, as overfitting is more prone to occur. An exemplification of these two situations can be seen in Figure 3.14. To overcome this difficulty, an L0-Norm Penalized LS estimation is proposed to correctly select the polynomial order [Sto+04] as follows:

$$\{\hat{\boldsymbol{\phi}}, \hat{\boldsymbol{\chi}}_{TX}\} = \arg \min_{\boldsymbol{\phi}, \boldsymbol{\chi}_{TX}} \|\mathbf{Py} - \mathbf{PA}(\boldsymbol{\phi})\boldsymbol{\chi}_{TX}\|^2 + \lambda \|\boldsymbol{\phi}\|_0, \tag{3.47}$$

where λ is the shrinkage controlling factor. The system model depends only on the IQ imbalance linear parameters and the laser phase nonlinear parameters. Considering this, during the preamble-based estimation, only a computation of a pseudoinverse matrix is required to estimate the transmitter IQ imbalance parameters. During the tracking stage, the laser phase estimation is also operated using the LM optimization algorithm by initializing the laser phase instances with 0s.

Figure 3.15 depicts the experimental setup used for this validation. The user's binary sequence is modulated into a 4-QAM configuration having a bandwidth of 8 GHz. The symbols are sent into the Keysight M8195A Arbitrary Waveform Generator (AWG). The signal is upsampled at a rate of 32 GSa/s using DACs with 8 bits resolution. Then, it is converted to the optical domain by an MXIQER-LN-30 optical modulator with a V_π of 5.4 V and a Keysight N4391A Optical Modulation Analyzer (OMA) local oscillator

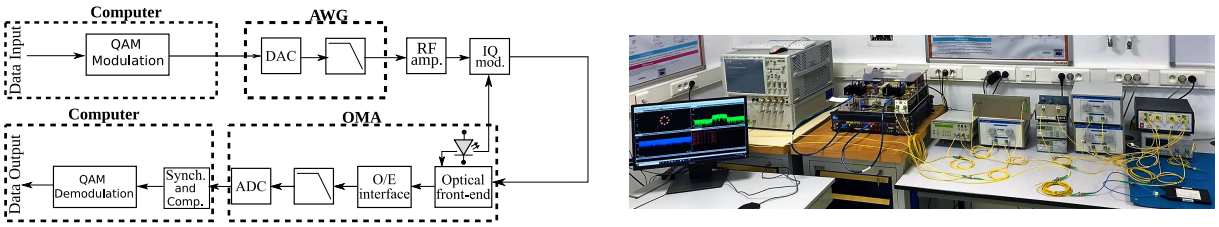

Figure 3.15 – QAM coherent optical experimental setup. AWG: Arbitrary Waveform Generator, OMA: Optical Modulation Analyzer

operating at 1540 nm with a laser linewidth of 100 kHz. The IQ modulator's operating point is stabilized via the MBC-IQ-LAB-A1 bias controller. On the receiver side, the OMA converts the signal back into the electrical domain using the 40 GSa/s ADC with 8 bits resolution. Finally, the signal goes through synchronization, impairments compensation, and demodulation.

Four thousand 4-QAM symbols were used to evaluate the technique's performance. Among these, 100 are used as a preamble, and the rest is divided into data blocks of a length of 300. Each data block contains 12 4-QAM pilot symbols. The preamble and the pilot symbols are known on the receiver side. The laser PN is related to a single laser having a linewidth of 100 kHz, while for IQ imbalance, 1 dB amplitude gain difference and multiple phase deviations between 5° and 20° were inserted using software operations.

In Figure 3.16, the constellations obtained after synchronization, then after the compensation, and the estimated laser phase for the case where the $\vartheta = 10°$ is depicted. It can be observed that the constellation after the synchronization is highly impaired by the transmitter IQ imbalance, laser PN, and noise. Then, after the compensation, the IQ

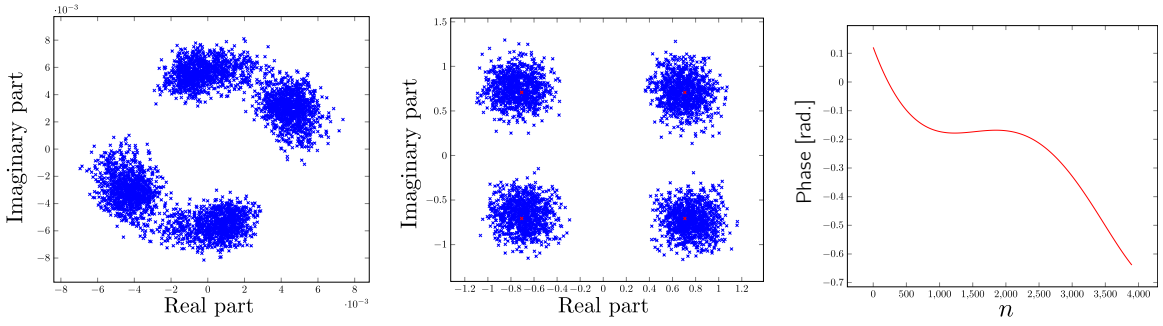

(a) Constellation after the synchronization

(b) Constellation after the compensation

(c) Estimated laser phase

Figure 3.16 – Signal constellations after synchronization and compensation, and the estimated laser phase for the case where $\vartheta = 10°$

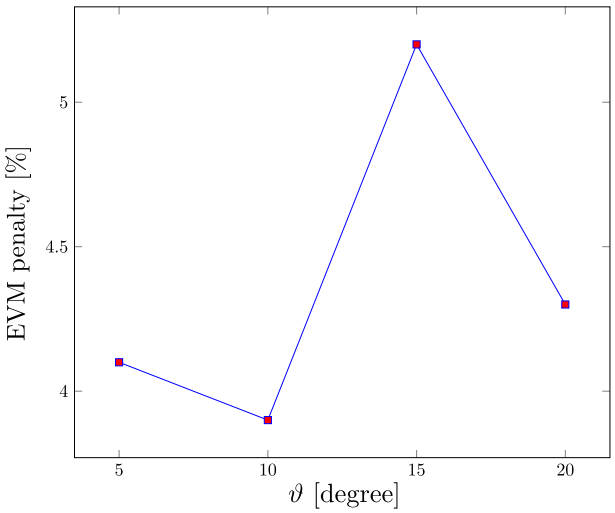

Figure 3.17 – EVM penalty for $g = 1$ dB against phase imbalance (ϑ) with respect to the case where no IQ imbalance occurs

imbalance and laser PN is mitigated, the corresponding EVM value being 21.7%. The estimated laser phase is depicted in 3.16c. In this case, the polynomial order selected by the algorithm is 5.

Finally, in Figure 3.17, the EVM penalty for different values of ϑ between $[5°, 20°]$ with respect to the case where no IQ imbalance is present is depicted. It can be seen that the maximum EVM penalty is 5.2%, denoting good robustness of the algorithm.

3.4 Conclusion and discussion

This chapter proposed a global DSP approach based on statistical signal processing. The proposed method globally estimates and compensates for multiple imperfections like laser PN, IQ imbalance, CD, and CFO in a SP coherent optical system. The estimation is split into two parts: a static impairments estimation using a preamble and a laser phase tracking over the data blocks using pilot symbols. Both techniques are based on NLS estimation. The compensation is performed using ZF equalizer. By performing a global estimation, the proposed technique avoids the difficulties associated with the use of cascaded local DSP approaches.

The technique's performance was evaluated using numerical simulation and an experimental demonstration. Moreover, a comparison to some local DSP compensation techniques was operated. The proposed method proved to have good estimation perfor-

mance as a reduced performance gap is introduced compared to the CRLB. In addition, the proposed method reaches a good QoS, and its compensation penalty is relatively reduced compared to a modified Clairvoyant equalizer. Furthermore, the method proved to work efficiently in a simplified experimental setup. Compared to the conventional local DSP approaches, the proposed method has better performance at low OSNR values for 4-QAM and outperforms it in the case of 16-QAM.

Despite the clear advantages of the proposed global approach, there are some drawbacks. First, the computational complexity is increased compared to the conventional compensation approach. This could be a problem in implementing the method in real-time communications. Another drawback is a typical one for the model-based approaches. The approach is sensitive to model mismatches and is difficult to adapt to new scenarios or in the presence of additional impairments.

Chapter 4

Global compensation of the linear imperfections using a parametric network

In the previous chapters, the compensation of linear impairments in coherent optical systems was investigated using two distinct DSP approaches: a conventional approach that consists in cascading multiple DSP compensation algorithms, and an original DSP approach that estimates and compensates for all the considered impairments globally. It was illustrated that the global approach outperforms the conventional DSP approach for the considered scenario. However, the proposed parametric DSP approach has limited flexibility since its application to a new channel model implies new specific mathematical developments. To overcome this limitation of the DSP approach, several authors investigated the use of ML/DL for the compensation of communication chains. Unlike DSP techniques, ML/DL networks have the distinct advantage of being universal approximators since they can approximate a large class of functions. The use of conventional networks to compensate optical communication chains has been investigated in [Fre+20; Gai+20; Sha+22; Zib+15]. However, despite their flexibility, conventional networks generally require a large dataset for training, and their computational complexity may be prohibitive [Fre+21]. Furthermore, conventional networks are not well adapted to the dynamic nature of communication channels since the tracking of time-varying channel parameters may require periodic retraining [Rav+22].

To overcome the limitations of ML/DL techniques in communications applications, several authors have proposed to use model-based ML/DL networks [Osh+17]. In optical communications, most studies focus on using a particular model-based ML/DL approach, called Learned Digital Back-propagation (LDBP), for the compensation of fiber nonlinearity [Bit+20a; Bit+20b; Fan+21; Häg+20a; Lin+22; Lin+21]. In the presence of time-varying impairments, the LDBP approach is usually associated with cascaded lo-

cal DSP algorithms [Bit+20a; Bit+20b; Fan+21; Oli+20]. Unfortunately, this strategy usually requires complicated training strategies and is also inherently impacted by the suboptimality of the cascaded DSP approach.

In this chapter, we propose a new model-based ML/DL network for the global compensation of static and time-varying impairments. As opposed to other model-based techniques, the proposed network is composed of multiple parametric layers, where each layer allows the compensation of a specific impairment. As opposed to the conventional ML/DL technique, the proposed model-based multi-layer parametric networks can track the time-variant impairments with a small number of training samples. Furthermore, as opposed to the global DSP approach presented in Chapter 3, the proposed compensation network is more general since it inherits the extreme flexibility of multi-layer networks allowing the compensation in a wide range of communication chains.

This chapter is organized as follows. A generic parametric multi-layer system model is introduced in section 4.1. Then, in section 4.2, a particular DP coherent optical system model is analyzed. Finally, in section 4.3, the results obtained by numerical simulations and experimental investigation are discussed.

4.1 A Parametric Multi-Layer Compensation Network

4.1.1 Multi-Layer Linear SISO Signal Model

For the sake of presentation, let us consider first a SISO signal model where multiple imperfections occur and introduce $\mathbf{x}$ the input data vector defined by:

$$\mathbf{x} = [x[0], \ldots, x[N-1]]^T, \tag{4.1}$$

where N is the length of the data vector. The input signal contains symbols from a discrete alphabet $\mathbb{S}$ composed of $|\mathbb{S}|$ complex elements (e.g. Phase Shift Keying (PSK), QAM). During transmission, the signal is impaired by multiple hardware and channel imperfections. In Figure 4.1, a generic communication chain impaired by L impairments is depicted, where $\mathbf{y}$ is the received signal. In this figure, the communication chain is modeled as a multi-layer network. Regarding the noise component, its contribution is usually distributed along the communication chain. However, in this chapter, we neglect

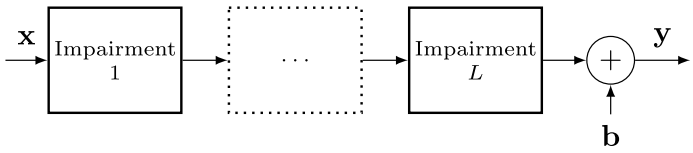

Figure 4.1 – Communication chain with multiple impairments

the impact of the impairment layers on the noise distribution for ease of simplicity. Using this approximation, the noise is modeled as an additive component which is placed after the last considered impairment.

4.1.1.1 Parametric Linear Layers

In the following, we assume that each layer can be described by a parametric linear transformation. Under this assumption, the layer input-output relationship can be modeled by:

$$\tilde{\mathbf{x}}_{l+1} = \mathbf{F}_l(\boldsymbol{\alpha}_l)\tilde{\mathbf{x}}_l, \tag{4.2}$$

where the tilde denotes the real-valued augmented version of the original signals, $\mathbf{x}_l$ and $\mathbf{x}_{l+1}$ are the signals before and after the $l-th$ impairment layer, respectively. The forward matrix $\mathbf{F}_l(\boldsymbol{\alpha}_l)$ is called the transfer matrix of the layer. This matrix depends on a vector parameter $\boldsymbol{\alpha}_l$.

Let us denote by $\boldsymbol{\alpha}_l[m]$ the vector parameter for the $m-th$ transmitted block of the signal. Regarding this vector, we can distinguish two cases:

— Static vector parameter: $\boldsymbol{\alpha}_l[m] = \boldsymbol{\alpha}_l$ for all block index m,

— Time-varying parameter: $\boldsymbol{\alpha}_l[m]$ can vary with the block index m.

4.1.1.2 Multi-Layer Model

At the receiver side, the resulting signal impaired by all the imperfections can be expressed as follows:

$$\tilde{\mathbf{y}} = \mathbf{F}(\boldsymbol{\alpha})\tilde{\mathbf{x}} + \tilde{\mathbf{b}}, \tag{4.3}$$

with $\mathbf{y}$ the received signal, and

$$\mathbf{F}(\boldsymbol{\alpha}) = \mathbf{F}_L(\boldsymbol{\alpha}_L) \times \ldots \times \mathbf{F}_1(\boldsymbol{\alpha}_1), \tag{4.4}$$

where $\boldsymbol{\alpha} = \left[\boldsymbol{\alpha}_1^T, \ldots, \boldsymbol{\alpha}_L^T\right]^T$ is a column vector containing the real-valued system's parameters, and $\tilde{\mathbf{b}}$ corresponds to the AWGN contribution.

4.1.2 Compensation Network Architecture

On the receiver side, the objective is to recover the transmitted data $\mathbf{x}$ from the received one $\mathbf{y}$. Mathematically, under Gaussian additive noise and assuming independent and identically distributed symbols, the detection problem can be solved by minimizing the following LS cost function as follows:

$$\{\hat{\boldsymbol{\alpha}}, \mathbf{x}_{det}\} = \arg \min_{\boldsymbol{\alpha}, \mathbf{x} \in \mathbb{S}^N} \|\tilde{\mathbf{y}} - \mathbf{F}(\boldsymbol{\alpha})\tilde{\mathbf{x}}\|_2^2. \tag{4.5}$$

To address this detection problem, we propose using a ZF MIMO detector for simplicity. This subsection shows that the ZF MIMO detector can be implemented using a simple compensation network.

4.1.2.1 Zero-Forcing Detection

As detailed in chapters 2 and 3, the ZF detection is split in two steps: compensation and hard detection. For the proposed multi-layer model, the implementation of the ZF detector also exhibits a multi-layer structure. Indeed, under the assumption that the matrix $\mathbf{F}(\boldsymbol{\alpha})$ is invertible, $\mathbf{F}^{-1}(\boldsymbol{\alpha})$ can be decomposed as follows:

$$\mathbf{F}^{-1}(\boldsymbol{\alpha}) = \mathbf{F}_1^{-1}(\boldsymbol{\alpha}_1) \times \ldots \times \mathbf{F}_L^{-1}(\boldsymbol{\alpha}_L). \tag{4.6}$$

Note that the decomposition of the inverse matrix leads to L matrix inversion instead of one inversion, thus increasing the computation complexity. Nevertheless, many transfer matrices encountered in communication systems exhibit a particular property that allows for avoiding any direct matrix inversion.

4.1.2.2 Isomorphic Layers

Many transfer matrices encountered in communication systems exhibit a particular property presented in this subsection: the isomorphic property. An isomorphic transfer matrix respects the following equality:

$$\mathbf{F}_l^{-1}(\boldsymbol{\alpha}_l) = \mathbf{F}_l(\boldsymbol{\beta}_l). \tag{4.7}$$

In other terms, compensating an isomorphic parametric layer can be achieved by applying the same parametric layer with a new set of parameters $\boldsymbol{\beta}_l$. For example, compensating a CFO impairment with parameter $\alpha = \omega_0$ can be obtained by applying a CFO impairment with parameter $\beta = -\omega_0$. By assuming L isomorphic layers in (4.8), the matrix $\mathbf{F}^{-1}(\boldsymbol{\alpha})$ can be expressed as:

$$\mathbf{F}^{-1}(\boldsymbol{\alpha}) = \mathbf{B}(\boldsymbol{\beta}) = \mathbf{F}_1(\boldsymbol{\beta}_1) \times \ldots \times \mathbf{F}_L(\boldsymbol{\beta}_L), \tag{4.8}$$

where $\boldsymbol{\beta}$ is a vector containing all the compensation parameters. As observed, the isomorphic property avoids any direct matrix inversion.

4.1.2.3 Network Architecture

Assuming L isomorphic layers, the decomposition of $\mathbf{F}^{-1}(\boldsymbol{\alpha})$ in (4.8) shows that the ZF impairment compensation can be implemented using a parametric multi-layer network. This proposed parametric network is presented in Figure 4.2. In this compensation network, each layer reverses the effect of one particular impairment. Mathematically, the

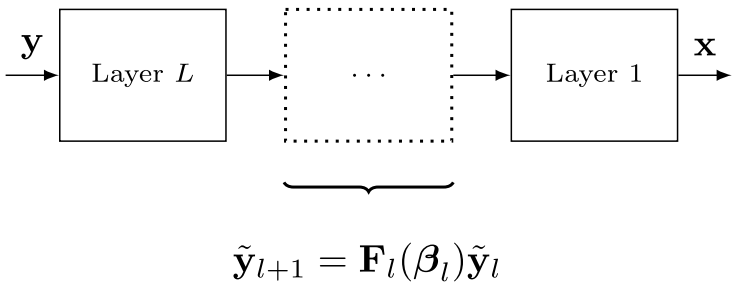

Figure 4.2 – Proposed multi-layer parametric network depending on the parameter $\boldsymbol{\beta} = \{\boldsymbol{\beta}_1, \cdots, \boldsymbol{\beta}_L\}$)

output of the $l-th$ compensation layer is given by:

$$\tilde{\mathbf{y}}_{l+1} = \mathbf{F}_l(\boldsymbol{\beta}_l)\tilde{\mathbf{y}}_l, \tag{4.9}$$

where $\mathbf{y}_l$ and $\mathbf{y}_{l+1}$ are the signals before and after the compensation, respectively, $\mathbf{F}_l(\boldsymbol{\beta}_l)$ is the real-valued transfer matrix of the layer, and $\boldsymbol{\beta}_l$ is the compensation vector parameter.

4.1.2.4 Extension to MIMO Communications

The MIMO systems increase the capacity of a communication system by transmitting and receiving simultaneously multiple signals over the same channel. The proposed approach is not limited to SISO scenarios and can be relatively easily extended to a MIMO setup when the number of inputs is equal to the number of outputs.

First, the signals are stacked as follows:

$$\mathbf{x} = \begin{bmatrix} \mathbf{x}_0^T & \mathbf{x}_1^T & \cdots & \mathbf{x}_{M-1}^T \end{bmatrix}^T, \tag{4.10}$$

where M denotes the number of signals composing the MIMO frame. Secondly, the transfer matrix may be obtained in different ways, according to the imperfections characteristics. For example, the impairments in a MIMO system may have a similar, different, or coupled effect on each composing signal. Based on that, the compensation matrix of each layer can be constructed as detailed in Table 4.1, where the first index of $\boldsymbol{\beta}$ refers to the $l-th$ compensation layer and the second to the particular $i-th$ signal composing the MIMO frame.

4.1.3 Network training

The compensation network in Figure 4.2 depends on the vector parameter $\boldsymbol{\beta}$. In practice, this vector is unknown and must be estimated during the training stage. Mathematically, the objective of the training stage is to minimize a cost function (metric), such as the network outputs being close to some target symbols. Motivated by the application of the ZF technique, we propose to use the following cost function:

$$\hat{\boldsymbol{\beta}} = \arg\min_{\boldsymbol{\beta}} \|\tilde{\mathbf{x}}_{target} - \mathbf{B}(\boldsymbol{\beta})\tilde{\mathbf{y}}\|_2^2, \tag{4.11}$$

Table 4.1 – The compensation transfer matrix of $l-th$ layer depending on the impairments effect in MIMO systems

Effect classification	**Compensation matrix**	**Parameters to be estimated**
Similar	$\mathbf{F}(\boldsymbol{\beta}_l) = \begin{bmatrix} \mathbf{F}(\boldsymbol{\beta}_{l,0}) & 0 & \dots & 0 \\ 0 & \mathbf{F}(\boldsymbol{\beta}_{l,0}) & \dots & 0 \\ \vdots & & \ddots & \vdots \\ 0 & 0 & \dots & \mathbf{F}(\boldsymbol{\beta}_{l,0}) \end{bmatrix}$	$\boldsymbol{\beta}_{l,0}$
Different	$\mathbf{F}(\boldsymbol{\beta}_l) = \begin{bmatrix} \mathbf{F}(\boldsymbol{\beta}_{l,0}) & 0 & \dots & 0 \\ 0 & \mathbf{F}(\boldsymbol{\beta}_{l,1}) & \dots & 0 \\ \vdots & & \ddots & \vdots \\ 0 & 0 & \dots & \mathbf{F}(\boldsymbol{\beta}_{l,M-1}) \end{bmatrix}$	$\left[\boldsymbol{\beta}_{l,0}, \cdots, \boldsymbol{\beta}_{l,M-1}\right]^T$
Coupled	$\mathbf{F}(\boldsymbol{\beta}_l)$	$\boldsymbol{\beta}_l$

where $\tilde{\mathbf{x}}_{target}$ and $\mathbf{B}(\boldsymbol{\beta})\tilde{\mathbf{y}}$ are the target (desired output of the network) and the actual output of the network.

As static and time-variant effects impair the signals, the same data frame structure used in chapters 2 and 3 is employed. The data frame consists of a preamble and multiple pilot symbols inserted periodically into the data frame, as shown in Figure 4.3. The preamble and pilots are known on the receiver side, and consist of random symbols from the constellation set $\mathbb{S}$. The preamble, made of N_0 symbols, is denoted by $\mathbf{x}_0$ and is used for the global estimation of all systems parameters, while the P pilot symbols are denoted

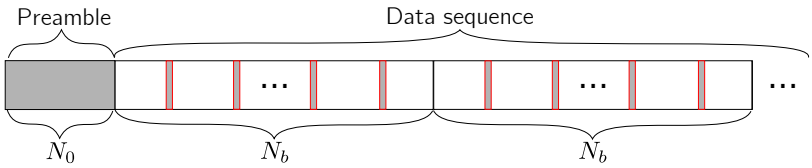

Figure 4.3 – Data frame structure consisting of a preamble and multiple pilot symbols inserted periodically

by $\mathbf{x}_1$ and are used for time-variant imperfections tracking.

Based on the frame structure, the training is split into three parts:

— *Preamble-based training*: First, a preamble-based training that aims to estimate all compensation parameters $\boldsymbol{\beta}$ is operated. The following equation describes this training step:

$$\hat{\boldsymbol{\beta}} = \arg\min_{\boldsymbol{\beta}} \|\tilde{\mathbf{x}}_0 - \mathbf{P}_0\mathbf{B}(\boldsymbol{\beta})\tilde{\mathbf{y}}\|_2^2, \tag{4.12}$$

where $\mathbf{x}_0$ represent the transmitted block, and $\mathbf{P}_0$ is set up as a preamble extraction matrix;

— *Pilot-based training*: Secondly, pilot-based training is operated to re-estimate the time-variant parameters. It is also supervised training. The following equation describes this training step:

$$\hat{\boldsymbol{\beta}} = \arg\min_{\boldsymbol{\beta}} \|\tilde{\mathbf{x}}_1 - \mathbf{P}_1\mathbf{B}(\boldsymbol{\beta})\tilde{\mathbf{y}}\|_2^2, \tag{4.13}$$

where $\mathbf{x}_1$ represents the transmitted pilots, and $\mathbf{P}_1$ is set up as a pilot extraction matrix. During this step, overfitting may occur because the numbers of parameters to be estimated and the training symbols have relatively close values.
An original technique is proposed to reduce the overfitting probability and establish the number of required iterations during this step. The data at the output of the network is periodically detected. Then the cost function from (4.11) is computed using as target $\tilde{\mathbf{x}}_{target} = \tilde{\mathbf{x}}_{det}$ and $\mathbf{B}(\boldsymbol{\beta})\tilde{\mathbf{y}}$ as output, where $\mathbf{x}_{det}$ is the detected signal. If the value of the cost function (denoted in the following "detection error") stops decreasing with the number of iterations, the training is stopped, as overfitting probably occurs;

— *Self-labeling training*: This step exploits the constellation knowledge to avoid overfitting and perform a better estimation of the time-variant parameters. The compensated signal after the pilot-based training is detected and used as a target. It can be seen as a DD-LMS [Wid+77], where the main difference is that the update is performed by block, not by sample. The following equation describes this training step:

$$\hat{\boldsymbol{\beta}} = \arg\min_{\boldsymbol{\beta}} \|\tilde{\mathbf{x}}_{det} - \mathbf{B}(\boldsymbol{\beta})\tilde{\mathbf{y}}\|_2^2; \tag{4.14}$$

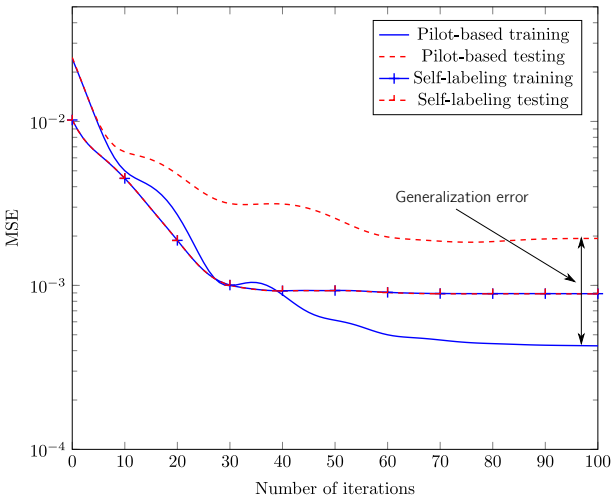

Figure 4.4 – Evolution of MSE with the number of iterations during the pilot-based and self-labeling training and testing

To better illustrate the benefit of using a self-labeling step, in Figure 4.4 the MSE with the number of iterations during the pilot-based and self-labeling training and testing for a 16-QAM setup with an OSNR of 30 dB is depicted. Each data block contains 300 symbols, of which 10 are pilot symbols. It can be seen that the generalization error for the pilot-based step is relatively high. In contrast, for the self-labeling step, the generalization error is largely reduced, the training and testing curves being almost identical. This can be because the noise may impact the pilot symbols differently than the testing symbols. On the other hand, during the self-labeling training, the noise contribution is averaged on multiple training symbols, so a more accurate estimation of the parameters is generally obtained.

4.1.4 Comparison with conventional Neural Networks

As a state of comparison, Figure 4.5 presents the architecture of a Multi-layer Perceptron (MLP) network and proposed network parametric network. It can be seen that the MLP network is parametrized by the matrices $\mathbf{H}_l$ denoting a linear transformation and the bias vectors $\mathbf{b}_l$, while the proposed parametric network only by the vector $\boldsymbol{\beta}$.

Both network architectures have multiple layers and can be implemented using DL frameworks (e.g., PyTorch, TensorFlow, etc.). In addition, the training is relatively similar, being based on the backpropagation with the Gradient Descent-based optimization. Furthermore, both architectures can be easily modified and updated based on the scenario

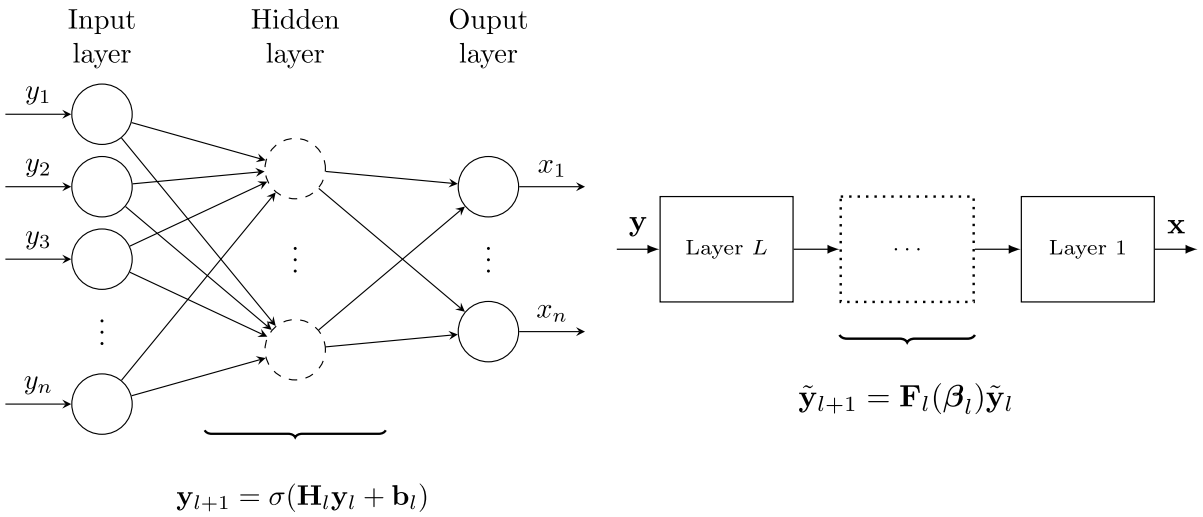

(a) MLP network (learned parameters: $\boldsymbol{\beta} = \{\mathbf{H}_1, \cdots, \mathbf{H}_L, \mathbf{b}_1, \cdots, \mathbf{b}_L\}$), $\sigma(.)$: activation function

(b) Proposed multi-layer parametric network (learned parameters: $\boldsymbol{\beta} = \{\boldsymbol{\beta}_1, \cdots, \boldsymbol{\beta}_L\}$)

Figure 4.5 – Comparison between an MLP network and the proposed multi-layer parametric network

considered.

The MLP uses nonlinear activation functions allowing the modeling of nonlinear transformations. On the contrary, the proposed parametric contains only linear layers and cannot model nonlinear transformations. Compared to conventional networks, the layers of the proposed parametric network benefit from the knowledge of the imperfections model. It follows that the training stage can be performed using a smaller dataset consisting of only a few symbols. The MLP networks use dataset segmentation, as generally, independent parts of the dataset are used for training, validation, and testing. On the other hand, as the parametric network has to periodically perform the training, the validation dataset may be excluded. Moreover, by having just a few parameters to estimate, the computational complexity of the training stage is drastically reduced compared to the MLP. Furthermore, different from the MLP, most of the layers of the parametric network can be implemented using scalar operations which substantially reduces the overall computational complexity of the parametric network.

4.2 A Parametric Network for DP Coherent Optical System with Multiple Impairments

4.2.1 System Architecture

A DP coherent optical system can been as a particular 2×2 MIMO communication, where $p \in \{X, Y\}$ denotes the two polarizations. Such a system impaired by laser PN and IQ imbalance, both on transmitter and receiver sides, CD, PMD, and CFO is depicted in Figure 4.6.

The signal model and classifications regarding the time evolution and the impact on each polarization are provided in Chapter 2 for each impairment.

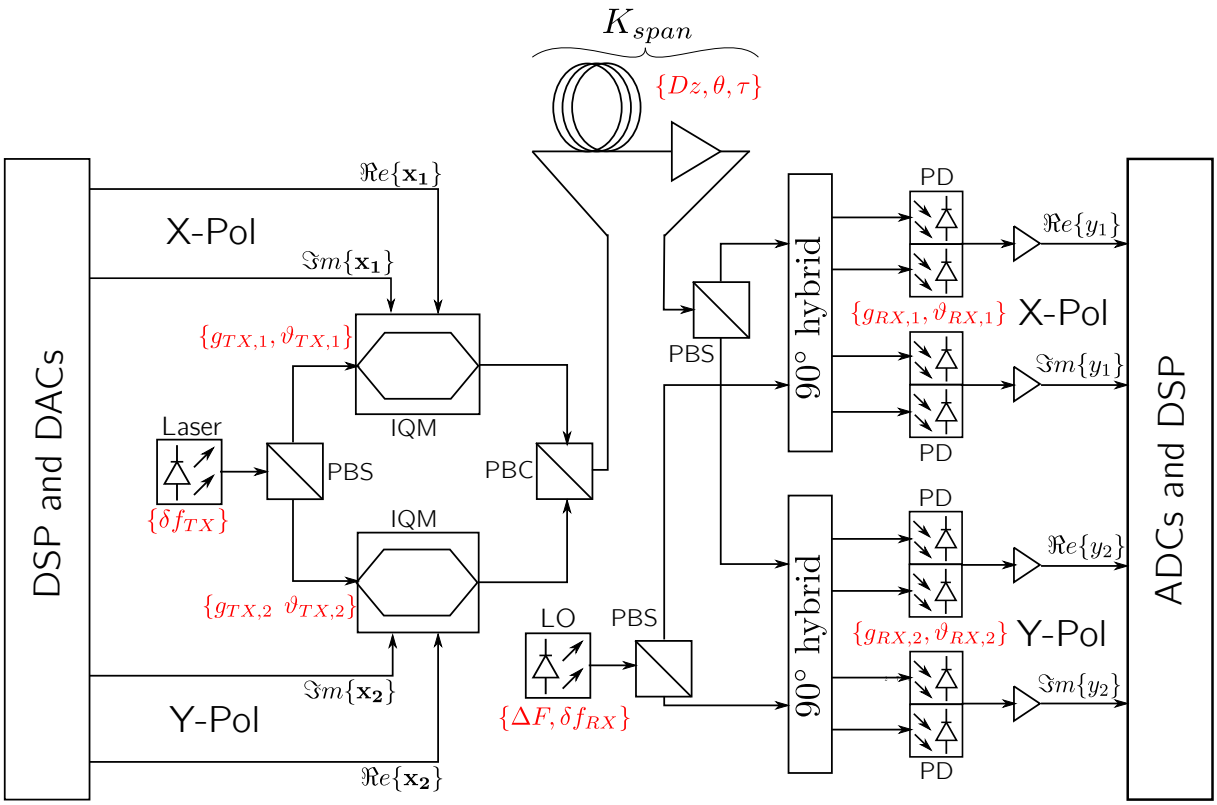

Figure 4.6 – DP coherent optical system under the impact of laser PN, IQ imbalance, CD, PMD, and CFO

4.2.2 Compensation Network

The block diagram of the multi-layer system of interest is depicted in Figure 4.7. The data is modulated, then the signal is upsampled and filtered by an RRC. Then the resulting signal undergoes multiple hardware and channel imperfections described by the vector parameter $\boldsymbol{\alpha}$, whose elements are marked in red. On the receiver side, the impact of the impairments is compensated for by the parametric network, and the transmitted data is recovered after demodulation.

4.2.3 Network Layers

In the following, the proposed network's compensation layers are detailed, and it will be demonstrated that all of them are isomorphic. Similarly to the implementation, a scalar model will be provided for all the layers, except the one compensating for PMD. It is important to notice that the compensation layers should be reversely ordered with respect to the impairments layers.

4.2.3.1 Laser PN compensation layer

For the laser phase, we consider a common phase model where the laser phase is assumed to be constant over K consecutive symbols. The evolution of the laser phase is then described by the parameter $\boldsymbol{\alpha}_1 = \boldsymbol{\phi}$ that contains N_b/K constant levels.

The output of a laser phase PN impairment layer can be expressed as follows:

$$y_{p,l}[n] = x_{p,l+1}[n] = x_{p,l}[n]e^{j\alpha_1[\lfloor n/K \rfloor]}, \tag{4.15}$$

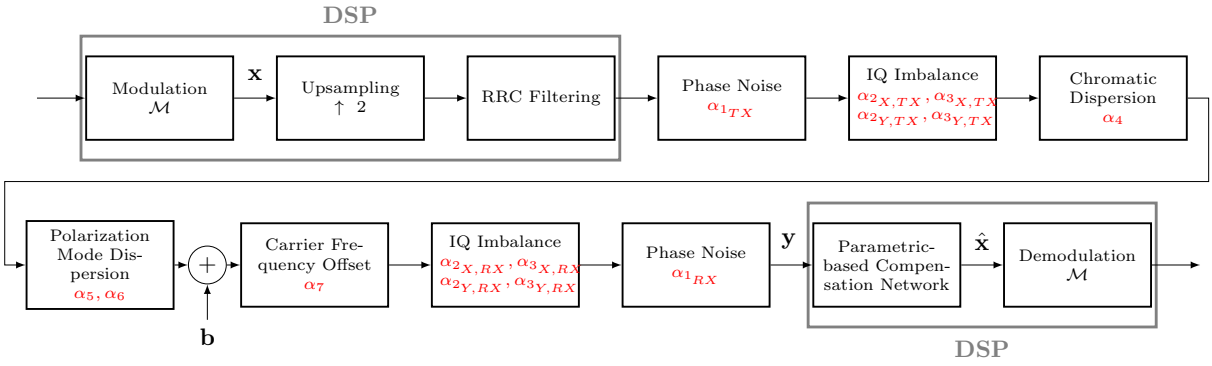

Figure 4.7 – Block diagram of the multi-layer system of interest

where $x_{p,l}$ and $x_{p,l+1}$ are the signals corresponding to a single polarization before and after being impaired, respectively, $\boldsymbol{\alpha}_1$ is the vector of laser phase and $\lfloor . \rfloor$ represents the integer part.

Proposition 1. *The common phase layer is isomorphic.*

Proof. It can be checked that a common laser phase layer depending on the parameter $\alpha_1[m]$ can be compensated by applying a laser phase layer with the parameter $\beta_1[m] = -\alpha_1[m]$. Indeed, the compensated signal can be obtained as:

$$y_{p,l+1} = y_{p,l}[n]e^{j\beta_1[\lfloor n/K \rfloor]} = x_{p,l}[n]e^{j\alpha_1[\lfloor n/K \rfloor]}e^{-j\alpha_1[\lfloor n/K \rfloor]} = x_{p,l}[n]. \tag{4.16}$$

□

4.2.3.2 IQ imbalance compensation layer

The IQ imbalance impairment layer is modeled using the complex parameters $\alpha_2 = \mu$ and $\alpha_3 = \nu$. The impaired complex signal at the output of the layer can be expressed as:

$$y_{p,l} = x_{p,l+1}[n] = \alpha_{2,p}x_{p,l}[n] + \alpha_{3,p}x^*_{p,l}[n]. \tag{4.17}$$

Proposition 2. *The IQ imbalance layer is isomorphic.*

Proof. It can be checked that by setting:

$$\beta_{2,p} = \frac{\alpha^*_{2,p}}{|\alpha_{2,p}|^2 - |\alpha_{3,p}|^2}, \tag{4.18a}$$

$$\beta_{3,p} = \frac{-\alpha_{3,p}}{|\alpha_{2,p}|^2 - |\alpha_{3,p}|^2}, \tag{4.18b}$$

the IQ imbalance can be perfectly compensated for. Indeed, the resulting compensated signal is expressed as:

$$\begin{aligned} y_{p,l+1} &= \beta_{2,p}y_{p,l} + \beta_{3,p}y^*_{p,l} = \beta_{2,p}(\alpha_{2,p}x_{p,l}[n] + \alpha_{3,p}x^*_{p,l}[n]) + \beta_{3,p}(\alpha^*_{2,p}x^*_{p,l}[n] + \alpha^*_{3,p}x_{p,l}[n]) \\ &= x_{p,l}[n]. \end{aligned} \tag{4.19}$$

□

4.2.3.3 CFO compensation layer

The CFO impact can be parametrized by a parameter $\alpha_7 = \Delta F$. The impaired complex signal at the output of the CFO layer is obtained as:

$$y_{p,l} = x_{p,l+1}[n] = x_{p,l}[n]e^{j2\pi n\alpha_7 T_{symb}}. \tag{4.20}$$

Proposition 3. *The CFO layer is isomorphic.*

Proof. It can be checked that by setting $\beta_4 = -\alpha_7$, the CFO can be perfectly compensated for. By this, the signal at the output of the compensation layer is obtained as follows:

$$y_{p,l+1} = y_{p,l}[n]e^{j2\pi n\beta_4 T_{symb}} = x_{p,l}[n]e^{j2\pi n\alpha_7 T_{symb}}e^{-j2\pi n\alpha_7 T_{symb}} = x_{p,l}[n]. \tag{4.21}$$

□

4.2.3.4 PMD compensation layer

PMD impact is described by two parameters: $\alpha_5 = \theta$ and $\alpha_6 = \tau$. The impaired complex signal at the output of the layer is obtained as follows:

$$\begin{bmatrix} y_{X,l}[n] \\ x_{Y,l}[n] \end{bmatrix} = \begin{bmatrix} x_{X,l+1}[n] \\ x_{Y,l+1}[n] \end{bmatrix} = \mathcal{F}^{-1}\left(\begin{bmatrix} \cos(\alpha_5) & -\sin(\alpha_5) \\ \sin(\alpha_5) & \cos(\alpha_5) \end{bmatrix}\begin{bmatrix} e^{j\omega\alpha_6/2} & 0 \\ 0 & e^{-j\omega\alpha_6/2} \end{bmatrix}\right.$$
$$\left.\begin{bmatrix} \cos(\alpha_5) & \sin(\alpha_5) \\ -\sin(\alpha_5) & \cos(\alpha_5) \end{bmatrix}\mathcal{F}\left(\begin{bmatrix} x_{X,l}[n] \\ x_{Y,l}[n] \end{bmatrix}\right)\right). \tag{4.22}$$

Proposition 4. *The PMD layer is isomorphic.*

Proof. It can be verified that by setting $\beta_5 = \alpha_5$ and $\beta_6 = -\alpha_6$, the network can perfectly compensate for the PMD. In this way, the resulting signal at the output of the compensation layer can be obtained as follows:

$$\begin{bmatrix} y_{X,l+1}[n] \\ x_{Y,l+1}[n] \end{bmatrix} = \mathcal{F}^{-1}\left(\begin{bmatrix} \cos(\beta_5) & -\sin(\beta_5) \\ \sin(\beta_5) & \cos(\beta_5) \end{bmatrix}\begin{bmatrix} e^{j\omega\beta_6/2} & 0 \\ 0 & e^{-j\omega\beta_6/2} \end{bmatrix}\begin{bmatrix} \cos(\beta_5) & \sin(\beta_5) \\ -\sin(\beta_5) & \cos(\beta_5) \end{bmatrix}\right.$$
$$\left.\mathcal{F}\left(\begin{bmatrix} y_{X,l}[n] \\ y_{Y,l}[n] \end{bmatrix}\right)\right) = \begin{bmatrix} x_{X,l}[n] \\ y_{Y,l}[n] \end{bmatrix}. \tag{4.23}$$

□

4.2.3.5 CD compensation layer

CD impact is described in this work by the parameter $\alpha_4 = Dz$, representing the accumulated chromatic dispersion. The impaired complex signal at the output of the layer is obtained as:

$$y_{p,l}[n] = x_{p,l+1}[n] = \mathcal{F}^{-1}\left(e^{-j\frac{\alpha_4\lambda^2}{4\pi c}\omega^2}\mathcal{F}\left(\mathbf{x}_{p,l}[n]\right)\right). \tag{4.24}$$

Proposition 5. *The CD layer is isomorphic.*

Proof. It can be verified that by setting $\beta_7 = -\alpha_4$, the layer perfectly compensates for the CD impact. The signal at the output of the compensation layer is expressed as follows:

$$\begin{aligned} y_{p,l+1}[n] &= \mathcal{F}^{-1}\left(e^{-j\frac{\beta_7\lambda^2}{4\pi c}\omega^2}\mathcal{F}\left(\mathbf{y}_{p,l}[n]\right)\right) = \mathcal{F}^{-1}\left(e^{-j\frac{-\alpha_4\lambda^2}{4\pi c}\omega^2}e^{-j\frac{\alpha_4\lambda^2}{4\pi c}\omega^2}\mathcal{F}\left(\mathbf{x}_{p,l}[n]\right)\right) \\ &= x_{p,l}[n]. \end{aligned} \tag{4.25}$$

□

4.2.4 Network architecture and training

As all the compensation layers considered in the chain are isomorphic, the parametric compensation network has the architecture depicted in Figure 4.8. The layers are reversely ordered compared to the impairments and depend on the compensation parameter $\boldsymbol{\beta}$. The network contains multiple trainable layers related to the impairments compensation and two static layers that perform the RRC matched filtering and the downsampling.

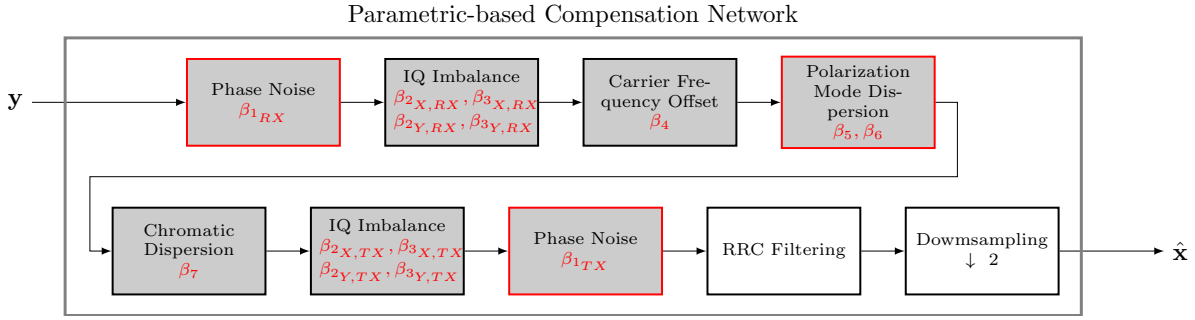

Figure 4.8 – The architecture of the parametric compensation network

The gray-colored blocks from Figure 4.8 update their parameters during the preamble-based training. In addition, the red contour blocks re-update their parameters during pilot-based and self-labeling training. The training operations are detailed in Algorithm 1.

Algorithm 1 Network training

Initialize parameters: $\boldsymbol{\beta} \leftarrow \boldsymbol{\beta}_0$
Preamble-based training
Set stop_condition
$\mathbf{x}_{target} \leftarrow \tilde{\mathbf{x}}_0$
while stop_condition = false **do**
    $\mathbf{x}_{out} \leftarrow \mathbf{P}_0\mathbf{B}(\boldsymbol{\beta})\tilde{\mathbf{y}}$
    Compute the loss: $\|\tilde{\mathbf{x}}_{target} - \tilde{\mathbf{x}}_{out}\|^2$
    Update parameters: $\boldsymbol{\beta}$
end while
Pilots-based training
Set stop_condition
Set detection interval: p
Select time-variant parameters for training: $\boldsymbol{\beta}_{\text{temp}} = [\boldsymbol{\beta}_{1_{RX}}, \boldsymbol{\beta}_{1_{TX}}, \boldsymbol{\beta}_5, \boldsymbol{\beta}_6]$
while stop_condition = false **do**
    $\mathbf{x}_{out} \leftarrow \mathbf{P}_1\mathbf{B}(\boldsymbol{\beta})\tilde{\mathbf{y}}$
    $\mathbf{x}_{target} \leftarrow \tilde{\mathbf{x}}_1$
    Compute the loss: $\|\tilde{\mathbf{x}}_{target} - \tilde{\mathbf{x}}_{out}\|^2$
    Update parameters: $\boldsymbol{\beta}_{temp}$
    Number of iterations choice
    if i mod $p = 0$ **then**
        $\mathbf{x}_{out} \leftarrow \mathbf{B}(\boldsymbol{\beta})\tilde{\mathbf{y}}$
        $\mathbf{x}_{target} \leftarrow \tilde{\mathbf{x}}_{det}$
        detection_err $= \|\tilde{\mathbf{x}}_{target} - \tilde{\mathbf{x}}_{out}\|^2$
        if detection_error stop decreasing **then**
            stop_condition = true
        end if
    end if
end while
Self-labeling training
Set stop condition
while stop_condition = false **do**
    $\mathbf{x}_{out} \leftarrow \mathbf{B}(\boldsymbol{\beta})\tilde{\mathbf{y}}$
    $\mathbf{x}_{target} \leftarrow \tilde{\mathbf{x}}_{det}$
    Compute the loss: $\|\tilde{\mathbf{x}}_{target} - \tilde{\mathbf{x}}_{out}\|^2$
    Update parameters: $\boldsymbol{\beta}_{temp}$
end while

4.3 Results

This section presents the results obtained using the proposed parametric network. First, in 4.3.1, the simulation results obtained in the case of a DP coherent optical communications are analyzed with respect to the statistical performance and computational complexity. Then, in 4.3.2, a comparison with two conventional approaches, a classical static MLP and a DSP approach, is made. Finally, in 4.3.3, an experimental demonstration of the proposed scheme is performed in a simplified scenario consisting of an SP coherent optical system.

The signals employed in this section are generated using Python's scientific libraries NumPy [Har+20], and SciPy [Vir+20]. The compensation network on the receiver side is implemented using the PyTorch framework [Pas+19], and the training is performed using ADAM optimizer [Kin+14] with learning rates of 10^{-4} for the preamble-training and 10^{-2} for pilot-based and self-labeling training.

4.3.1 Simulation results

The simulations used 600600 $\mathcal{M}$-QAM symbols for each scenario. From these, 600 are used as a preamble, 20000 as pilot symbols inserted periodically (each $30th$ symbol is a pilot) into data blocks of length 600. The rest of the 580000 symbols is used as payload, resulting in an overhead of 3.4%. The system parameters are detailed in Table 4.2, where $\mathbf{N_{RRC}}$ refers to the number of RRC filter taps.

The transmitted signals are impaired by lasers' PNs related to 100 kHz laser linewidth, both on the transmitter and receiver side. If not stated otherwise, the IQ imbalance is related to 1 dB amplitude variation and 10° phase difference, both on the transmitter and receiver. The CD corresponds to an accumulated CD Dz of 17000 ps/nm, which comes from a fiber dispersion coefficient of $D = 17$ ps/nm-km and a fiber length of $z = 1000$ km. PMD is considered constant during a block of N_b symbols and its parameters are randomly chosen from the following intervals: $\theta \in [-\pi/2, \pi/2)$, and $\tau \in [5 \text{ ps}, 20 \text{ ps}]$. Finally, the CFO between the two lasers is 200 MHz.

Table 4.2 – System parameters

BDR [GBaud]	$\mathbf{f_s}$ **[GHz]**	$\mathbf{N_{RRC}}$	$\boldsymbol{\alpha}_{rf}$	$\mathbf{N_0}$	$\mathbf{N_b}$	**Pilot int.**
20	40	61	0.15	600	600	30

ADAM optimizer performs a local optimization. Consequently, the network parameters need to be initialized so that local minimum problems are avoided. This problem can be solved in practice using another global optimization algorithm before network training or by initializing the parameters with values obtained from a coarse estimation using different approaches like the conventional DSP algorithms. However, for simplicity, in this work, the initialization is done in a way that avoids these problems. Concretely, the parameters are initialized as follows:

— IQ imbalance compensation parameters are set up as $\beta_{2_{X/Y,TX/RX}} = 1$, $\beta_{3_{X/Y,TX/RX}} = 0$ - the case where the signal is not impaired by IQ imbalance;

— CFO compensation parameter β_4 is randomly chosen from an interval corresponding to a CFO value in $\Delta F \in [187.5 \text{ MHz}, \ 212.5 \text{ MHz}]$;

— CD compensation parameter β_7 is randomly chosen from an interval related to a fiber length between 995 km and 1005 km, as prior knowledge about the fiber length and dispersion coefficient generally exist;

— PMD compensation parameters are set up as $\beta_5 = 0$, $\beta_6 = 0$ - the case where the signal is not impaired by PMD;

— Laser PN compensation parameter $\boldsymbol{\beta_{1_{TX/RX}}}$ is initialized with 0 during the preamble-based estimation. Then, during the pilot-based and self-labeling training, it is re-initialized with the last estimated phase compensation parameter of the previous block.

The detection error of the proposed technique is computed for each $20th$ iteration. This leads to a good compromise between statistical performance and computational complex-

Table 4.3 – Network and optimizer parameters

Stage	**Network parameters**		**Optimizer parameters**	
	Static	**Adaptive**	**Learning rate**	**Maximum iterations**
Preamble	RRC Downsampling	$\boldsymbol{\beta_{1_{TX/RX}}}$ $\beta_{2_{X/Y,TX/RX}}$ $\beta_{3_{X/Y,TX/RX}}$ β_4, β_5, β_6, β_7	10^{-4}	50000
Pilots	RRC Downsampling $\beta_{2_{X/Y,TX/RX}}$ $\beta_{3_{X/Y,TX/RX}}$ β_4, β_7	$\boldsymbol{\beta_{1_{TX/RX}}}$ β_5, β_6	10^{-2}	500
Self-labeling	RRC Downsampling $\beta_{2_{X/Y,TX/RX}}$ $\beta_{3_{X/Y,TX/RX}}$ β_4, β_7	$\boldsymbol{\beta_{1_{TX/RX}}}$ β_5, β_6	10^{-2}	100

ity. In Table 4.3 the network and optimizer parameters are summarized.

4.3.1.1 Influence of the number of constant phases

The number of constant phases considered for a data block may be a critical aspect that needs to be set up. The number of constant phases is related to the parameter K. There are multiple implications related to it:

— A reduced value of K better describes the laser phase evolution and, by this, good statistical performance may be achieved;

— A large value of K reduces the number of parameters to be estimated and diminishes the computational demands;

— During the pilot-based training, a reduced value of K may lead to overfitting as the number of parameters and training symbols have similar values.

In the case of the preamble-based training, the number of parameters to estimate is low compared to the number of training symbols, and the risk of overfitting is reduced. Moreover, the preamble processing is performed only once and does not impose stringent requirements regarding computational complexity. As a consequence, in this work, for the preamble-based training, the value of K was fixed at 25. On the contrary, pilot-based training is prone to overfitting, and a reduced computational complexity is a crucial requirement for it, as it is performed for each data block.

To focus only on the impact of the number of constant phase values, first, a communication not impaired by PMD is assumed. In Figure 4.9, the evolution of MSE with respect to the number of training iterations for 16-QAM transmission at an OSNR of 20 dB for different values of K during pilot-based training is depicted. For $K = 25$, the training error has the lowest value, but the detection and testing errors are the highest compared to the other cases where $K = 50$ and $K = 100$, respectively. Moreover, even if the training error decreases, the detection and testing errors increase with the iterations for $K = 25$, suggesting overfitting. In the other cases, the training, detection, and testing errors have a similar evolution, and no overfitting seems to occur. As a consequence, these two values are used in future simulations.

4.3.1.2 EVM performance

In the following simulations, the EVM metric will be used to assess the communication performance. According to 3GPP specifications [36118], EVM should be maximum 17.5% for 4-QAM, 12.5% for 16-QAM, 8% for 64-QAM, and 3.5% for 256-QAM. In Figure 4.10,

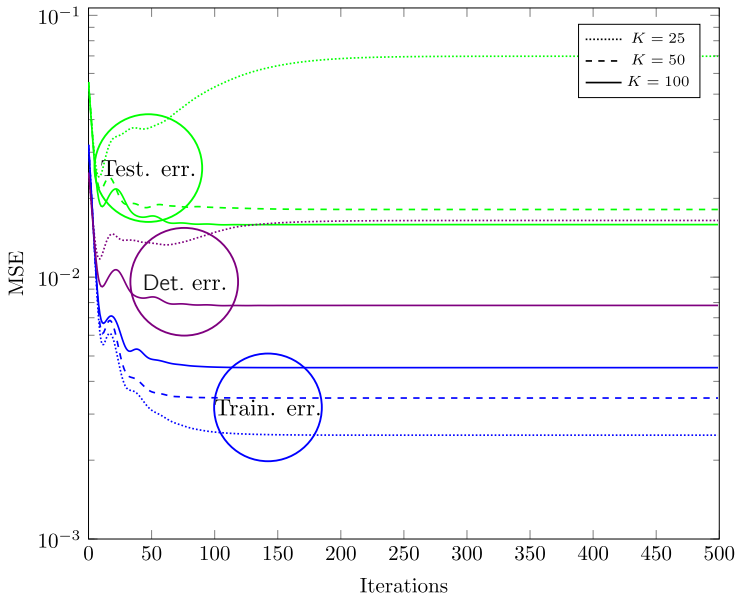

Figure 4.9 – MSE evolution with respect to the number of iterations during the supervised pilot-based tracking for different values of K

the EVM evolution with respect to OSNR is depicted for multiple $\mathcal{M}$-QAMs, where $K = 100$ for 4-QAM and 16-QAM, and $K = 50$ for 64-QAM and 256-QAM. The choice of K is based on the fact that 4-QAM and 16-QAM are generally used in noisier scenarios, where a value of $K = 100$ leads to better robustness to noise. On the contrary, 64-QAM and 256-QAM can only be employed in case of low noise levels, and a value of $K = 50$ better reproduces the phase evolution, typically leading to improved performance. With red are denoted the simulated EVM performances obtained for a channel impaired only by AWGN. In Figure 4.10, it can be seen that EVM have an identical evolution that does not depend on modulation format. The EVM values for a AWGN channels are below the imposed threshold after OSNRs of approximately 15 dB for 4-QAM, 18 dB for 16-QAM, 22 dB for 64-QAM, and 29 dB for 256-QAM. In Figure 4.10a the EVM evolution for testing data after the supervised pilot-based training is depicted. It can be seen that the proposed parametric network in the considered setup can reach the desired performance after OSNRs of approximately 18 dB for 4-QAM, 22 dB for 16-QAM, and 28 dB for 64-QAM. In Figure 4.10b the EVM evolution for the testing data after the self-labeling training is depicted. It can be seen that the proposed parametric network reaches the desired performance after OSNR values of approximately 17 dB for 4-QAM, 20 dB for 16-QAM, and 26 dB for 64-QAM. In both scenarios, for 256-QAM, even if the EVM performance increases with OSNR, the imposed performance bound cannot be reached.

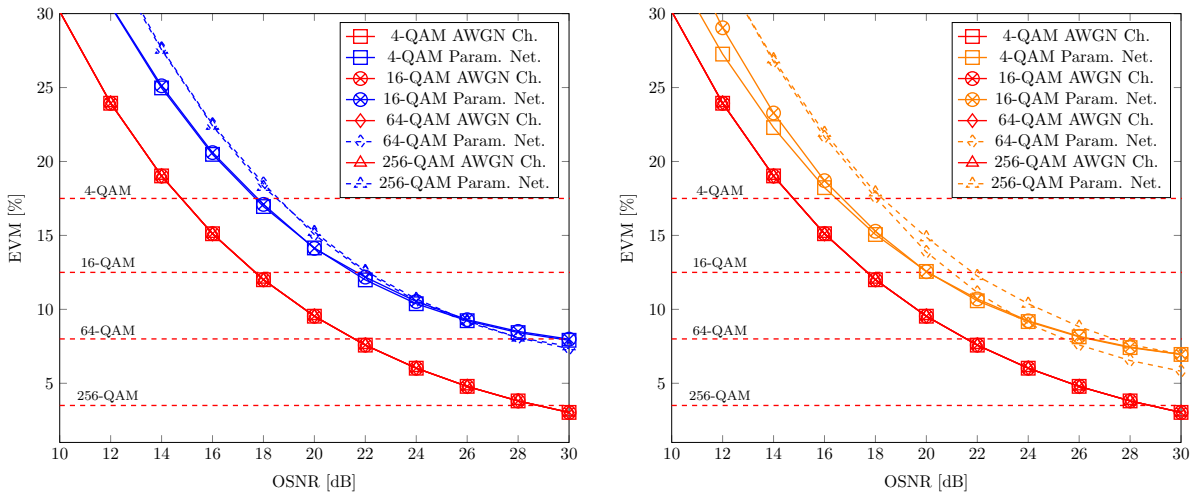

(a) EVM evolution with respect to OSNR after the supervised pilot-based training

(b) EVM evolution with respect to OSNR after the self-labeling training

Figure 4.10 – EVM performance of the proposed parametric network

4.3.1.3 BER performance

The BER performance is analyzed in the following. Based on that, in Figure 4.11, the BER evolution with respect to OSNR for $K = 50$ and $K = 100$ is depicted for multiple $\mathcal{M}$-QAM transmissions. In Figure 4.11a, the BER evolution is presented for the testing data after the supervised pilot-based, while in Figure 4.11b for the testing data after the

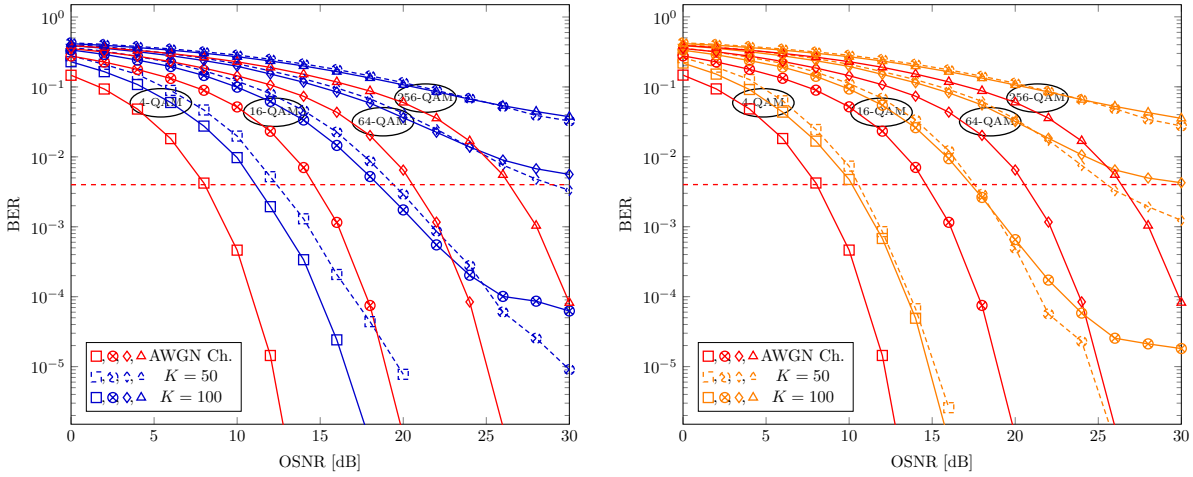

(a) BER evolution with respect to OSNR after the supervised pilot-based training

(b) BER evolution with respect to OSNR after the self-labeling training

Figure 4.11 – BER performance of the proposed parametric network

self-labeling training. It can be seen that the curves have a similar evolution in both cases, with the self-labeling step improving the general performance of the network. In the case of the pilot-based training, it can be seen that the value of $K = 100$ obtains better performance until an OSNR value of 25 dB for all modulations considered, while the value of $K = 50$ performs better after it. A similar evolution is obtained for the self-labeling step, but in this case, the value of OSNR where $K = 50$ starts performing better is 20 dB. Finally, it should be noticed that for all modulations, except the 256-QAM, the proposed method can achieve BER values under the imposed threshold of 4×10^{-3}.

4.3.1.4 Influence of IQ imbalance

The influence of different configurations of IQ imbalance on the BER performance is shown in Figure 4.12. It is important to notice that when an IQ imbalance configuration is changed (TX/RX), the other one (RX/TX) is fixed with the following values: $g = 1$ dB and $\vartheta = 10°$. Additionally, the impairments impact the two polarization signals identically. It can be observed that transmitter IQ imbalance introduces a bigger penalty on system performance compared to the receiver IQ imbalance in this scenario. The proposed network can reach the desired performance for values of receiver IQ imbalance as high as 1.5 dB and 20°, while for transmitter IQ imbalance at these values and above, its performance is above the imposed BER threshold.

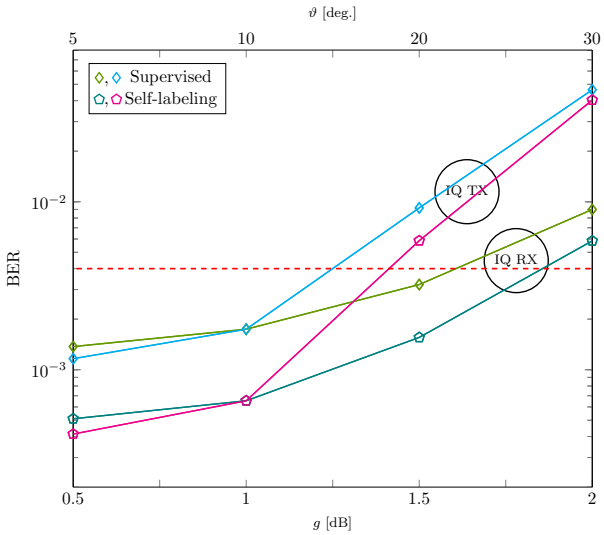

Figure 4.12 – Network performance for different values of IQ imbalance (TX & RX) for 16-QAM at an OSNR of 20 dB

4.3.1.5 Computational complexity

A critical aspect of DP coherent optical communications is the computational complexity, as these systems benefit from very large communications bandwidths. In this chapter, the computational cost is measured using the number of Floating-point Operations (FLOPs) [Hun05]. The number of FLOPs required during each step of training and testing can be seen in Table 4.4. It is worth mentioning that the training requires multiple iterations, while the testing is performed only once. As expected, the most computationally demanding operation is the preamble-based training. The pilot-based and self-labeling training requires a relatively similar number of FLOPs, fewer than preamble-based training. Finally, it can be seen that the testing is a less computationally demanding operation.

In addition, a complexity versus performance analysis is operated. The number of iterations required during the training depends a lot on the optimization algorithm employed. Different from the preamble-based training, which is performed only once, the pilot-based and self-labeling training are operated for each data block, so they are critical from a computational point of view. A performance versus complexity analysis for these two training steps can be seen in Table 4.5, where the BER values obtained after a particular number of iterations for a 16-QAM at an OSNR of 20 dB are shown. In the scenario considered, the best performance-complexity compromise could be obtained

Table 4.4 – Number of FLOPs required by the parametric network

Metric	**Training**			**Testing**
	Preamble	**Pilots**	**Self-labeling**	
FLOPs	2.8×10^5	2.4×10^5	2.4×10^5	7.9×10^4

Table 4.5 – Complexity versus performance regarding the BER and the number of training iterations

Iterations	**After pilot-based training**		**After self-labeling training**	
	BER	**FLOPs**	**BER**	**FLOPs**
25	2×10^{-2}	6.1×10^6	1.6×10^{-2}	1.2×10^7
50	4.9×10^{-3}	1.2×10^7	2.3×10^{-3}	2.4×10^7
75	2.2×10^{-3}	1.8×10^7	8.4×10^{-4}	3.6×10^7
100	1.9×10^{-3}	2.4×10^7	7.8×10^{-4}	4.8×10^7

using only the pilot-based training with 75 iterations. With this number of iterations, a BER of 2.2×10^{-3} is achieved requiring a total number of FLOPs approximately equal to 1.8×10^{7}. However, better compromises may be obtained by using a more advanced optimization algorithm.

4.3.2 Comparison to the conventional DL and DSP compensation techniques

In the following, a comparison to conventional approaches used for impairments compensation is introduced. The comparison considers two conventional approaches: a DL technique and the local DSP algorithms. It takes into consideration the BER performance and the computational complexity.

4.3.2.1 DL approach

A typical approach used for compensation and detection is the one that uses a static MLP network [Fre+21; Sid+18]. The block diagram of the system of interest used for this particular comparison is shown in Figure 4.13. A SP coherent optical system impaired only by static imperfections including IQ imbalance (both on transmitter and receiver sides), residual CD and CFO is assumed. For this setup, a 4-QAM is used at 20 Gbaud with a sampling frequency of 20 GHz. The length of the blocks (preamble and data blocks) is of $N_{0,b} = 30$ symbols with no pilot symbols. Both transmitter and receiver IQ imbalance are related to 1 dB amplitude variation and 10° phase difference. The residual values are 17 ps/nm for CD, and 12.5 MHz for CFO.

The MLP architecture consists of 6 layers (4 hidden, 1 input, 1 output). The hidden layers are composed of $20N_b$ neurons. Rectified Linear Unit (ReLU) is used as activation function. The network is trained using 1000000 iterations with a batch size of 1000 samples, while the test dataset contains 1500000 samples. The proposed parametric network is composed of 4 layers corresponding to each impairment. Only a preamble of 30 samples is used for training, while 10000 samples compose the testing dataset. The

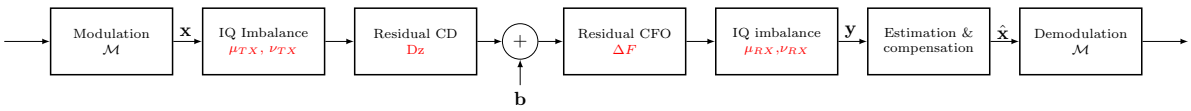

Figure 4.13 – Block diagram of the system of interest

MLP network has to optimize 1551120 parameters, while in the case of the parametric network, the number of parameters is limited to 10.

The results obtained for this setup can be seen in Figure 4.14, where the performance obtained by a Clairvoyant equalizer is also considered. It can be seen that the Clairvoyant equalizer and MLP network have slightly better performance than the proposed parametric network, which introduces an approximate penalty of 0.5 dB at BER threshold.

Next, in addition to the previously mentioned imperfections, a laser PN related to 100 kHz is considered on the receiver side. The MLP network does not change its architecture, as the system knowledge is difficult to be added to such architectures. On the contrary, in the parametric network, a new layer related to laser PN compensation is added, and a pilot is inserted into each data block. A single constant level of phase is assumed for each data block, increasing the number of parameters to be estimated by the proposed network to 11. The results obtained in this scenario can be seen in Figure 4.15. It can be noted that the proposed parametric network still manages to compensate for the impairments, and its BER results are below the imposed threshold, while the MLP network cannot reach the desired QoS. This is because the MLP have difficulties tracking time-variant channels.

Considering the computational complexity, the MLP network requires 15.4×10^{12} FLOPs, while the proposed parametric network requires 8.2×10^{2} FLOPs during the testing in the case of a static channel. In the case of the time-variant channel, the testing operation requires 10^{3} FLOPs, and, in addition, 5.1×10^{3} FLOPs are required for a single

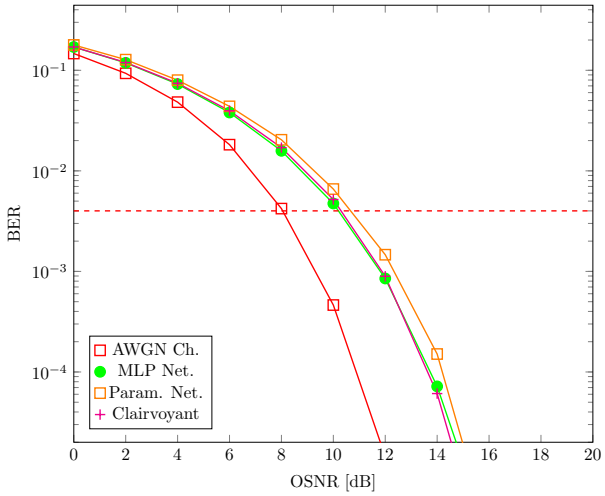

Figure 4.14 – BER evolution with respect to OSNR for a static channel

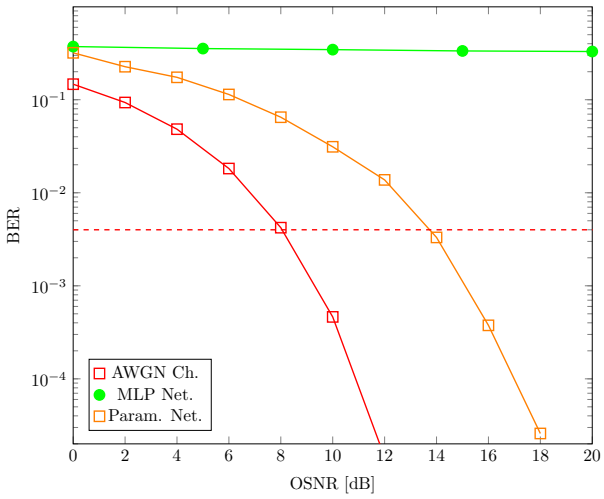

Figure 4.15 – BER evolution with respect to OSNR for a time-variant channel

iteration of pilot-based and self-labeling training.

4.3.2.2 Conventional DSP approach

The second competing technique considered is the one that compensates for impairments using the conventional DSP algorithms studied in Chapter 2. The block diagram of the SP coherent optical system of interest for this comparison is depicted in 4.16. The system is impacted by IQ imbalance (both on transmitter and receiver sides), CFO, and laser PN. The symbol rate for this scenario is of 20 Gbaud, and the sampling frequency is 20 GHz. A number of 300300 symbols were used for this comparison. From these, 300 symbols represent the preamble, while the rest are split into data blocks of length 300, with pilot symbols at an interval of 30 symbols, resulting an overhead of 3.4%. The imperfections correspond to 1 dB and 10° IQ imbalance on transmitter and receiver sides, 200 MHz CFO and a laser PN related to a laser linewidth of 100 kHz.

In the case of local DSP compensation, the algorithms identified in Chapter 2 are used in the three configurations considered. On the other hand, the parametric network compensates for the impairments in the reversed order using the compensation parameters

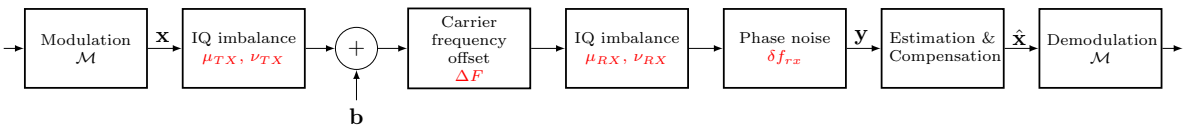

Figure 4.16 – Block diagram of the system of interest

($\boldsymbol{\beta}_1$, β_2, β_3, and β_4). In Figure 4.17, the BER evolution with respect to OSNR for the two competing approaches is shown. The performance of the "DSP v1" approach is poor, especially in the case of 16-QAM. This is due to transmitter IQ imbalance, which cannot be correctly compensated for by GSOP. Next, in the second configuration, "DSP v2", an improvement can be seen. However, the performance is still limited for 16-QAM. This arises because the performance of the laser PN compensation algorithm is highly degraded in the presence of transmitter IQ imbalance. Finally, in the "DSP v3" configuration, an important improvement is displayed. Still, the performance does not match the performance of the proposed parametric network. At the BER threshold, the "DSP v3" technique introduces a penalty of approximately 0.2 dB for 4-QAM and 1.7 dB for 16-QAM, respectively.

Next, the computational complexity of the two approaches is reported in the following using the number of FLOPs required by each technique. The number of FLOPs required in the "DSP v3" scenario is approximate 8.9×10^3. In the case of the parametric network, a single iteration for pilot-based and self-labeling training requires 4×10^4 FLOPs, while the testing operation needs 7.8×10^3 FLOPs.

4.3.3 Experimental demonstration

To further validate the effectiveness of the proposed parametric network, experimental validation is conducted. The validation is performed in a simplified back-to-back coherent optical communication chain impaired by transmitter IQ imbalance, CFO and laser PN.

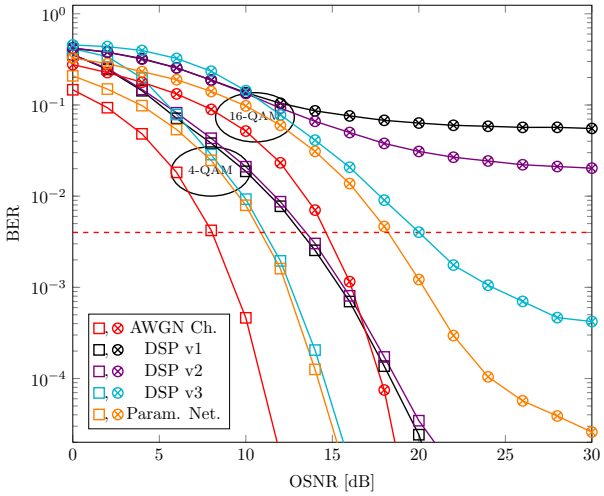

Figure 4.17 – BER evolution with respect to OSNR

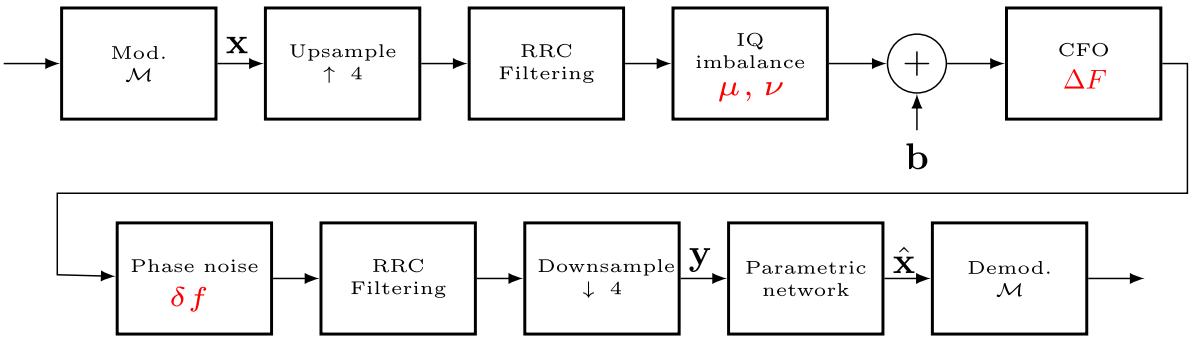

Figure 4.18 – Block diagram of the experimental system of interest

The block diagram of the setup is depicted in Figure 4.18. In the considered system, the transmitted signal is first upsampled with a factor 4 and RRC filtered. Then the signal undergoes multiple linear impairments. On the receiver side, the signal is once again RRC filtered, then downsampled. Finally, the impact of the impairments is compensated for by the parametric network, and the transmitted data is recovered after demodulation.

The network architecture that performs the compensation can be seen in Figure 4.19. As previously, the network compensates for the impairments in reversed order by using some compensation parameters ($\boldsymbol{\beta}_1$, β_2, β_3, β_4). The experimental setup used for this work is similar to the one in Figure 3.15.

For this experimental demonstration, 3900 4-QAM symbols were used. From these, 300 are employed for the preamble, and the rest consists of data blocks of 300 symbols with pilots inserted periodically (each $30th$ symbol is a pilot). The impairments are as follows:

— a laser PN corresponding to 100 kHz laser linewidth;
— an IQ imbalance related to 1 dB amplitude variation and 20° phase deviation;
— a CFO of 200 MHz between the two lasers.

The parameters initialization is performed as is 4.3.1. An approximate number of 3000 iterations were used for preamble-based training, 400 iterations for pilot-based training, and 100 for self-labeling training.

In this experimental demonstration, the influence of K during the self-labeling training

Figure 4.19 – Block diagram of the compensation network

was investigated using as metric the EVM, because no errors were detected on the receiver side. In Figure 4.20, the values of EVM for different K during the self-labeling training can be seen. It can be seen that for $K = 300$, EVM has a value of 20.34% that decreases to 17.5% for $K = 2$, reaching the imposed threshold of 3GPP.

In Figure 4.21, different constellations of the received signal in particular scenarios are depicted. It can be seen that the constellation after synchronization is highly impacted by impairments. Then, after the pilot-based training, most of the impact of the impairments is compensated for, and an EVM of 21.98% is obtained. Finally, a finer compensation is achieved after the self-labeling training, improving the system performance.

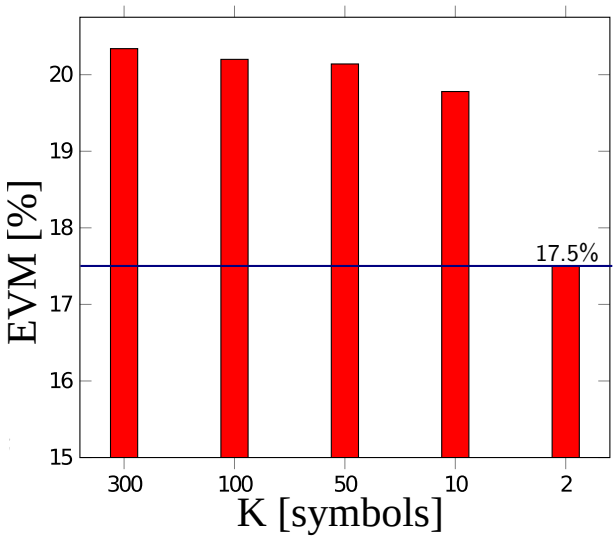

Figure 4.20 – EVM for different values of K during the self-labeling training

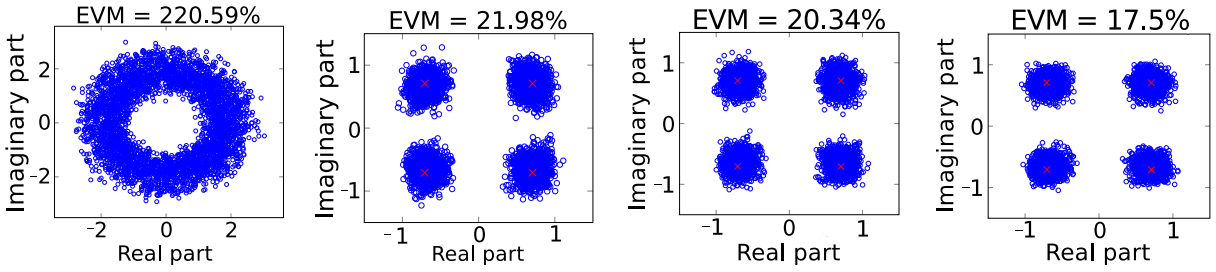

(a) Constellation after synchronization

(b) Constellation after pilot-based training

(c) Constellation after self-labeling training with $K = 300$

(d) Constellation after self-labeling training with $K = 2$

Figure 4.21 – Received signal constellations after different processing steps

4.4 Conclusion and discussion

In this chapter, a new multi-layer parametric network has been presented for global compensation of multiple linear imperfections in DP coherent optical systems. The proposed parametric network benefits from the imperfections parametrization and compensates for their impact using some compensation parameters. Moreover, the parametric network has a multi-layer architecture that is composed of multiple parametric layers that are reversely ordered compared to imperfections. This type of architecture is flexible, as new impairments can be easily included, their order in the network may be changed, and new models may be relatively easily added. Furthermore, an original training scheme that allows the tracking of time-variant impairments and requires reduced datasets was identified in this work.

The simulation results proved the effectiveness of the approach in terms of EVM and BER in complex scenarios where laser PN, IQ imbalance, CD, PMD, and CFO occur. The proposed technique was compared to a conventional MLP network and the local DSP algorithms investigated in Chapter 2. Our network outperforms these two approaches in all scenarios considered for a time-variant channel. Different from the MLP, the parametric network can alleviate time-variant imperfections. Compared to local DSP algorithms, the network avoids the complications related to the cascading of multiple compensation techniques. In addition, an experimental demonstration in a simplified scenario was operated and proved the effectiveness of the proposed parametric network.

The main drawback of the approach is the computational complexity. Even if its computational complexity is much more reduced compared to a classical DL network, the proposed network has a higher computational cost than the DSP approaches. Still, at first glance, it can be reduced by using more advanced optimization algorithms as in [Cho+22a], which represents one of the future directions for this work. Other investigations will be performed regarding the order of compensation layers in the network architecture. Finally, another future objective is to include nonlinearity compensation in the proposed network architecture. In this way, an almost complete global compensation of all impairments of the coherent optical systems may be achieved.

Conclusion and perspectives

The recent developments in coherent optical communications have been driven, among others, by the advances in digital compensation techniques. This thesis was centered on the compensation of linear imperfections using DSP-based and ML/DL-based approaches. In the following, the main contributions and some prospects are emphasized.

Chapter 2 has presented the most critical linear impairments that occur in an optical communication chain such as PN, IQ imbalance, CD, and CFO. These imperfections must be compensated for to recover the transmitted data. Thus, an extensive analysis of the compensation performance of conventional DSP algorithms in different scenarios was conducted. This study demonstrated that, despite its effectiveness in particular scenarios where only a few imperfections occur, cascaded DSP algorithms might have issues when multiple imperfections occur. In particular, we have also illustrated that the best optical combination of DSP algorithms is often challenging to identify and is usually statistically suboptimal.

In Chapter 3, a parametric DSP-based estimation and compensation technique was proposed. Departing from the cascaded approach, this new technique focuses on the global compensation of all the system imperfections, a strategy that has been relatively little explored in the literature. This technique can globally estimate the linear impairments such as laser PN, IQ imbalance, CD, and CFO that appear in single-polarization systems. The simulations proved that the algorithm has good statistical performance. Considering the estimation accuracy, the technique is relatively close to the CRLB in some scenarios, while the penalty introduced compared to a modified Clairvoyant technique is rather reduced. Compared to the conventional DSP algorithms, some simulations have shown that the proposed global approach performs better for high-order modulations. As opposed to the conventional cascaded DSP approach, the proposed parametric approach can differentiate between receiver and transmitter impairments such as lasers' phases and IQ imbalance, making it well suited for monitoring optical communication chains. To validate the effectiveness of the proposed approach, early experimental tests have also been conducted in our laboratory with a simple optical communication chain. While the proposed parametric approach usually outperforms the conventional cascaded DSP technique, its main

drawback is its flexibility. Indeed, extending the proposed approach to other communication chains, such as dual-polarization systems, usually requires additional non-trivial mathematical development.

Chapter 4 has described a new model-based parametric network that overcomes the limitation of the previous technique. The network has an original architecture composed of multiple parametric compensation layers. Each layer is parametrized by some parameters related to the imperfections model. In the compensation network, these layers are reversely ordered compared to imperfections. Unlike conventional DL networks, this parametric network benefits from the model knowledge and is very flexible since it allows the integration of new impairments in the network structure. An innovative training technique based on symbol constellation knowledge is also introduced. This technique limits the presence of overfitting and allows the tracking of time-variant parameters. The simulation results have proved that the approach is effective for the global compensation of multiple impairments in PDM optical communication systems. The parametric network outperforms the conventional DL approach in the case of a time-variant channel and the local DSP approach in all the considered scenarios. Finally, the experimental investigation proved that the network could operate on experimental data.

Even if the algorithms proposed in this thesis show promising results, several areas for improvement are detailed in the following.

— First, the computational complexity of the proposed techniques, even if significantly reduced compared to the standard DL approaches, is still higher than the one of the conventional DSP approach. The computational complexity is critical in practice, especially during the tracking stage. To reduce it, future work will consider more advanced optimization algorithms such as the LM algorithm or Deep Unfolded techniques.
— Secondly, while the multi-layer structure of the channel is perfectly controlled in simulations, the channel model is usually uncertain in practice. In particular, choosing a priori general multi-layer parametric structure that performs well with different experimental signals is far from trivial. Therefore, similarly to the hyperparameter optimization step in DL algorithms, future works will focus on identifying the optimal multi-layer arrangement. This research direction could also provide new algorithms for physical layer monitoring.
— Thirdly, while the proposed techniques focus on the compensation of (widely) linear

impairments, additional works should also consider the compensation of nonlinear impairments and channel effects (such as modulator nonlinearity, Kerr effects, etc.). In particular, several research teams work on compensating fiber nonlinearity with low-complexity DL networks like LDBP. While it is challenging to integrate the conventional cascaded DSP algorithms with LDBP approach, we believe that the joint combination of our multi-layer parametric network with LDBP is quite natural. Specifically, both approaches rely on parametric layers which can be jointly optimized.

— Finally, early experimental investigations were conducted during the thesis. In the future, we propose extending them to more complex scenarios to further validate our approaches' effectiveness.

Appendix A

The compensation strategy in conventional coherent optical communications

Reference	PN	IQ imb.	PMD	CD	CFO	Others	Tech.
[Fat+08]	X	RX	X	X	X	X	-
[Cha+09]	X	RX	X	X	X	X	-
[Far+13]	X	RX	X	X	X	IQ skew	Joint
[Flu+16]	X	TX	X	X	X	IQ skew Offset control	Joint
[Sil+16]	X	RX	X	X	X	IQ skew	Joint
[Ngu+17]	X	✓	X	X	X	X	-
[Zha+19a]	X	✓	X	X	X	X	-
[Lag+20]	X	Tx	Demux.	X	X	X	Joint
[Xie+12]	RX	X	X	X	✓	X	Cascaded
[Sat+10]	RX	X	X	X	X	X	-
[Pev+09]	RX	X	X	X	X	X	-
[Vit+83]	RX	X	X	X	X	X	-
[Sei08]	RX	X	X	X	X	X	-
[Fat+10]	RX	X	X	X	X	X	-
[Pfa+09]	RX	X	X	X	X	X	-
[Mag+12]	RX	X	X	X	X	X	-
[Mil+16]	RX	X	Demux.	X	X	X	Cascaded
[Zha+12]	RX	X	X	X	X	X	-
[Paj+15]	RX	X	X	X	X	X	-
[Paj+15]	RX	X	X	X	X	X	-

[Mor+11]	RX	X	X	X	X	X	-
[Col+11]	✓	X	X	X	X	X	-
[Sav08]	X	X	X	✓	X	X	-
[Egh+14]	X	X	X	✓	X	X	-
[Xu+10]	X	X	X	✓	X	X	-
[Gol+07]	X	X	X	✓	X	X	-
[Gey+10]	X	X	X	✓	X	X	-
[Kud+09]	X	X	X	✓	X	X	-
[Xu+11]	X	X	X	✓	X	X	-
[Kus+09a]	X	X	X	✓	X	X	-
[Ip+07]	X	X	✓	✓	X	X	Joint
[Lav+15]	X	X	✓	X	X	X	-
[Han+05]	Rx	X	Demux.	X	✓	X	Cascaded
[Ngu+15]	X	✓	Demux.	X	X	X	Joint
[Büt+20]	X	X	✓	X	X	Nonlinearity	Joint
[Häg+20b]	X	X	✓	X	X	Nonlinearity	Joint
[Zho+11]	X	X	X	X	✓	X	-
[Lev+07]	X	X	X	X	✓	X	-
[Hof+08]	RX	X	X	X	✓	X	Cascaded
[Zha+15]	X	X	X	X	✓	X	-
[Nak+10]	X	X	X	X	✓	X	-
[Wan+01]	X	X	X	X	✓	X	-
[Sel+09]	X	X	X	X	✓	X	-
[Fat+11]	X	X	X	X	✓	X	-
[Mei+13]	RX	X	X	X	✓	X	Joint
[Mor+13]	RX	X	X	X	✓	X	Joint

Appendix B

CRLB COMPUTATION FOR THE NONLINEAR PARAMETERS

The computation of the CRLB is performed in this appendix in order to obtain the performance bounds of the nonlinear parameters estimation, as the MSE is lower bounded by the CRLB [Kay93].

In (3.24), all the parameters of $\boldsymbol{\chi}_\phi$ are unknown. In this case, the signal model contains parameters indetermination. As a consequence, first, it is considered that $\phi_{tx} = \phi_{rx} = 0$. By setting this, the following transformation can be used: $\boldsymbol{\chi}_\phi \rightarrow \boldsymbol{\chi}$. Secondly, without modifying the noise statistics and maintaining the generality, it can be assumed that $\mu_{RX} = 1$. Furthermore, the unrealistic scenario whithin $|\nu_{RX}| \geq 1$ is excluded from the estimation problem.

Assuming these, the received signal can be rewritten as follows:

$$\mathbf{y} = \mathbf{x}(\boldsymbol{\Omega}) + \mathbf{b}, \tag{B.1}$$

where $\boldsymbol{\Omega}$ is a real-valued vector corresponding to the parameters that need to be estimated, $\mathbf{x}(\boldsymbol{\Omega})$ is a vector that contains the part of the signal which is deterministic:

$$\mathbf{x}(\boldsymbol{\Omega}) = \mathbf{F}(\boldsymbol{\kappa})\boldsymbol{\chi}_{TX} + \nu_{RX}\mathbf{F}^*(\boldsymbol{\kappa})\boldsymbol{\chi}_{TX}^*, \tag{B.2}$$

with

$$\mathbf{F}(\boldsymbol{\kappa}) = \mathbf{G}(\boldsymbol{\kappa})\mathbf{x}, \tag{B.3}$$

$$\boldsymbol{\chi}_{TX} = \begin{bmatrix} \mu_{TX} \\ \nu_{TX} \end{bmatrix}, \tag{B.4}$$

$$\mathbf{X} = \begin{bmatrix} \mathbf{x} & \mathbf{x}^* \end{bmatrix}, \tag{B.5}$$

and $\mathbf{b}$ is the noise vector.

The real-valued augmented signal model is used in order to compute the CRLB:

$$\tilde{\mathbf{y}} = \tilde{\mathbf{x}}(\mathbf{\Omega}) + \tilde{\mathbf{b}}, \tag{B.6}$$

where $\tilde{\mathbf{x}}(\mathbf{\Omega})$ is expressed as:

$$\tilde{\mathbf{x}}(\mathbf{\Omega}) = \begin{bmatrix} \Re e((1+\nu_{RX})\mathbf{F}(\boldsymbol{\kappa})\boldsymbol{\chi}_{TX}) \\ \Im m((1-\nu_{RX})\mathbf{F}(\boldsymbol{\kappa})\boldsymbol{\chi}_{TX}) \end{bmatrix}. \tag{B.7}$$

The parameters to be estimated are in a number of 9, and are given by:

$$\mathbf{\Omega} = \begin{bmatrix} \boldsymbol{\kappa} & \mathbf{\Omega}_{RX} & \mathbf{\Omega}_{TX} & \sigma^2 \end{bmatrix}^T, \tag{B.8}$$

where

- $\mathbf{\Omega}_r = \begin{bmatrix} \Re e(\nu_{RX}) & \Im m(\nu_{RX}) \end{bmatrix}$ is a row vector describing the impact of receiver IQ imbalance,
- $\mathbf{\Omega}_t = \begin{bmatrix} \Re e(\boldsymbol{\chi}_{TX}^T) & \Im m(\boldsymbol{\chi}_{TX}^T) \end{bmatrix}$ is a row vector describing the impact of the transmitter IQ imbalance parameters,
- σ^2 is the noise variance.

With Ω_k is denoted the $k-th$ element of $\mathbf{\Omega}$. The CRLBs of Ω_k is given by the k-th diagonal element of the inverse of the Fisher Information Matrix i.e.:

$$\text{CRLB}[\Omega_k] = [\mathbf{I}^{-1}(\mathbf{\Omega})]_{kk}. \tag{B.9}$$

where $\mathbf{I}(\mathbf{\Omega})$ is the Fisher Information Matrix, and $[.]_{kl}$ corresponds to the (k,l)-th element of a matrix. As the augmented received vector is distributed as $\tilde{\mathbf{y}} \sim \mathcal{N}(\tilde{\mathbf{x}}(\mathbf{\Omega}), \mathbf{C}(\mathbf{\Omega}))$, where $\mathbf{C}(\mathbf{\Omega})$ is the covariance matrix, the (k,l)-th element of the Fisher Information Matrix is given by [Kay93]:

$$[\mathbf{I}(\mathbf{\Omega})]_{kl} = \left[\frac{\partial \tilde{\mathbf{x}}(\mathbf{\Omega})}{\partial [\mathbf{\Omega}]_k}\right]^T \mathbf{C}^{-1}(\mathbf{\Omega}) \left[\frac{\partial \tilde{\mathbf{x}}(\mathbf{\Omega})}{\partial [\mathbf{\Omega}]_l}\right] + \frac{1}{2}\mathbf{tr}\left[\mathbf{C}^{-1}(\mathbf{\Omega})\frac{\partial \mathbf{C}(\mathbf{\Omega})}{\partial [\mathbf{\Omega}]_k}\mathbf{C}^{-1}(\mathbf{\Omega})\frac{\partial \mathbf{C}(\mathbf{\Omega})}{\partial [\mathbf{\Omega}]_l}\right]. \tag{B.10}$$

Regarding the partial derivatives of $\tilde{\mathbf{x}}(\boldsymbol{\Omega})$, $\frac{\partial \tilde{\mathbf{x}}(\boldsymbol{\Omega})}{\partial \sigma^2} = \mathbf{0}$, and:

$$\frac{\partial \tilde{\mathbf{x}}(\boldsymbol{\Omega})}{\partial [\boldsymbol{\kappa}]_k} = \begin{bmatrix} \Re e((1+\nu_{RX}^*)\mathbf{L}_k \boldsymbol{\chi}_{TX}) \\ \Im m((1-\nu_{RX}^*)\mathbf{L}_k \boldsymbol{\chi}_{TX}) \end{bmatrix}, \tag{B.11}$$

$$\frac{\partial \tilde{\mathbf{x}}(\boldsymbol{\Omega})}{\partial [\boldsymbol{\Omega}_{RX}]_k} = \begin{bmatrix} \Re e(\mathbf{F}(\boldsymbol{\kappa})\boldsymbol{\chi}_{TX}) & \Im m(\mathbf{F}(\boldsymbol{\kappa})\boldsymbol{\chi}_{TX}) \\ -\Im m(\mathbf{F}(\boldsymbol{\kappa})\boldsymbol{\chi}_{TX}) & \Re e(\mathbf{F}(\boldsymbol{\kappa})\boldsymbol{\chi}_{TX}) \end{bmatrix} \mathbf{e}_k, \tag{B.12}$$

$$\frac{\partial \tilde{\mathbf{x}}(\boldsymbol{\Omega})}{\partial [\boldsymbol{\Omega}_{TX}]_k} = \begin{bmatrix} \Re e((1+\nu_{RX}^*)\mathbf{F}(\boldsymbol{\kappa})) & -\Im m((1+\nu_{RX}^*)\mathbf{F}(\boldsymbol{\kappa})) \\ \Im m((1-\nu_{RX}^*)\mathbf{F}(\boldsymbol{\kappa})) & \Re e((1-\nu_{RX}^*)\mathbf{F}(\boldsymbol{\kappa})) \end{bmatrix} \mathbf{e}_k. \tag{B.13}$$

where:

$$\mathbf{L}_k = \frac{\partial \mathbf{F}(\boldsymbol{\kappa})}{\partial [\boldsymbol{\kappa}]_k} = \frac{\partial \mathbf{G}(\boldsymbol{\kappa})}{\partial [\boldsymbol{\kappa}]_k} \mathbf{X}. \tag{B.14}$$

As the noise is placed before receiver IQ imbalance, the AWGN loses the circularity property, and $\tilde{\mathbf{b}}$ is defined as:

$$\tilde{\mathbf{b}} = (\tilde{\mathbf{M}}(\nu_{RX}) \otimes \mathbf{I}_{N_0})\tilde{\mathbf{w}}, \tag{B.15}$$

with:

$$\tilde{\mathbf{M}}(\nu_{RX}) = \mathbf{I}_2 + \begin{bmatrix} \Re e(\nu_{RX}) & \Im m(\nu_{RX}) \\ \Im m(\nu_{RX}) & -\Re e(\nu_{RX}) \end{bmatrix}, \tag{B.16}$$

and $\mathbf{w}$ the noise before being impacted by the receiver IQ imbalance. The covariance matrix is expressed as $\mathbf{C}(\boldsymbol{\Omega}) = \frac{\sigma^2}{2}\tilde{\mathbf{M}}(\nu_{RX})\tilde{\mathbf{M}}^T(\nu_{RX}) \otimes \mathbf{I}_{N_0}$, and the derivatives $\frac{\partial \mathbf{C}(\boldsymbol{\Omega})}{\partial [\boldsymbol{\Omega}]_k}$ are non-zero only for the receiver's IQ imbalance parameter $\boldsymbol{\Omega}_{RX}$, and for the noise variance σ^2. These non-zero derivatives are given by:

$$\frac{\partial \mathbf{C}(\boldsymbol{\Omega})}{\partial [\boldsymbol{\Omega}_{RX}]_0} = \sigma^2 \begin{bmatrix} \Re e(\nu_{RX}) + 1 & 0 \\ 0 & \Re e(\nu_{RX}) - 1 \end{bmatrix} \otimes \mathbf{I}_{N_p}, \tag{B.17}$$

$$\frac{\partial \mathbf{C}(\boldsymbol{\Omega})}{\partial [\boldsymbol{\Omega}_{RX}]_1} = \sigma^2 \begin{bmatrix} \Im m(\nu_{RX}) & 1 \\ 1 & \Im m(\nu_{RX}) \end{bmatrix} \otimes \mathbf{I}_{N_p}, \tag{B.18}$$

$$\frac{\partial \mathbf{C}(\boldsymbol{\Omega})}{\partial \sigma^2} = \frac{1}{2}\tilde{\mathbf{M}}(\nu_{RX})\tilde{\mathbf{M}}^T(\nu_{RX}) \otimes \mathbf{I}_{N_0}. \tag{B.19}$$

List of publications

Journal papers

[Fru+22a] Alexandru Frunză, Vincent Choqueuse, Pascal Morel, and Stéphane Azou, « A Parametric Network for the Global Compensation of Physical Layer Linear Impairments in Coherent Optical Communications », *in*: *IEEE Open Journal of the Communications Society* 3 (Aug. 2022), pp. 1428–1444, DOI: https://doi.org/10.1109/OJCOMS.2022.3201130

[Fru+21a] Alexandru Frunză, Vincent Choqueuse, Pascal Morel, and Stéphane Azou, « Global estimation and compensation of linear effects in coherent optical systems based on nonlinear least squares », *in*: *IEEE Systems Journal* 16 (Sept. 2021), pp. 3794–3804, DOI: https://doi.org/10.1109/JSYST.2021.3111777

[Fru+22d] Alexandru Frunză, Vincent Choqueuse, Pascal Morel, Alexandru Serbănescu, and Stéphane Azou, « An Experimental Demonstration of Joint Linear Impairments Compensation in Coherent Optical Systems Using a Parametric Network », *in*: *Journal of Military Technology* (Dec. 2022)

[Fru+22b] Alexandru Frunză, Vincent Choqueuse, Pascal Morel, and Stéphane Azou, « Robust Estimation of the Channel Parameters in Presence of Transmitter and Receiver IQ Impairments », *in*: *Journal of Military Technology* (Dec. 2022)

Conference papers

[Cho+22b] Vincent Choqueuse, Alexandru Frunză, Adel Belouchrani, Stéphane Azou, and Pascal Morel, « ParamNet: A Multi-Layer Parametric Network for Joint Channel Estimation and Symbol Detection », *in*: *30th European Signal Processing Conference (EUSIPCO)*, Belgrade, Serbia, 2022, pp. 1–5, URL: https://eurasip.org/Proceedings/Eusipco/Eusipco2022/pdfs/0001616.pdf

[Fru+22c] Alexandru Frunză, Vincent Choqueuse, Pascal Morel, Alexandru Serbănescu, and Stéphane Azou, « A Comparative Study on Global Compensation Techniques for Coherent Optical Communications », *in*: *2022 14th International Conference on Communications (COMM)*, IEEE, Bucharest, Romania, 2022, pp. 1–6, DOI: https://doi.org/10.1109/COMM54429.2022.9817216

[Fru+21b] Alexandru Frunză, Jacqueline E Sime, Vincent Choqueuse, Pascal Morel, and Stéphane Azou, « Joint Estimation and Compensation of Transmitter IQ Imbalance and Laser Phase Noise in Coherent Optical Systems », *in*: *2021 IEEE Photonics Conference (IPC)*, IEEE, Vancouver, BC, Canada, 2021, pp. 1–2, DOI: https://doi.org/10.1109/IPC48725.2021.9593089

Open-access archive

[Cho+22a] Vincent Choqueuse, Alexandru Frunză, Stéphane Azou, and Pascal Morel, « PhyCOM: A Multi-Layer Parametric Network for Joint Linear Impairments Compensation and Symbol Detection », *in*: *arXiv preprint arXiv:2203.00266* (Mar. 2022), pp. 1–20, DOI: 10.48550/arXiv.2203.00266

BIBLIOGRAPHY

[36118] 3GPP TS 36.104, « Base Station (BS) Radio Transmission and Reception (2018) », *in*: ***version 16*** *(version 16.0.0)* (2018).

[Agr00] Govind P Agrawal, « Nonlinear fiber optics », *in*: *Nonlinear Science at the Dawn of the 21st Century*, Springer, 2000, pp. 195–211.

[Agr12] Govind P Agrawal, *Fiber-optic communication systems*, vol. 222, John Wiley & Sons, 2012.

[Agr+16] Erik Agrell, Magnus Karlsson, AR Chraplyvy, David J Richardson, Peter M Krummrich, Peter Winzer, Kim Roberts, Johannes Karl Fischer, Seb J Savory, Benjamin J Eggleton, et al., « Roadmap of optical communications », *in*: *Journal of Optics* 18.*6* (May 2016), p. 063002.

[Bar+90] John R Barry and Edward A Lee, « Performance of coherent optical receivers », *in*: *Proceedings of the IEEE* 78.*8* (Aug. 1990), pp. 1369–1394.

[Bec+99] Philippe M Becker, Anders A Olsson, and Jay R Simpson, *Erbium-doped fiber amplifiers: fundamentals and technology*, Elsevier, 1999.

[Bit+20a] Bertold Ian Bitachon, Amirhossein Ghazisaeidi, Benedikt Baeuerle, Marco Eppenberger, and Juerg Leuthold, « Deep learning based digital back propagation with polarization state rotation & phase noise invariance », *in*: *2020 Optical Fiber Communications Conference and Exhibition (OFC)*, IEEE, San Diego, CA, USA, 2020, pp. 1–3.

[Bit+20b] Bertold Ian Bitachon, Amirhossein Ghazisaeidi, Marco Eppenberger, Benedikt Baeuerle, Masafumi Ayata, and Juerg Leuthold, « Deep learning based digital backpropagation demonstrating SNR gain at low complexity in a 1200 km transmission link », *in*: *Optics Express* 28.*20* (Sept. 2020), pp. 29318–29334.

[Bja93] Anders Bjarklev, *Optical fiber amplifiers: design and system applications*, Artech House Boston, 1993.

[Bor+14] Robert Borkowski, Darko Zibar, and Idelfonso Tafur Monroy, « Anatomy of a digital coherent receiver », *in*: *IEICE Transactions on Communications* 97.*8* (Aug. 2014), pp. 1528–1536.

[Bor+13] Max Born and Emil Wolf, *Principles of optics: electromagnetic theory of propagation, interference and diffraction of light*, Elsevier, 2013.

[Bos19] Gabriella Bosco, « Advanced modulation techniques for flexible optical transceivers: The rate/reach tradeoff », *in*: *Journal of Lightwave Technology* 37.*1* (Dec. 2019), pp. 36–49.

[Buc+04] Fred Buchali and Henning Bulow, « Adaptive PMD compensation by electrical and optical techniques », *in*: *Journal of Lightwave Technology* 22.*4* (Apr. 2004), pp. 1116–1126.

[Buc+19] Fred Buchali, Karsten Schuh, Roman Dischler, Mathieu Chagnon, Vahid Aref, Henning Buelow, Qian Hu, Florian Pulka, Massimo Frascolla, Esmaeel Alhammadi, Adel Samhan, Islam Younis, Mohamed El-Zonkoli, and Peter Winzer, « 1.3-Tb/s single-channel and 50.8-Tb/s WDM transmission over field-deployed fiber », *in*: *45th European Conference on Optical Communication (ECOC 2019)*, Dublin, Ireland, 2019, pp. 1–4, DOI: 10.1049/cp.2019.1017.

[Bul+08] Henning Bulow, Fred Buchali, and Axel Klekamp, « Electronic dispersion compensation », *in*: *Journal of lightwave technology* 26.*1* (Jan. 2008), pp. 158–167.

[Büt+20] Rick M Bütler, Christian Häger, Henry D Pfister, Gabriele Liga, and Alex Alvarado, « Model-based machine learning for joint digital backpropagation and PMD compensation », *in*: *Journal of Lightwave Technology* 39.*4* (Oct. 2020), pp. 949–959.

[Cha+09] Sun Hyok Chang, Hwan Seok Chung, and Kwangjoon Kim, « Impact of quadrature imbalance in optical coherent QPSK receiver », *in*: *IEEE Photonics Technology Letters* 21.*11* (Mar. 2009), pp. 709–711.

[Cho+22a] Vincent Choqueuse, Alexandru Frunză, Stéphane Azou, and Pascal Morel, « PhyCOM: A Multi-Layer Parametric Network for Joint Linear Impairments Compensation and Symbol Detection », *in*: *arXiv preprint arXiv:2203.00266* (Mar. 2022), pp. 1–20, DOI: 10.48550/arXiv.2203.00266.

[Cho+22b] Vincent Choqueuse, Alexandru Frunză, Adel Belouchrani, Stéphane Azou, and Pascal Morel, « ParamNet: A Multi-Layer Parametric Network for Joint Channel Estimation and Symbol Detection », *in*: *30th European Signal Processing Conference (EUSIPCO)*, Belgrade, Serbia, 2022, pp. 1–5, URL: https://eurasip.org/Proceedings/Eusipco/Eusipco2022/pdfs/0001616.pdf.

[Chu+10] Hwan Seok Chung, Sun Hyok Chang, and Kwangjoon Kim, « Effect of IQ mismatch compensation in an optical coherent OFDM receiver », *in*: *IEEE photonics technology letters* 22.*5* (Jan. 2010), pp. 308–310.

[Cis21] U Cisco, « Global - 2021 Forecast Highlights », *in*: *Cisco: San Jose, CA, USA* (2021), URL: https://www.cisco.com/c/dam/m/en_us/solutions/service-provider/vni-forecast-highlights/pdf/Global_2021_Forecast_Highlights.pdf.

[Col+11] Giulio Colavolpe, Tommaso Foggi, Enrico Forestieri, and Marco Secondini, « Impact of phase noise and compensation techniques in coherent optical systems », *in*: *Journal of Lightwave Technology* 29.*18* (Aug. 2011), pp. 2790–2800.

[Cub12] Erkin Cubukcu, « Root raised cosine (RRC) filters and pulse shaping in communication systems », *in*: *AIAA Conference*, JSC-CN-26387, May 2012.

[Dav+11] Christopher C Davis and Thomas E Murphy, « Fiber-optic communications », *in*: *IEEE Signal Processing Magazine* 28.*4* (July 2011), pp. 147–150.

[Der92] Frowin Derr, « Coherent optical QPSK intradyne system: Concept and digital receiver realization », *in*: *Journal of Lightwave Technology* 10.*9* (Sept. 1992), pp. 1290–1296.

[Des+87] Emmanuel Desurvire, Jay R Simpson, and PC Becker, « High-gain erbium-doped traveling-wave fiber amplifier », *in*: *Optics letters* 12.*11* (Nov. 1987), pp. 888–890.

[Di +10] Gianni Di Domenico, Stéphane Schilt, and Pierre Thomann, « Simple approach to the relation between laser frequency noise and laser line shape », *in*: *Applied optics* 49.*25* (Aug. 2010), pp. 4801–4807.

[Egh+14] Amir Eghbali, Håkan Johansson, Oscar Gustafsson, and Seb J Savory, « Optimal least-squares FIR digital filters for compensation of chromatic dispersion in digital coherent optical receivers », *in*: *Journal of lightwave technology* 32.*8* (Feb. 2014), pp. 1449–1456.

[Elr+88] Aly F Elrefaie, Richard E Wagner, DA Atlas, and DG Daut, « Chromatic dispersion limitations in coherent lightwave transmission systems », *in*: *Journal of Lightwave Technology* 6.*5* (May 1988), pp. 704–709.

[Ess+10] René-Jean Essiambre, Gerhard Kramer, Peter J Winzer, Gerard J Foschini, and Bernhard Goebel, « Capacity limits of optical fiber networks », *in*: *Journal of Lightwave Technology* 28.*4* (Feb. 2010), pp. 662–701.

[Eva+92] Stephen G Evangelides, Linn F Mollenauer, James P Gordon, and Neal S Bergano, « Polarization multiplexing with solitons », *in*: *Journal of Lightwave Technology* 10.*1* (Jan. 1992), pp. 28–35.

[Fan+21] Qirui Fan, Chao Lu, and Alan Pak Tao Lau, « Combined Neural Network and Adaptive DSP Training for Long-Haul Optical Communications », *in*: *Journal of Lightwave Technology* 39.*22* (Sept. 2021), pp. 7083–7091.

[Far+13] Md Saifuddin Faruk and Kazuro Kikuchi, « Compensation for in-phase/quadrature imbalance in coherent-receiver front end for optical quadrature amplitude modulation », *in*: *IEEE Photonics Journal* 5.*2* (Mar. 2013), pp. 7800110–7800110.

[Far+10] Md Saifuddin Faruk, Yojiro Mori, Chao Zhang, and Kazuro Kikuchi, « Proper polarization demultiplexing in coherent optical receiver using constant modulus algorithm with training mode », *in*: *OECC 2010 Technical Digest*, IEEE, Sapporo, Japan, 2010, pp. 768–769.

[Far+17] Md Saifuddin Faruk and Seb J Savory, « Digital signal processing for coherent transceivers employing multilevel formats », *in*: *Journal of Lightwave Technology* 35.*5* (Feb. 2017), pp. 1125–1141.

[Fat+10] Irshaad Fatadin, David Ives, and Seb J Savory, « Laser linewidth tolerance for 16-QAM coherent optical systems using QPSK partitioning », *in*: *IEEE Photonics Technology Letters* 22.*9* (Feb. 2010), pp. 631–633.

[Fat+11] Irshaad Fatadin and Seb J Savory, « Compensation of frequency offset for 16-QAM optical coherent systems using QPSK partitioning », *in*: *IEEE Photonics Technology Letters* 23.*17* (June 2011), pp. 1246–1248.

[Fat+08] Irshaad Fatadin, Seb J Savory, and David Ives, « Compensation of quadrature imbalance in an optical QPSK coherent receiver », *in*: *IEEE Photonics Technology Letters* 20.*20* (Sept. 2008), pp. 1733–1735.

[Fic21] Jessica Fickers, « Modulation Formats and Digital Signal Processing for Fiber-optic Communications With Coherent Detection », PhD thesis, Brussels School of Engineering, 2021.

[Flu+16] Chris RS Fludger and Theo Kupfer, « Transmitter impairment mitigation and monitoring for high baud-rate, high order modulation systems », *in*: *ECOC 2016; 42nd European Conference on Optical Communication*, VDE, Dusseldorf, Germany, 2016, pp. 1–3.

[For15] Optical Internetworking Forum, *Integrable Tunable Laser Assembly Multi Source Agreement, OIF-ITLA-MSA-01.3*, July 2015.

[Fre+20] Pedro J Freire, Vladislav Neskornuik, Antonio Napoli, Bernhard Spinnler, Nelson Costa, Ginni Khanna, Emilio Riccardi, Jaroslaw E Prilepsky, and Sergei K Turitsyn, « Complex-valued neural network design for mitigation of signal distortions in optical links », *in*: *Journal of Lightwave Technology* 39.*6* (Dec. 2020), pp. 1696–1705.

[Fre+21] Pedro J Freire, Yevhenii Osadchuk, Bernhard Spinnler, et al., « Performance versus complexity study of neural network equalizers in coherent optical systems », *in*: *Journal of Lightwave Technology* 39.*19* (July 2021), pp. 6085–6096.

[Fru+21a] Alexandru Frunză, Vincent Choqueuse, Pascal Morel, and Stéphane Azou, « Global estimation and compensation of linear effects in coherent optical systems based on nonlinear least squares », *in*: *IEEE Systems Journal* 16 (Sept. 2021), pp. 3794–3804, DOI: https://doi.org/10.1109/JSYST.2021.3111777.

[Fru+22a] Alexandru Frunză, Vincent Choqueuse, Pascal Morel, and Stéphane Azou, « A Parametric Network for the Global Compensation of Physical Layer Linear Impairments in Coherent Optical Communications », *in*: *IEEE Open*

Journal of the Communications Society 3 (Aug. 2022), pp. 1428–1444, DOI: https://doi.org/10.1109/OJCOMS.2022.3201130.

[Fru+22b] Alexandru Frunză, Vincent Choqueuse, Pascal Morel, and Stéphane Azou, « Robust Estimation of the Channel Parameters in Presence of Transmitter and Receiver IQ Impairments », *in*: *Journal of Military Technology* (Dec. 2022).

[Fru+22c] Alexandru Frunză, Vincent Choqueuse, Pascal Morel, Alexandru Serbănescu, and Stéphane Azou, « A Comparative Study on Global Compensation Techniques for Coherent Optical Communications », *in*: *2022 14th International Conference on Communications (COMM)*, IEEE, Bucharest, Romania, 2022, pp. 1–6, DOI: https://doi.org/10.1109/COMM54429.2022.9817216.

[Fru+22d] Alexandru Frunză, Vincent Choqueuse, Pascal Morel, Alexandru Serbănescu, and Stéphane Azou, « An Experimental Demonstration of Joint Linear Impairments Compensation in Coherent Optical Systems Using a Parametric Network », *in*: *Journal of Military Technology* (Dec. 2022).

[Fru+21b] Alexandru Frunză, Jacqueline E Sime, Vincent Choqueuse, Pascal Morel, and Stéphane Azou, « Joint Estimation and Compensation of Transmitter IQ Imbalance and Laser Phase Noise in Coherent Optical Systems », *in*: *2021 IEEE Photonics Conference (IPC)*, IEEE, Vancouver, BC, Canada, 2021, pp. 1–2, DOI: https://doi.org/10.1109/IPC48725.2021.9593089.

[Gai+20] Simone Gaiarin, Francesco Da Ros, Rasmus T Jones, and Darko Zibar, « End-to-end optimization of coherent optical communications over the split-step Fourier method guided by the nonlinear Fourier transform theory », *in*: *Journal of Lightwave Technology* 39.*2* (Oct. 2020), pp. 418–428.

[Gar86] Floyd Gardner, « A BPSK/QPSK timing-error detector for sampled receivers », *in*: *IEEE Transactions on communications* 34.*5* (May 1986), pp. 423–429.

[Gar91] Reiner B Garreis, « 90 degree optical hybrid for coherent receivers », *in*: *Optical Space Communication II*, vol. 1522, International Society for Optics and Photonics, Feb. 1991, pp. 210–219.

[Gey+10] JC Geyer, CRS Fludger, T Duthel, C Schulien, and B Schmauss, « Efficient frequency domain chromatic dispersion compensation in a coherent Polmux QPSK-receiver », *in*: *Optical Fiber Communication Conference*, Optica Publishing Group, San Diego, California United States, 2010, OWV5.

[God80] Dominique Godard, « Self-recovering equalization and carrier tracking in two-dimensional data communication systems », *in*: *IEEE transactions on communications* 28.*11* (Nov. 1980), pp. 1867–1875.

[Gol+07] Gilad Goldfarb and Guifang Li, « Chromatic dispersion compensation using digital IIR filtering with coherent detection », *in*: *IEEE Photonics Technology Letters* 19.*13* (June 2007), pp. 969–971.

[Gol+73] Gene H Golub and Victor Pereyra, « The differentiation of pseudo-inverses and nonlinear least squares problems whose variables separate », *in*: *SIAM Journal on Numerical Analysis* 10.*2* (Apr. 1973), pp. 413–432.

[Häg+20a] Christian Häger and Henry D Pfister, « Physics-based deep learning for fiber-optic communication systems », *in*: *IEEE Journal on Selected Areas in Communications* 39.*1* (Nov. 2020), pp. 280–294.

[Häg+20b] Christian Häger, Henry D Pfister, Rick M Bütler, Gabriele Liga, and Alex Alvarado, « Model-based machine learning for joint digital backpropagation and PMD compensation », *in*: *Optical Fiber Communication Conference*, Optical Society of America, San Diego, California United States, 2020, W3D–3.

[Han+05] Yan Han and Guifang Li, « Coherent optical communication using polarization multiple-input-multiple-output », *in*: *Optics Express* 13.*19* (Sept. 2005), pp. 7527–7534.

[Har+20] Charles R. Harris et al., « Array programming with NumPy », *in*: *Nature* 585 (Sept. 2020), pp. 357–362, DOI: 10.1038/s41586-020-2649-2.

[Hay08] Simon S Haykin, *Adaptive filter theory*, Pearson Education India, 2008.

[Hil+92] Paul M Hill, Robert Olshansky, and WK Burns, « Optical polarization division multiplexing at 4 Gb/s », *in*: *IEEE photonics technology letters* 4.*5* (May 1992), pp. 500–502.

[Ho05] Keang-Po Ho, *Phase-modulated optical communication systems*, Springer Science & Business Media, 2005.

[Hof+08] Sebastian Hoffmann, Suhas Bhandare, Timo Pfau, Olaf Adamczyk, Christian Wordehoff, Ralf Peveling, Mario Porrmann, and Reinhold Noé, « Frequency and phase estimation for coherent QPSK transmission with unlocked DFB lasers », *in*: *IEEE Photonics Technology Letters* 20.*18* (Sept. 2008), pp. 1569–1571.

[Hua+13] Dezhao Huang, Tee-Hiang Cheng, and Changyuan Yu, « Decision-aided carrier phase estimation with selective averaging for low-cost optical coherent communication », *in*: *2013 9th International Conference on Information, Communications & Signal Processing*, IEEE, Tainan, Taiwan, 2013, pp. 1–3.

[Hun05] Raphael Hunger, *Floating point operations in matrix-vector calculus*, Munich University of Technology, Inst. for Circuit Theory and Signal, 2005.

[Ip+07] Ezra Ip and Joseph M Kahn, « Digital equalization of chromatic dispersion and polarization mode dispersion », *in*: *Journal of Lightwave Technology* 25.*8* (Aug. 2007), pp. 2033–2043.

[ITU18] ITU-T G Suppl. 64, *PON transmission technologies above 10 Gbit/s per wavelength*, ITU, Feb. 2018, URL: `http://handle.itu.int/11.1002/1000/13589`.

[ITU11] ITU-T G.689.1, *Multichannel DWDM applications with single-channel optical interfaces*, ITU, Nov. 2011, URL: `https://www.itu.int/rec/T-REC-G.698.1-200911-I/en`.

[ITU20] ITU-T G.8310, *Architecture of the metro transport network*, ITU, Dec. 2020, URL: `http://handle.itu.int/11.1002/1000/14516`.

[ITU04] ITU-T G975.1 Recommandation, *Forward error correction for high bit-rate DWDM submarine systems*, Feb. 2004.

[Jal+19] Fatemeh Jalali and Amir Zaimbashi, « Cognitive radio spectrum sensing under joint TX/RX I/Q imbalance and uncalibrated receiver », *in*: *IEEE Systems Journal* 14.*1* (Mar. 2019), pp. 105–112.

[Jeo+10] Seok-Hwan Jeong and Ken Morito, « Novel Optical 90° Hybrid Consisting of a Paired Interference Based 2×4 MMI Coupler, a Phase Shifter and a 2×2 MMI Coupler », *in*: *Journal of lightwave technology* 28.*9* (May 2010), pp. 1323–1331.

[Joh+98] Richard Johnson, Philip Schniter, Thomas J Endres, James D Behm, Donald Richard Brown, and Raúl A Casas, « Blind equalization using the constant modulus criterion: A review », *in*: *Proceedings of the IEEE* 86.*10* (Oct. 1998), pp. 1927–1950.

[Kam86] Pooi Kam, « Maximum likelihood carrier phase recovery for linear suppressed-carrier digital data modulations », *in*: *IEEE Transactions on Communications* 34.*6* (June 1986), pp. 522–527.

[Kam+02] Ivan P Kaminow and Tingye Li, *Optical fiber telecommunications volume IV B: systems and impairments*, Academic Press, 2002.

[Kao+66] K Charles Kao and George A Hockham, « Dielectric-fibre surface waveguides for optical frequencies », *in*: *Proceedings of the Institution of Electrical Engineers*, vol. 113, 7, IET, 1966, pp. 1151–1158.

[Kay93] Steven M Kay, *Fundamentals of Statistical Signal Processing: Estimtion Theory*, Prentice Hall PTR, 1993, pp. 254–260.

[Kik11] Kazuro Kikuchi, « Performance analyses of polarization demultiplexing based on constant-modulus algorithm in digital coherent optical receivers », *in*: *Optics Express* 19.*10* (May 2011), pp. 9868–9880.

[Kik15] Kazuro Kikuchi, « Fundamentals of coherent optical fiber communications », *in*: *Journal of lightwave technology* 34.*1* (Aug. 2015), pp. 157–179.

[Kin+14] Diederik P Kingma and Jimmy Ba, « Adam: A method for stochastic optimization », *in*: *arXiv preprint arXiv:1412.6980* (Dec. 2014), pp. 1–15.

[Kud+09] Riichi Kudo, Takayuki Kobayashi, Koichi Ishihara, Yasushi Takatori, Akihide Sano, and Yutaka Miyamoto, « Coherent optical single carrier transmission using overlap frequency domain equalization for long-haul optical systems », *in*: *Journal of Lightwave Technology* 27.*16* (Aug. 2009), pp. 3721–3728.

[Kus+09a] M Kuschnerov, FN Hauske, K Piyawanno, B Spinnler, A Napoli, and B Lankl, « Adaptive chromatic dispersion equalization for non-dispersion managed coherent systems », *in*: *Optical Fiber Communication Conference*, Optica Publishing Group, San Diego, California, United States, 2009, OMT1.

[Kus+09b] Maxim Kuschnerov, Fabian N Hauske, Kittipong Piyawanno, Bernhard Spinnler, Mohammad S Alfiad, Antonio Napoli, and Berthold Lankl, « DSP for coherent single-carrier receivers », *in*: *Journal of lightwave technology* 27.*16* (Aug. 2009), pp. 3614–3622.

[Lag+20] Marwa Kazdoghli Lagha, Robin Gerzaguet, Laurent Bramerie, Mathilde Gay, Marie-Laure Chares, Christophe Peucheret, and Pascal Scalart, « Blind Joint Polarization Demultiplexing and IQ Imbalance Compensation for M-QAM Coherent Optical Communications », *in*: *Journal of Lightwave Technology* 38.*16* (Apr. 2020), pp. 4213–4220.

[Lap+14] Charles Laperle and Maurice O'Sullivan, « Advances in high-speed DACs, ADCs, and DSP for optical coherent transceivers », *in*: *Journal of Lightwave Technology* 32.*4* (Feb. 2014), pp. 629–643.

[Lav+15] Domaniç Lavery, Milen Paskov, Robert Maher, Seb J Savory, and Polina Bayvel, « Modified radius directed equaliser for high order QAM », *in*: *2015 European Conference on Optical Communication (ECOC)*, IEEE, Valencia, Spain, 2015, pp. 1–3.

[Lev+07] Andreas Leven, Noriaki Kaneda, Ut-Va Koc, and Young-Kai Chen, « Frequency estimation in intradyne reception », *in*: *IEEE Photonics Technology Letters* 19.*6* (Feb. 2007), pp. 366–368.

[Lia+19] Junpeng Liang, Yangyang Fan, Zhenning Tao, Xiaofei Su, and Hisao Nakashima, « Transceiver imbalances compensation and monitoring by receiver DSP », *in*: *Journal of Lightwave Technology* 39.*17* (Oct. 2019), pp. 5397–5404.

[Lia+05] Ling Liao, Dean Samara-Rubio, Michael Morse, Ansheng Liu, Dexter Hodge, Doron Rubin, Ulrich D Keil, and Thorkild Franck, « High speed silicon Mach-Zehnder modulator », *in*: *Optics express* 13.*8* (Apr. 2005), pp. 3129–3135.

[Lin+22] Xiang Lin, Shenghang Luo, Octavia A Dobre, Lutz Lampe, Deyuan Chang, and Chuandong Li, « Perturbation-aided deep neural network for dual-polarization optical communication systems », *in*: *Optical Fiber Communication Conference*, Optica Publishing Group, San Diego, CA, USA, 2022, W2A–35.

[Lin+21] Xiang Lin, Shenghang Luo, Sunish Kumar Orappanpara Soman, Octavia A Dobre, Lutz Lampe, Deyuan Chang, and Chuandong Li, « Perturbation theory-aided learned digital back-propagation scheme for optical fiber non-

linearity compensation », *in*: *Journal of Lightwave Technology* 40.*7* (Dec. 2021), pp. 1981–1988.

[Lin+88] Richard A Linke and Alan H Gnauck, « High-capacity coherent lightwave systems », *in*: *Journal of Lightwave Technology* 6.*11* (Nov. 1988), pp. 1750–1769.

[Liu98] Chia-Ling Liu, « Impacts of i/q imbalance on qpsk-ofdm-qam detection », *in*: *IEEE Transactions on Consumer Electronics* 44.*3* (Aug. 1998), pp. 984–989.

[Liu+09] Ling Liu, Zhenning Tao, Weizhen Yan, Shoichiro Oda, Takeshi Hoshida, and Jens C Rasmussen, « Initial tap setup of constant modulus algorithm for polarization de-multiplexing in optical coherent receivers », *in*: *2009 Conference on Optical Fiber Communication*, IEEE, San Diego, CA, USA, 2009, pp. 1–3.

[Ma+15] Xiurong Ma, Zhaocai Ding, Kun Li, and Xiao Wang, « Novel Rx IQ mismatch compensation considering laser phase noise for CO-OFDM system », *in*: *Optical Fiber Technology* 24 (Aug. 2015), pp. 44–48.

[Mag+12] Maurizio Magarini, Luca Barletta, Arnaldo Spalvieri, Francesco Vacondio, Timo Pfau, Marianna Pepe, Marco Bertolini, and Giancarlo Gavioli, « Pilot-symbols-aided carrier-phase recovery for 100-G PM-QPSK digital coherent receivers », *in*: *IEEE Photonics Technology Letters* 24.*9* (Feb. 2012), pp. 739–741.

[Mag+11] Maurizio Magarini, Arnaldo Spalvieri, Francesco Vacondio, Marco Bertolini, Marianna Pepe, and Giancarlo Gavioli, « Empirical modeling and simulation of phase noise in long-haul coherent optical transmission systems », *in*: *Optics Express* 19.*23* (Oct. 2011), pp. 22455–22461.

[Mea+87] Robert J Mears, L Reekie, IM Jauncey, and David N Payne, « Low-noise erbium-doped fibre amplifier operating at 1.54 μm », *in*: *Electronics Letters* 23.*19* (Sept. 1987), pp. 1026–1028.

[Meh+18] Amir Mehrabian and Amir Zaimbashi, « Spectrum sensing in SIMO cognitive radios under primary user transmitter IQ imbalance », *in*: *IEEE Systems Journal* 13.*2* (Aug. 2018), pp. 1210–1218.

[Mei+13] Adaickalavan Meiyappan, Pooi-Yuen Kam, and Hoon Kim, « On decision aided carrier phase and frequency offset estimation in coherent optical receivers », *in*: *Journal of lightwave technology* 31.*13* (Apr. 2013), pp. 2055–2069.

[Mil+16] David S Millar, Robert Maher, Domaniç Lavery, Toshiaki Koike-Akino, Milutin Pajovic, Alex Alvarado, Milen Paskov, Keisuke Kojima, Kieran Parsons, Benn C Thomsen, et al., « Design of a 1 Tb/s superchannel coherent receiver », *in*: *Journal of Lightwave Technology* 34.*6* (Jan. 2016), pp. 1453–1463.

[Min+22] Hao Ming, Xinyu Chen, Xiansong Fang, Lei Zhang, Chenjia Li, and Fan Zhang, « Ultralow complexity long short-term memory network for fiber nonlinearity mitigation in coherent optical communication systems », *in*: *Journal of Lightwave Technology* 40.*8* (Apr. 2022), pp. 2427–2434.

[Miy+79] Terenuma Miya, Y Terunuma, Tatsuya Hosaka, and Tadakazu Miyashita, « Ultimate low-loss single-mode fibre at 1.55 μm », *in*: *Electronics Letters* 15.*4* (1979), pp. 106–108.

[Mor78] Jorge J Moré, « The Levenberg-Marquardt algorithm: implementation and theory », *in*: *Numerical Analysis*, Springer, 1978, pp. 105–116.

[Mor+80] Jorge J Moré, Burton S Garbow, and Kenneth E Hillstrom, *User guide for MINPACK-1*, tech. rep., Geneva, Switzerland: CM-P00068642, Aug. 1980.

[Mor+15] Damián A Morero, Mario A Castrillón, Alejandro Aguirre, Mario R Hueda, and Oscar E Agazzi, « Design tradeoffs and challenges in practical coherent optical transceiver implementations », *in*: *Journal of Lightwave Technology* 34.*1* (Aug. 2015), pp. 121–136.

[Mor+13] Yojiro Mori and Kazuro Kikuchi, « Dual-stage decision-directed phase estimator enabling perfect frequency-offset elimination in digital coherent optical receivers », *in*: *Optical Fiber Communication Conference*, Optical Society of America, Anaheim, California, United States, 2013, OTu3I–7.

[Mor+11] Mohamed Morsy-Osman, Qunbi Zhuge, Lawrence R Chen, and David V Plant, « Feedforward carrier recovery via pilot-aided transmission for single-carrier systems with arbitrary M-QAM constellations », *in*: *Optics express* 19.*24* (Nov. 2011), pp. 24331–24343.

[Mue+76] Kurth Mueller and Markus Muller, « Timing recovery in digital synchronous data receivers », *in*: *IEEE transactions on communications* 24.*5* (May 1976), pp. 516–531.

[Nak+10] Tadao Nakagawa, Koichi Ishihara, Takayuki Kobayashi, Riichi Kudo, Munehiro Matsui, Yasushi Takatori, and Masato Mizoguchi, « Wide-range and fast-tracking frequency offset estimator for optical coherent receivers », *in*: *36th European Conference and Exhibition on Optical Communication*, IEEE, Turin, Italy, 2010, pp. 1–3.

[Nak+11] Tadao Nakagawa, Munehiro Matsui, Takayuki Kobayashi, Koichi Ishihara, Riichi Kudo, Masato Mizoguchi, and Yutaka Miyamoto, « Non-data-aided wide-range frequency offset estimator for QAM optical coherent receivers », *in*: *2011 Optical Fiber Communication Conference and Exposition and the National Fiber Optic Engineers Conference*, IEEE, Los Angeles, CA, USA, 2011, pp. 1–3.

[Nap+17] Antonio Napoli, Mahdi M Mezghanni, Stefano Calabro, Robert Palmer, Guido Saathoff, and Bernhard Spinnler, « Digital predistortion techniques for finite extinction ratio IQ Mach–Zehnder modulators », *in*: *Journal of Lightwave Technology* 35.*19* (July 2017), pp. 4289–4296.

[Ngu+17] Trung-Hien Nguyen, Pascal Scalart, Mathilde Gay, Laurent Bramerie, Olivier Sentieys, Jean-Claude Simon, Christophe Peucheret, and Michel Joindot, « Blind transmitter IQ imbalance compensation in M-QAM optical coherent systems », *in*: *Journal of optical communications and networking* 9.*9* (Aug. 2017), pp. D42–D50.

[Ngu+15] Trung-Hien Nguyen, Pascal Scalart, Michel Joindot, Mathilde Gay, Laurent Bramerie, Christophe Peucheret, Arnaud Carer, Jean-Claude Simon, and Olivier Sentieys, « Joint simple blind IQ imbalance compensation and adaptive equalization for 16-QAM optical communications », *in*: *2015 IEEE International Conference on Communications (ICC)*, IEEE, London, UK, 2015, pp. 4913–4918.

[Osh+17] Timothy O'shea and Jakob Hoydis, « An introduction to deep learning for the physical layer », *in*: *IEEE Transactions on Cognitive Communications and Networking* 3.*4* (Oct. 2017), pp. 563–575.

[Oko+88] Takanori Okoshi and Kazurō Kikuchi, *Coherent optical fiber communications*, vol. 4, Springer Science & Business Media, 1988.

[Oli+20] Vinıcius Oliari, Sebastiaan Goossens, Christian Häger, et al., « Revisiting efficient multi-step nonlinearity compensation with machine learning: An experimental demonstration », *in*: *Journal of Lightwave Technology* 38.*12* (May 2020), pp. 3114–3124.

[Opt17] OpticalCloudInfra, *How Low Can Fiber Loss Go?*, 2017, URL: http://opticalcloudinfra.com/index.php/2017/04/17/low-can-fiber-loss-go/ (visited on 09/07/2022).

[Paj+15] Milutin Pajovic, David S Millar, Toshiaki Koike-Akino, Keisuke Kojima, Valeria Arlunno, and Kieran Parsons, « Multi-pilot aided carrier phase estimation for single carrier coherent systems », *in*: *Signal Processing in Photonic Communications*, Optica Publishing Group, Boston, Massachusetts United States, 2015, SpT4D–4.

[Pas+19] Adam Paszke, Sam Gross, Francisco Massa, et al., « PyTorch: An Imperative Style, High-Performance Deep Learning Library », *in*: *Advances in Neural Information Processing Systems 32*, Curran Associates, Inc., Dec. 2019, pp. 8024–8035.

[Peu12] Christophe Peucheret, « Generation and detection of optical modulation formats », *in*: *Dept. of Photonics Engg, Technical University of Denmark* (2012).

[Pev+09] R Peveling, T Pfau, O Aamczyk, R Eickhoff, and R Noe, « Multiplier-free Real-time Phase Tracking for Coherent QPSK Receivers [J] », *in*: *IEEE Photon Technol Lett* 21.*3* (Feb. 2009), pp. 137–139.

[Pfa16] Timo Pfau, « Real-Time Implementation of High-Speed Digital Coherent Transceivers », *in*: *Enabling Technologies for High Spectral-Efficiency Coherent Optical Communication Networks*, John Wiley Sons, Ltd, 2016, chap. 12, pp. 435–446, ISBN: 9781119078289, DOI: https://doi.org/10.1002/9781119078289.ch12, eprint: https://onlinelibrary.wiley.com/doi/pdf/10.1002/9781119078289.ch12, URL: https://onlinelibrary.wiley.com/doi/abs/10.1002/9781119078289.ch12.

[Pfa+09] Timo Pfau, Sebastian Hoffmann, and Reinhold Noé, « Hardware-efficient coherent digital receiver concept with feedforward carrier recovery for M-QAM constellations », *in*: *Journal of Lightwave Technology* 27.*8* (Apr. 2009), pp. 989–999.

[Por+22] Stefano Porto, Mohammad Chitgarha, Irene Leung, Robert Maher, Ryan Going, Stefan Wolf, Pavel Studenkov, Jiaming Zhang, Hossein Hodaei, Thomas Frost, et al., « Demonstration of a 2× 800 Gb/s/wave Coherent Optical Engine Based on an InP Monolithic PIC », *in*: *Journal of Lightwave Technology* 40.*3* (2022), pp. 664–671.

[Qur85] Shahid UH Qureshi, « Adaptive equalization », *in*: *Proceedings of the IEEE* 73.*9* (Sept. 1985), pp. 1349–1387.

[Rav+22] Tomer Raviv, Sangwoo Park, Osvaldo Simeone, Yonina C Eldar, and Nir Shlezinger, « Online Meta-Learning For Hybrid Model-Based Deep Receivers », *in*: *arXiv preprint arXiv:2203.14359* (2022).

[Ray+16] G Raybon, A Adamiecki, and J Cho, « High Symbol Rate, Single Carrier, Coherent Optical Transmission Systems for Data Rates from 400 Gb/s to 1.0-Tb/s », *in*: *Photonic Networks and Devices*, Optica Publishing Group, 2016, NeM4B–2.

[Rea+90] Michael J Ready and Richard P Gooch, « Blind equalization based on radius directed adaptation », *in*: *International Conference on Acoustics, Speech, and Signal Processing*, IEEE, Albuquerque, NM, USA, 1990, pp. 1699–1702.

[Ric+13] David J Richardson, John M Fini, and Lynn E Nelson, « Space-division multiplexing in optical fibres », *in*: *Nature photonics* 7.*5* (Apr. 2013), pp. 354–362.

[Rud16] Sebastian Ruder, « An overview of gradient descent optimization algorithms », *in*: *arXiv preprint arXiv:1609.04747* (June 2016).

[Sai+81] S Saito and Y Yamamoto, « Direct observation of Lorentzian lineshape of semiconductor laser and linewidth reduction with external grating feedback », *in*: *Electronics Letters* 17.*9* (Apr. 1981), pp. 325–327.

[Sat+10] Naresh Satyan, Jacob B Sendowski, Arseny Vasilyev, George A Rakuljic, and Amnon Yariv, « Phase noise reduction of a semiconductor laser in a composite optical phase-locked loop », *in*: *Optical Engineering* 49.*12* (Dec. 2010), p. 124301.

[Sav08] Seb J Savory, « Digital filters for coherent optical receivers », *in*: *Optics express* 16.*2* (Jan. 2008), pp. 804–817.

[Sav10] Seb J Savory, « Digital coherent optical receivers: Algorithms and subsystems », *in*: *IEEE Journal of selected topics in quantum electronics* 16.*5* (May 2010), pp. 1164–1179.

[Sav+07] Seb J Savory, G Gavioli, RI Killey, and P Bayvel, « Transmission of 42.8 Gbit/s Polarizatio n Multiplexed NRZ-QPSK over 6400km of Standard Fiber with no Optical Dispersion Compensation », *in*: *Optical Fiber Communication Conference*, Optica Publishing Group, Anaheim, California, United States, 2007, OTuA1.

[Sch+11] Rene Schmogrow, Bernd Nebendahl, Marcus Winter, Arne Josten, David Hillerkuss, Swen Koenig, Joachim Meyer, Michael Dreschmann, Michael Huebner, Christian Koos, et al., « Error vector magnitude as a performance measure for advanced modulation formats », *in*: *IEEE Photonics Technology Letters* 24.*1* (2011), pp. 61–63.

[Sei08] Matthias Seimetz, « Laser linewidth limitations for optical systems with high-order modulation employing feed forward digital carrier phase estimation », *in*: *optical fiber communication conference*, Optical Society of America, San Diego, California United States, 2008, OTuM2.

[Sel+09] Mehrez Selmi, Yves Jaouen, and Philippe Ciblat, « Accurate digital frequency offset estimator for coherent PolMux QAM transmission systems », *in*: *2009 35th European Conference on Optical Communication*, IEEE, Vienna, Austria, 2009, pp. 1–2.

[Sen+09] John M Senior and M Yousif Jamro, *Optical fiber communications: principles and practice*, Pearson Education, 2009.

[Sha+22] Abtin Shahkarami, Mansoor Yousefi, and Yves Jaouen, « Complexity reduction over Bi-RNN-based nonlinearity mitigation in dual-pol fiber-optic com-

munications via a CRNN-based approach », *in*: *Optical Fiber Technology* 74 (2022), p. 103072.

[Shi+08a] William Shieh, Hongchun Bao, and Yan Tang, « Coherent optical OFDM: theory and design », *in*: *Optics express* 16.*2* (Jan. 2008), pp. 841–859.

[Shi+08b] William Shieh, Xingwen Yi, Yiran Ma, and Qi Yang, « Coherent optical OFDM: has its time come? », *in*: *Journal of Optical Networking* 7.*3* (Feb. 2008), pp. 234–255.

[Shi+20] James Shipman, Jerry D Wilson, Charles A Higgins, and Bo Lou, *An introduction to physical science*, Cengage Learning, 2020.

[Shy+92] John J Shynk et al., « Frequency-domain and multirate adaptive filtering », *in*: *IEEE Signal processing magazine* 9.*1* (Jan. 1992), pp. 14–37.

[Sid+18] Oleg Sidelnikov, Alexey Redyuk, and Stylianos Sygletos, « Equalization performance and complexity analysis of dynamic deep neural networks in long haul transmission systems », *in*: *Optics express* 26.*25* (Nov. 2018), pp. 32765–32776.

[Sil17] Edson Porto da Silva, « Linear and Nonlinear Impairment Compensation in Coherent Optical Transmission with Digital Signal Processing », PhD thesis, DTU Fotonik, Department of Photonics Engineering, Technical University of Denmark, Feb. 2017.

[Sil+16] Edson Porto da Silva and Darko Zibar, « Widely linear equalization for IQ imbalance and skew compensation in optical coherent receivers », *in*: *Journal of Lightwave Technology* 34.*15* (June 2016), pp. 3577–3586.

[Sim21] Jacqueline Sime, « Baseband mitigation of nonlinear impairments in SOA based coherent optical OFDM systems: stochastic and experimental analyses », PhD thesis, ENIB, Lab-STICC, CNRS UMR 6285, 2021.

[Skv+20] Pavel Skvortcov, Ian Phillips, and Wladek Forysiak, « Transmitter frequency-dependent IQ imbalance characterization and pre-emphasis », *in*: *Signal Processing in Photonic Communications*, Optical Society of America, Washington, DC United States, 2020, SpTh1I–2.

[Spa+11] Arnaldo Spalvieri and Luca Barletta, « Pilot-aided carrier recovery in the presence of phase noise », *in*: *IEEE Transactions on Communications* 59.*7* (May 2011), pp. 1966–1974.

[Sto+13] Josef Stoer and Roland Bulirsch, *Introduction to numerical analysis*, Springer Science & Business Media, 2013.

[Sto+04] Petre Stoica and Yngve Selen, « Model-order selection: a review of information criterion rules », *in*: *IEEE Signal Processing Magazine* 21.*4* (July 2004), pp. 36–47.

[Tan+07] Deepaknath Tandur and Marc Moonen, « Joint adaptive compensation of transmitter and receiver IQ imbalance under carrier frequency offset in OFDM-based systems », *in*: *IEEE Transactions on Signal Processing* 55.*11* (Oct. 2007), pp. 5246–5252.

[Tar+05] Alireza Tarighat, Rahim Bagheri, and Ali H Sayed, « Compensation schemes and performance analysis of IQ imbalances in OFDM receivers », *in*: *IEEE Transactions on Signal Processing* 53.*8* (July 2005), pp. 3257–3268.

[Tay09] Michael G Taylor, « Phase estimation methods for optical coherent detection using digital signal processing », *in*: *Journal of Lightwave Technology* 27.*7* (Apr. 2009), pp. 901–914.

[Tri+12] Abdessalem Trimeche, Nesrine Boukid, Anis Sakly, and Abdellatif Mtibaa, « Performance analysis of ZF and MMSE equalizers for MIMO systems », *in*: *7th International Conference on Design & Technology of Integrated Systems in Nanoscale Era*, IEEE, Tunis, Tunisia, 2012, pp. 1–6.

[Tub+05] Jan Tubbax, Boris Come, Liesbet Van der Perre, Stéphane Donnay, Marc Engels, Hugo De Man, and Marc Moonen, « Compensation of IQ imbalance and phase noise in OFDM systems », *in*: *IEEE Transactions on Wireless Communications* 4.*3* (May 2005), pp. 872–877.

[Uda+13] R Udayakumar, V Khanaa, and T Saravanan, « Chromatic dispersion compensation in optical fiber communication system and its simulation », *in*: *Indian Journal of Science and Technology* 6.*6* (May 2013), pp. 4762–4766.

[Vib+91] Mats Viberg, Bjorn Ottersten, and Thomas Kailath, « Detection and estimation in sensor arrays using weighted subspace fitting », *in*: *IEEE Transactions on Signal Processing* 39.*11* (Nov. 1991), pp. 2436–2449.

[Vir+20] Pauli Virtanen et al., « SciPy 1.0: Fundamental Algorithms for Scientific Computing in Python », *in*: *Nature Methods* 17 (Feb. 2020), pp. 261–272, DOI: 10.1038/s41592-019-0686-2.

[Vit+83] Andrew J Viterbi and Audrey M Viterbi, « Nonlinear estimation of PSK-modulated carrier phase with application to burst digital transmission », *in*: *IEEE Transactions on Information theory* 29.*4* (July 1983), pp. 543–551.

[Wan+01] Yan Wang, Erchin Serpedin, Philippe Ciblat, and Philippe Loubaton, « Non-data aided feedforward cyclostationary statistics based carrier frequency offset estimators for linear modulations », *in*: *GLOBECOM'01. IEEE Global Telecommunications Conference (Cat. No. 01CH37270)*, vol. 2, IEEE, San Antonio, TX, USA, 2001, pp. 1386–1390.

[Wid+77] Bernard Widrow, John McCool, Michael G Larimore, and C Richard Johnson, « Stationary and nonstationary learning characteristics of the LMS adaptive filter », *in*: *Aspects of signal processing*, Springer, 1977, pp. 355–393.

[Win+18] Peter J Winzer, David T Neilson, and Andrew R Chraplyvy, « Fiber-optic transmission and networking: the previous 20 and the next 20 years », *in*: *Optics express* 26.*18* (Aug. 2018), pp. 24190–24239.

[Xie+12] Chongjin Xie and Gregory Raybon, « Digital PLL based frequency offset compensation and carrier phase estimation for 16-QAM coherent optical communication systems », *in*: *European conference and exhibition on optical communication*, Optica Publishing Group, Amsterdam, Netherlands, 2012, Mo–1.

[Xu+11] T. Xu, G. Jacobsen, S. Popov, M. Forzati, J. Mårtensson, M. Mussolin, J. Li, K. Wang, Y. Zhang, and A. T. Friberg, « Frequency-Domain Chromatic Dispersion Equalization Using Overlap-Add Methods in Coherent Optical System », *in*: 32.*2* (2011), pp. 131–135, DOI: doi:10.1515/joc.2011.022, URL: https://doi.org/10.1515/joc.2011.022.

[Xu+10] Tianhua Xu, Gunnar Jacobsen, Sergei Popov, Jie Li, Evgeny Vanin, Ke Wang, Ari T Friberg, and Yimo Zhang, « Chromatic dispersion compensation in coherent transmission system using digital filters », *in*: *Optics express* 18.*15* (July 2010), pp. 16243–16257.

[Zha+12] Fangzheng Zhang, Yan Li, Jian Wu, Wei Li, Xiaobin Hong, and Jintong Lin, « Improved Pilot-Aided Optical Carrier Phase Recovery for Coherent *M*-QAM », *in*: *IEEE Photonics Technology Letters* 24.*18* (July 2012), pp. 1577–1580.

[Zha+19a] Qun Zhang, Yanfu Yang, Changjian Guo, Xian Zhou, Yong Yao, Alan Pak Tao Lau, and Chao Lu, « Algorithms for blind separation and estimation of transmitter and receiver IQ imbalances », *in*: *Journal of Lightwave Technology* 37.*10* (Feb. 2019), pp. 2201–2208.

[Zha+15] Donghe Zhao, Lixia Xi, Xianfeng Tang, Wenbo Zhang, Yaojun Qiao, and Xiaoguang Zhang, « Digital pilot aided carrier frequency offset estimation for coherent optical transmission systems », *in*: *Optics express* 23.*19* (Sept. 2015), pp. 24822–24832.

[Zha+19b] Jian Zhao, Yaping Liu, and Tianhua Xu, « Advanced DSP for coherent optical fiber communication », *in*: *Applied Sciences* 9.*19* (Oct. 2019), p. 4192.

[Zho+11] Xian Zhou, Xue Chen, and Keping Long, « Wide-range frequency offset estimation algorithm for optical coherent systems using training sequence », *in*: *IEEE Photonics Technology Letters* 24.*1* (Oct. 2011), pp. 82–84.

[Zhu+02] Xu Zhu and Ross D Murch, « Performance analysis of maximum likelihood detection in a MIMO antenna system », *in*: *IEEE Transactions on Communications* 50.*2* (Feb. 2002), pp. 187–191.

[Zib+15] Darko Zibar, Molly Piels, Rasmus Jones, and Christian G Schäeffer, « Machine learning techniques in optical communication », *in*: *Journal of Lightwave Technology* 34.*6* (Dec. 2015), pp. 1442–1452.

DOCTORAT BRETAGNE LOIRE / MATHSTIC

ÉCOLE NATIONALE D'INGÉNIEURS DE BREST

Titre : Compensation globale des imperfections linéaires du système pour les communications optiques cohérentes à haut débit

Mot clés : communications optiques cohérentes, imperfections linéaires, compensation globale, traitement statistique du signal, réseau paramétrique à base de modèles

Résumé : Les communications optiques cohérentes représentent une technique clé qui pourrait répondre à l'augmentation de la demande de débit de données. Cependant, avec l'augmentation de la capacité du canal, l'impact des imperfections devient plus sévère et doit être compensé. Cette thèse se concentre sur la compensation des imperfections linéaires en ayant comme perspective d'avenir les imperfections non linéaires. L'approche conventionnelle de compensation met en cascade plusieurs blocs de traitement de signal numérique, chacun compensant une imperfection particulière. Cette méthode est problématique dans les scénarios complexes, et ses performances peuvent être drastiquement limitées. Deux approches visant à estimer et à compenser globalement les diverses déficiences linéaires ont été proposées pour surmonter ces limitations. Premièrement, une approche de traitement statistique du signal qui estime et compense globalement les imperfections linéaires est présentée. Ensuite, un réseau paramétrique à base de modèles est conçu pour réaliser une compensation globale d'une manière facilement adaptable. Les approches sont validées par des simulations numériques et des démonstrations expérimentales dans des scénarios simplifiés.

Title: Global compensation of system linear impairments for high-speed coherent optical communications

Keywords: coherent optical communications, linear imperfections, global compensation, statistical signal processing, model-based parametric network

Abstract: Coherent optical communications represent a key technology that could answer the increase of high data rate demands. However, with the increase in the channel capacity, the impact of imperfections becomes more severe and should be mitigated. This thesis focuses on the compensation of linear imperfections having as a future perspective the nonlinear ones. The conventional compensation approach cascades multiple digital signal processing blocks, each compensating for a particular impairment. This method is problematic in complex scenarios, and its performance may be drastically limited. Two techniques that aim to estimate and compensate for various linear impairments globally were proposed to overcome this limitation. First, a statistical signal processing approach that globally estimates and compensates for linear imperfections is introduced. Secondly, a model-based parametric network is designed to achieve global compensation in an easily adaptable manner. The approaches are validated through numerical simulations and experimental demonstrations in simplified scenarios.